Nonlinear response of glass–forming dispersions under applied time–dependent deformations

Dissertation submitted for the degree of Doctor of Natural Sciences

Presented by
Fabian Frahsa

at the
Universität Konstanz

Mathematisch–Naturwissenschaftliche Sektion

Fachbereich Physik

Date of the oral examination: 24.03.2015
First referee: Prof. Dr. Matthias Fuchs
Second referee: Prof. Dr. Thomas Voigtmann

Acknowledgments

There were many people contributing to this thesis in discussions and cooperations.

First of all, I would like to thank Prof. Matthias Fuchs, who offered me the opportunity to work on this project. Despite his many obligations, he constantly made efforts to aid in any possible form. He always took his time for supervising me concerning the minor problems just as much as the great ones. By introducing me to many new topics, he helped me to learn a lot in the recent years. At the same time, he offered me much freedom, to explore the topic of my thesis.

Of course, I also thank Prof. Thomas Voigtmann, who agreed to be the second referee for this thesis. In many informative discussions on different occasions, he offered me new perspectives on a large variety of topics.

I owe Marianne Grießer many thanks for guiding me through the bureaucratic jungle, that will remain a mystery to me.

I thank Prof. Eva Weig and Dr. Peter Keim who agreed to be examiners in my oral exam.

I also want to thank my family for their support during my studies and as a PhD student. There a many colleagues, whom I want to thank, all colleagues involved in the journal article on the Bauschinger effect, Miriam Siebenbürger for many fruitful and interesting discussions, Fabian Weyßer and Christof Walz, for preparing me on what I should expect while working on a PhD project, all the colleagues who I have met in Konstanz for the friendly collaboration and the moral support. And I would thank especially Niv Keren, Sebastian Fritschi and Simon Papenkort for proof reading this thesis.

Contents

1. Introduction

In the year 2011, the Gesellschaft für deutsche Sprache has elected "Stresstest" as the word of the year. In its statement [1], the Gesellschaft für deutsche Sprache made the indistinct claim that the expression originated in human medicine and has been adapted for banks, train stations, governments and nuclear power plants. What was lost in translation about the etymology, is that the German "Stresstest" is a loanword of the English "stress test", which is used metaphorically in human medicine and all other listed examples. Stress tests are conveyed literally in engineering and material testing. It is used to study, if the testes material can sustain an applied constant stress for a long time, and if not, when will it break or yield. This question is one of the major topics of this thesis.

It studies the nonlinear response of glass–forming dispersions under applied time–dependent deformations. Applying a load can provide a further comprehension of the process of yielding. The comparison of both, stress–controlled and strain–controlled rheology, is a method to find the underlying universal concepts that describe the dynamics of a glass–forming liquid. Therefore, an improved comprehension is gained of what makes a glass.

Glass–forming dispersions are modeled as an infinitely large system of monodisperse hard spheres suspended in a solvent. This model is a good approximation for all glass formers, highly repulsive on short ranges (below the particle diameter) and do not show long–range interaction. The solvent is treated as continuum, neglecting hydrodynamic interactions. Applying stress would affect a deformation response which the solvent mediates in such a way, that the deformation field might be time dependent but remains homogeneous in space. The deformation is considered to be an incompressible flow, the particle number density remains homogenous. The suspended spheres undergo Brownian motion [2], just as the dispersed pollen in Browns observations did. One example for a physical system which can be described by such a model are colloidal suspensions. These suspension consist of a homogeneous solvent and dispersed particles, the colloids. In order to qualify as colloids, the sedimentation of the particles has to be negligible, at least during observation time. One advantage of colloidal suspensions is their large size, compared to molecular and atomic particles. This makes it possible to observe colloids in optical microscopy and due to the slow velocities of their Brownian motion, it is feasible to track single particle trajectories.

The following chapter, chap. 2, introduces the theoretical framework, used in this thesis. Starting from the microscopic picture of Brownian motion, the MCT–ITT formalism describes ensemble averaged nonequilibrium quantities using generalized Green–Kubo relations. Shear

stress is given as an integral through the transient density–fluctuation correlation functions. Without shear flow, the theory predicts a transition from viscous fluids to ideal glasses. Close to the transition point, a schematic model can be used.

This model is used to describe the history–dependent material properties after a reversal of shear flow in chap. 3. The effects are discussed in their relation to the Bauschinger–effect and yielding is read as a transition from dominantly reversible anelastic response to the onset of an irreversible plastic flow.

In chap. 4, stress and strain change their roles. The strain response of applied stress is studied in form of creep under constant stress and the strain response resulting from stress ramps.

Chap. 5 gives an English and a German conclusion. A discussion on the numerical details, A, the used mathematical techniques, B, and the parameters of the schematic Mode–coupling model, C, have been added in the appendices.

2. Theoretical framework

This chapter introduces the underlying theoretical concepts of this thesis. It starts with a short introduction on Brownian motion and the projector operator formalism developed by Zwanzig [3] and Mori [4]. The nonlinear response of glass–forming dispersions under applied time–dependent deformations is computed using the Mode Coupling Theory (MCT), which is introduced in the third section of this chapter. A simplified schematic model of the Mode Coupling Theory is described subsequently to the theory which forms its base. An application of this schematic model to strain–controlled rheology is discussed in chap. 3 and is important for a detailed understanding for the chosen approach to compute the deformation response under applied stress, discussed in chap. 4.

2.1. Brownian motion

In his botanical studies [2], Brown observed under a microscope the random motion of pollen dispersed in water and concluded that this motion of the pollen is not caused by flows of the water or evaporation. Einstein studied the phenomenon of Brownian motion theoretically [5]. He connected it to disordered thermal motion and derived a result for its diffusion. Further work on this topic has been carried out by Smoluchowski [6], describing the particles motion as a result of several collisions.

This motivated Langevin to describe the Brownian motion by formulating stochastic forces of the thermal collisions. The underlying equation for this description is the Langevin–equation [7],

$$m\ddot{\boldsymbol{x}} = -6\pi\eta R\dot{\boldsymbol{x}} + \boldsymbol{f}. \tag{2.1}$$

It describes the force acting on a Brownian particle as the sum of a damping force and a stochastic force, $\boldsymbol{f}$, described in the subsequent section in more detail. Overdamping the Langevin–equation, $m\ddot{\boldsymbol{x}} = 0$, leads to the following Fokker–Planck equation [8, 9],

$$\frac{\mathrm{d}}{\mathrm{d}t}\psi = \left(-\frac{\partial}{\partial x}\Delta^{(1)} + \frac{\partial^2}{\partial x^2}\Delta^{(2)}\right)\psi. \tag{2.2}$$

The microscopic starting point of the model underlying this thesis is the Smoluchowski equation for Brownian motion of an ensemble of particles. The state that describes the positions, $\boldsymbol{r}_i$, of each particle, i, can be abbreviated by a single variable, Γ [10]. The Smoluchowski

equation reads,

$$\partial_t \psi(\Gamma, t) = \sum_i \boldsymbol{\nabla}_i \cdot \left(D_0 \boldsymbol{\nabla}_i - \frac{D_0}{k_B T} \boldsymbol{F}_i \right) \psi(\Gamma, t), \tag{2.3}$$

which describes the time evolution of the distribution function, $\psi(\Gamma, t)$, with the Smoluchowski operator,

$$\Omega_{\text{eq}} = \sum_i \boldsymbol{\nabla}_i \cdot \left(D_0 \boldsymbol{\nabla}_i - \frac{D_0}{k_B T} \boldsymbol{F}_i \right). \tag{2.4}$$

In this thesis, I will follow the convention of using reduced units, by setting the constants that appear in the Smoluchowski equation to one,

$$D_0 = 1, \tag{2.5}$$

$$k_B T = 1 \tag{2.6}$$

$$d = 1. \tag{2.7}$$

Length scales are expressed in units of the particle's diameter, d. The energy is expressed in scales of the thermal energy, $k_B T$, and the Stokes–Einstein–Sutherland coefficient, D_0, together with the particle diameter define the reduced time scale, $\frac{d^2}{D_0}$. If length scales are given in units of the particle's radius, R, instead of the diameter, an the time scale is accordingly changed, I will specify this explicitly.

The Smoluchowski operator reads in the reduced units,

$$\Omega_{\text{eq}} = \sum_i \boldsymbol{\nabla}_i \cdot (\boldsymbol{\nabla}_i - \boldsymbol{F}_i). \tag{2.8}$$

2.2. Slow variables

The dynamics of the system corresponds to a motion in phase space, a Hilbert space. From the full set of functions of phase space variables, $f(\{x_i, p_i\})$, one can choose a set of slowly varying phase space functions $A(\{x_i, p_i\})$ and describe trajectories in phase space, i.e., the dynamics of the system, as functions, $\mathcal{F}(A)$, of these slowly varying functions [3, 4, 11]. This set of dynamical variables, A, belong to a subspace of the full Hilbert space. The variables should be chosen in such a way, that they represent the relevant variables, which are of interest.

To project into the subspace of the variables, A, Zwanzig defines an operator [11],

$$\mathcal{P} = |A\rangle \langle A, A\rangle^{-1} \langle A|, \tag{2.9}$$

which fulfills the following requirements,

- it is idempotent, $\mathcal{P}^2 = \mathcal{P}$,
- on the subspace of slow variables, $\langle A|$, it acts as the identity operator, $\mathcal{P}A = \langle A|$,
- the sum of the subspace of slow variables and the complementary space make up the full space, so that any variable ,B, can be decomposed into, $\mathcal{P}B = \langle B, A\rangle \langle A, A\rangle^{-1} \langle A|$, and, $(1-\mathcal{P})\, B = \langle B| - \langle B, A\rangle \langle A, A\rangle^{-1} \langle A|$.

The operator, $\mathcal{L}$, which could be the Smoluchowski operator from eq. (2.3), can be split into two parts,

$$\mathcal{L} = \mathcal{P}\mathcal{L} + (1-\mathcal{P})\mathcal{L}. \tag{2.10}$$

The following operator identity,

$$e^{t\mathcal{L}} = e^{t(1-\mathcal{P})\mathcal{L}} + \int_0^t \mathrm{d}s\; e^{(t-s)\mathcal{L}}\mathcal{P}\mathcal{L}e^{s(1-\mathcal{P})\mathcal{L}}, \tag{2.11}$$

can be either proven by differentiation or by using the Laplace transforms. When the operator on the left–hand side of the equations acts on $(1-\mathcal{P})\mathcal{L}A$, this yields,

$$\begin{aligned} e^{t\mathcal{L}}(1-\mathcal{P})\mathcal{L}A =& e^{t\mathcal{L}}\mathcal{L}A - e^{t\mathcal{L}}\mathcal{P}\mathcal{L}A && (2.12)\\ =& \frac{\partial}{\partial t}e^{t\mathcal{L}}A - \langle \mathcal{L}A, A\rangle \langle A, A\rangle^{-1} e^{t\mathcal{L}}A && (2.13)\\ =& \frac{\partial}{\partial t}A(t) - \langle \mathcal{L}A, A\rangle \langle A, A\rangle^{-1} A(t). && (2.14) \end{aligned}$$

Analogously, the operator from the right–hand side gives,

$$\begin{aligned} & e^{t(1-\mathcal{P})\mathcal{L}}(1-\mathcal{P})\mathcal{L}A + \int_0^t \mathrm{d}s\; e^{(t-s)\mathcal{L}}\mathcal{P}\mathcal{L}e^{s(1-\mathcal{P})\mathcal{L}}(1-\mathcal{P})\mathcal{L}A && (2.15)\\ =& e^{t(1-\mathcal{P})\mathcal{L}}(1-\mathcal{P})\mathcal{L}A + \int_0^t \mathrm{d}s\; \left\langle \mathcal{L}e^{s(1-\mathcal{P})\mathcal{L}}(1-\mathcal{P})\mathcal{L}A, A\right\rangle \langle A, A\rangle^{-1} e^{(t-s)\mathcal{L}}A. && (2.16) \end{aligned}$$

Using the abbreviations, $f(t) = e^{t(1-\mathcal{P})\mathcal{L}}(1-\mathcal{P})\mathcal{L}A$, $i\Omega = \langle \mathcal{L}A, A\rangle \langle A, A\rangle^{-1}$ and $K(t) = \langle \mathcal{L}f(t), A\rangle \langle A, A\rangle^{-1}$, the Zwanzig–Mori equation is obtained,

$$\frac{\partial}{\partial t}A(t) = i\Omega A(t) - \int_0^t \mathrm{d}s\; K(t-s)A(s) + f(t). \tag{2.17}$$

Time–correlation functions, $C(t) = \langle A(t)A(0)\rangle$, can be obtained by taking the inner product with the variable at a previous time, $A(0)$. If one does this for each term in eq. (2.17), the inner product with the noise term, $f(t)$, vanishes, as the noise term is perpendicular to

the variables, A. The resulting equation for the time–correlation function is,

$$\frac{\partial}{\partial t}C(t) = i\Omega C(t) - \int_0^t \mathrm{d}s\; K(t-s)C(s). \tag{2.18}$$

2.3. Mode coupling theory

Mode–Coupling Theory (MCT) is a microscopic theory which describes the dynamics of viscous and glass–forming liquids. Initially it was developed by Götze, Bengtzelius and Sjölander [12]. Its major prediction is the glass transition from a liquid to a non–ergodic glass at a critical temperature T_c or critical density n_c, often given in terms of the critical packing fraction $\varphi_c = \frac{4}{3}\pi R^3 n_c$.

MCT uses the Zwanzig–Mori projection–operator formalism and factorization approximations, to describe dense matter with density–fluctuation modes as slow variables. At the glass transition, it predicts a critical slowing down of the structural dynamics which separates glassy and fluid dynamics. In this section, I will recapitulate the underlying theory of this thesis, the Integration through transients–Mode Coupling Theory developed by Fuchs and Cates [13, 10]. The integration–through transients (ITT) formalism uses the concepts of quiescent Mode–coupling theory and extends it, that as a consequence it can also describe non–linear response. By imposing incompressible flow, the ITT formalism describes explicitly a non–equilibrium scenario. Nonequilibrium averages are given by generalized Green–Kubo relations.

A detailed discussion of the microscopic theory goes beyond the scope of this thesis. In the following, I will summarize the theory in the form of ref. [14] by Brader et. al.

2.3.1. Smoluchowski equation under shear flow

If one considers shear flow, the Smoluchowski operator from eq. (2.3) is extended in the following way [14]

$$\Omega(t) = \Omega_{\mathrm{eq}} + \delta\Omega(t) = \sum_i \boldsymbol{\nabla}_i \cdot \left(\boldsymbol{\nabla}_i - \boldsymbol{F}_i - \boldsymbol{\kappa}(t)\cdot\boldsymbol{r}_i\right), \tag{2.19}$$

with the velocity gradient or strain rate tensor, $\kappa_{ij} = \partial v_j/\partial x_i$. This thesis will focus on simple shear flow,

$$\boldsymbol{\kappa}(t) = \begin{pmatrix} 0 & \dot\gamma(t) & 0 \\ 0 & 0 & 0 \\ 0 & 0 & 0 \end{pmatrix}, \tag{2.20}$$

with the only nonvanishing element, $\kappa_{xy}(t) = \dot\gamma(t)$, and the shear rate, $\dot\gamma(t)$.

The Smoluchowski operator is given again in reduced units. In reduced units, the velocity gradient tensor is quantified in terms of the dimensionless bare Péclet number, $Pe_0 = \frac{\dot{\gamma} d^2}{D_0}$.

The solution of the Smoluchowski equation, $\partial_t \psi(t) = \Omega(t)\psi(t)$, is written with a time–ordered exponential as time–evolution operator,

$$\psi(t) = e_+^{\int_{t'}^{t} \mathrm{d}s \Omega(s)} \psi_{\mathrm{eq}}. \tag{2.21}$$

The Smoluchowski operator can be split into two parts, the equilibrium operator of eq. (2.4) and a nonequilibrium part. The analogous splitting for the distribution function into the equilibrium distribution function, the solution of eq. (2.3), and a nonequilibrium part of the distribution function yields,

$$\Omega(t) = \Omega_{\mathrm{eq}} + \delta\Omega(t), \tag{2.22}$$
$$\psi(t) = \psi_{\mathrm{eq}} + \delta\psi(t). \tag{2.23}$$

If one considers that the time derivation of an equilibrium distribution function vanishes,

$$\Omega_{\mathrm{eq}} \psi_{\mathrm{eq}} = 0, \tag{2.24}$$

and that this thesis only studies incompressible fluids,

$$\mathrm{Tr}\boldsymbol{\kappa} = 0, \tag{2.25}$$

and defining the tensor,

$$\hat{\sigma}_{\alpha,\beta} = \delta_{\alpha,\beta} - \sum_i r_i^\alpha F_i^\beta, \tag{2.26}$$

one finds in accordance with ref. [14],

$$\Omega(t)\psi_{\mathrm{eq}} = [\boldsymbol{\kappa} : \hat{\boldsymbol{\sigma}}]\, \psi_{\mathrm{eq}}. \tag{2.27}$$

In the last equation, the following abbreviation for tracing over two tensors, $\mathbf{X}$, and $\mathbf{Y}$, has been used,

$$[\mathbf{X} : \mathbf{Y}] = \sum_{\alpha,\beta} X_{\alpha,\beta} Y_{\beta,\alpha}. \tag{2.28}$$

Now the Smoluchowski equation can be written as,

$$\partial_t \left(\psi_{\mathrm{eq}} + \delta\psi(t)\right) = \left(\Omega_{\mathrm{eq}} + \delta\Omega(t)\right)\left(\psi_{\mathrm{eq}} + \delta\psi(t)\right) \tag{2.29}$$

$$\Leftrightarrow \partial_t \delta\psi(t) = \Omega(t)\delta\psi(t) + \left[\boldsymbol{\kappa} : \hat{\boldsymbol{\sigma}}\right]\psi_{\mathrm{eq}} \tag{2.30}$$

$$= \int_0^t \mathrm{d}t' e_+^{\int_{t'}^t \mathrm{d}s\Omega(s)} \left[\boldsymbol{\kappa} : \hat{\boldsymbol{\sigma}}\right]\psi_{\mathrm{eq}}. \tag{2.31}$$

Solving the Smoluchowski equation yields the full time–dependent distribution function and determines the nonequilibrium contributions,

$$\psi(t) = \psi_{\mathrm{eq}} + \delta\psi(t) \tag{2.32}$$

$$= \psi_{\mathrm{eq}} + \int_0^t \mathrm{d}t' e_+^{\int_{t'}^t \mathrm{d}s\Omega(s)} \left[\boldsymbol{\kappa} : \hat{\boldsymbol{\sigma}}\right]\psi_{\mathrm{eq}}. \tag{2.33}$$

The expression for the distribution function allows to express a nonequilibrium average for an arbitrary variable, f,

$$\langle f \rangle^{\mathrm{neq}} = \langle f \rangle + \int \mathrm{d}\Gamma \int_0^t \mathrm{d}t' f e_+^{\int_{t'}^t \mathrm{d}s\Omega(s)} \left[\boldsymbol{\kappa} : \hat{\boldsymbol{\sigma}}\right]\psi_{\mathrm{eq}} \tag{2.34}$$

$$= \langle f \rangle + \int \mathrm{d}\Gamma \int_0^t \mathrm{d}t' \left[\boldsymbol{\kappa} : \hat{\boldsymbol{\sigma}}\right]\psi_{\mathrm{eq}} e_-^{\int_{t'}^t \mathrm{d}s\Omega^\dagger(s)} f \tag{2.35}$$

$$= \langle f \rangle + \int_0^t \mathrm{d}t' \left\langle \left[\boldsymbol{\kappa} : \hat{\boldsymbol{\sigma}}\right] e_-^{\int_{t'}^t \mathrm{d}s\Omega^\dagger(s)} f \right\rangle. \tag{2.36}$$

2.3.2. Wave–vector advection

Assuming an undercooled equilibrated liquid as described in the previous section, one can introduce a translation of the spacial coordinates,

$$\boldsymbol{x'} \to \boldsymbol{x} + \boldsymbol{a}t, \tag{2.37}$$

with some arbitrary vector, $\boldsymbol{a}$. For homogeneous flows, expressed by a velocity gradient tensor which does not depend on spacial coordinates, the Smoluchowski equation does only depend on the relative coordinates of the particles. Therefore it remains invariant, if the coordinated of each particle is translated by a vector, $\boldsymbol{a}$.

A proof, that the distribution function, $\psi(t)$, that solves the Smoluchowski equation for a homogeneous flow is also translationally invariant, is given in ref. [14].

In the same ref., a proof is given that a two–time correlation function of wave–vector–

dependent fluctuations,

$$C_{f_{\boldsymbol{q}} g_{\boldsymbol{k}}}(t,t') = \int \mathrm{d}\Gamma \psi(t') f^*_{\boldsymbol{q}} e_-^{\int_{t'}^{t} \mathrm{d}s \Omega^\dagger(s)} g_{\boldsymbol{k}}, \tag{2.38}$$

which is the time–correlation function of the slow variables in Mode–Coupling Theory, remains invariant under spacial translations if the wave vector, $\boldsymbol{q}$, is the advected wave vector of the wave vector, $\boldsymbol{k}$, at an earlier time,

$$\boldsymbol{q} = \boldsymbol{k}(t,t') = \boldsymbol{k}\, e_+^{\int_{t'}^{t} \mathrm{d}s \boldsymbol{\kappa}(s)}. \tag{2.39}$$

For simple shear flow, as defined in eq. (2.20), the time–ordered exponential can be expressed exactly as an expansion,

$$e_+^{\int_{t'}^{t} \mathrm{d}s \boldsymbol{\kappa}(s)} = \mathbf{1} + \boldsymbol{\kappa}(t,t') + \mathcal{O}(\boldsymbol{\kappa}^2), \tag{2.40}$$

which conveniently can be truncated after the term of linear order, as the velocity gradient tensor for simple shear flow vanishes in higher orders, $\boldsymbol{\kappa} \cdot \boldsymbol{\kappa} = \mathbf{0}$.

2.3.3. Exact projections onto density modes

As in sec. 2.2, one can again define a projector onto the slow variables. In MCT, the slow variables are the density modes, $\rho_{\boldsymbol{q}} = \sum_i e^{i\boldsymbol{q}\boldsymbol{r}_i}$. The operator and another projector onto the subspace perpendicular to it are defined,

$$\mathcal{P} = \sum_{\boldsymbol{k}} |\rho_{\boldsymbol{k}}\rangle \langle \rho^*_{\boldsymbol{k}}| \tag{2.41}$$

$$\mathcal{Q} = 1 - \mathcal{P}, \tag{2.42}$$

so that $\mathcal{P}\mathcal{Q} = 0$.
The number of particles is conserved, $\partial_t N = 0$, and the flow is considered to be incompressible, $\langle \boldsymbol{\kappa}(t) : \hat{\boldsymbol{\sigma}} \rangle = 0$. As a consequence, the integrand of eq. (2.36) vanishes, if the density mode at the wave vector zero is chosen as variable, $f = \rho_{\boldsymbol{q}=\mathbf{0}}$,

$$\left\langle [\boldsymbol{\kappa} : \hat{\boldsymbol{\sigma}}]\, e_-^{\int_{t'}^{t} \mathrm{d}s \Omega^\dagger(s)} \rho_{\boldsymbol{q}=\mathbf{0}} \right\rangle \tag{2.43}$$

$$= N \langle [\boldsymbol{\kappa} : \hat{\boldsymbol{\sigma}}] \rangle \tag{2.44}$$

$$= 0. \tag{2.45}$$

This expression has to vanish as well for any other $\rho_{\boldsymbol{q}}$-mode, due to translational invariance.

Because of this, one can rewrite eq. (2.36) in the following way

$$\langle f\rangle^{\mathrm{neq}} = \langle f\rangle + \int_0^t \mathrm{d}t' \left\langle [\boldsymbol{\kappa} : \hat{\boldsymbol{\sigma}}]\, \mathcal{Q} e_-^{\int_{t'}^t \mathrm{d}s \Omega^\dagger(s)} \mathcal{Q} f \right\rangle . \tag{2.46}$$

Using the operator identities

$$e_-^{\int_{t'}^t \mathrm{d}s \Omega^\dagger(s)} = e_-^{\int_{t'}^t \mathrm{d}s \mathcal{Q}\Omega^\dagger(s)} + \int_{t'}^t \mathrm{d}s' e_-^{\int_{t'}^{s'} \mathrm{d}s \Omega^\dagger(s)} \mathcal{P}\Omega^\dagger(s') e_-^{\int_{s'}^t \mathrm{d}s \mathcal{Q}\Omega^\dagger(s)}, \tag{2.47}$$

$$e_-^{\int_{t'}^t \mathrm{d}s \mathcal{Q}\Omega^\dagger(s)} \mathcal{Q} = e_-^{\int_{t'}^t \mathrm{d}s \mathcal{Q}\Omega^\dagger(s)\mathcal{Q}} \mathcal{Q}, \tag{2.48}$$

with the latter as a simple consequence of the idempotency of $\mathcal{Q}$, one can find the exact expression for eq. (2.36) in this form

$$\langle f\rangle^{\mathrm{neq}} = \langle f\rangle + \int_0^t \mathrm{d}t' \left\langle [\boldsymbol{\kappa} : \hat{\boldsymbol{\sigma}}]\, \mathcal{Q} e_-^{\int_{t'}^t \mathrm{d}s \mathcal{Q}\Omega^\dagger(s)\mathcal{Q}} \mathcal{Q} f \right\rangle . \tag{2.49}$$

2.3.4. Mode–coupling approximations

Higher moments for a Gaussian distribution can be expressed as a sum of second order moments. MCT introduces an ad-hoc approximation of the factorization of an average of a product into a product of averages, $\left\langle \rho^*_{\boldsymbol{k}} \rho^*_{\boldsymbol{p}} \rho_{\boldsymbol{k}} \rho_{\boldsymbol{p}} \right\rangle \approx \left\langle \rho^*_{\boldsymbol{k}} \rho_{\boldsymbol{k}} \right\rangle \left\langle \rho^*_{\boldsymbol{p}} \rho_{\boldsymbol{p}} \right\rangle$ to define a projector onto density pairs,

$$\mathcal{P}_2 = \sum_{\boldsymbol{k}>\boldsymbol{p}} \frac{|\rho_{\boldsymbol{k}}\rho_{\boldsymbol{p}}\rangle \left\langle \rho^*_{\boldsymbol{k}} \rho^*_{\boldsymbol{p}} \right|}{N^2 S_k S_p}. \tag{2.50}$$

If one uses this approximation for the result in eq. (2.49), an approximation for the stress response reads

$$\boldsymbol{\sigma}(t) = \frac{1}{V} \int_0^t \mathrm{d}t' \left\langle [\boldsymbol{\kappa} : \hat{\boldsymbol{\sigma}}]\, \mathcal{Q}\mathcal{P}_2 e_-^{\int_{t'}^t \mathrm{d}s \mathcal{Q}\Omega^\dagger(s)\mathcal{Q}} \mathcal{P}_2 \mathcal{Q} \hat{\boldsymbol{\sigma}} \right\rangle \tag{2.51}$$

$$= \sum_{\substack{\boldsymbol{k}>\boldsymbol{p} \\ \boldsymbol{k}'>\boldsymbol{p}'}} \frac{1}{V} \int_0^t \mathrm{d}t' \left\langle [\boldsymbol{\kappa} : \hat{\boldsymbol{\sigma}}]\, \mathcal{Q}\rho_{\boldsymbol{k}'}\rho_{\boldsymbol{p}'} \right\rangle \left\langle \rho^*_{\boldsymbol{k}} \rho^*_{\boldsymbol{p}} \mathcal{Q} \hat{\boldsymbol{\sigma}} \right\rangle \frac{\left\langle \rho^*_{\boldsymbol{k}'} \rho^*_{\boldsymbol{p}'} e_-^{\int_{t'}^t \mathrm{d}s \mathcal{Q}\Omega^\dagger(s)\mathcal{Q}} \rho_{\boldsymbol{k}}\rho_{\boldsymbol{p}} \right\rangle}{N^2 S_{k'} S_{p'} N^2 S_k S_p} \tag{2.52}$$

$$= \sum_{\substack{\boldsymbol{k}>\boldsymbol{p} \\ \boldsymbol{k}'>\boldsymbol{p}'}} \frac{1}{V} \int_0^t \mathrm{d}t' V^{(1)}_{\boldsymbol{k}',\boldsymbol{p}'} V^{(2)}_{\boldsymbol{k},\boldsymbol{p}} \frac{\left\langle \rho^*_{\boldsymbol{k}'} \rho^*_{\boldsymbol{p}'} e_-^{\int_{t'}^t \mathrm{d}s \mathcal{Q}\Omega^\dagger(s)\mathcal{Q}} \rho_{\boldsymbol{k}}\rho_{\boldsymbol{p}} \right\rangle}{N^2 S_{k'} S_{p'} N^2 S_k S_p}, \tag{2.53}$$

where the vertex functions are,

$$V^{(1)}_{\boldsymbol{k'},\boldsymbol{p'}} = \langle [\boldsymbol{\kappa}(t) : \hat{\boldsymbol{\sigma}}]\, \mathcal{Q}\rho_{\boldsymbol{k'}}\rho_{\boldsymbol{p'}}\rangle = \boldsymbol{\kappa}(t') : \boldsymbol{k'} \otimes \boldsymbol{p'} \frac{\mathrm{d}S_{k'}}{k'\mathrm{d}k'}\delta_{\boldsymbol{k'},-\boldsymbol{p'}} \tag{2.54}$$

$$V^{(2)}_{\boldsymbol{k},\boldsymbol{p}} = \left\langle \rho^*_{\boldsymbol{k}}\rho^*_{\boldsymbol{p}}\mathcal{Q}\hat{\boldsymbol{\sigma}}\right\rangle = \boldsymbol{k}\otimes\boldsymbol{p}\frac{\mathrm{d}S_k}{k'\mathrm{d}k}\delta_{\boldsymbol{k},-\boldsymbol{p}}. \tag{2.55}$$

The four-point correlation function is approximated as a product of two-time correlation functions and regarding the fact, that the density modes are the slow variables, the $\mathcal{Q}$-projected dynamics is approximated with the full dynamics. This is done under the assumption, that the fast variations will not make relevant contributions. The result of these approximation reads,

$$\frac{\left\langle \rho^*_{\boldsymbol{k'}}\rho^*_{\boldsymbol{p'}} e^{\int_{t'}^t \mathrm{d}s\mathcal{Q}\Omega^\dagger(s)\mathcal{Q}}\rho_{\boldsymbol{k}}\rho_{\boldsymbol{p}}\right\rangle}{N^2 S_{k'}S_{p'}N^2S_kS_p} \approx \frac{\left\langle \rho^*_{\boldsymbol{k'}} e^{\int_{t'}^t \mathrm{d}s\Omega^\dagger(s)}\rho_{\boldsymbol{k}}\right\rangle}{N^2S_{k'}S_k}\frac{\left\langle \rho^*_{\boldsymbol{k'}} e^{\int_{t'}^t \mathrm{d}s\Omega^\dagger(s)}\rho_{\boldsymbol{k}}\right\rangle}{N^2S_{k'}S_k}. \tag{2.56}$$

The expression for the stress tensor can be written as,

$$\boldsymbol{\sigma}(t) = \sum_{\substack{\boldsymbol{k}>\boldsymbol{p}\\ \boldsymbol{k'}>\boldsymbol{p'}}} \frac{1}{V}\int_0^t \mathrm{d}t' V^{(1)}_{\boldsymbol{k'},\boldsymbol{p'}}V^{(2)}_{\boldsymbol{k},\boldsymbol{p}}\frac{\left\langle \rho^*_{\boldsymbol{k'}} e^{\int_{t'}^t \mathrm{d}s\Omega^\dagger(s)}\rho_{\boldsymbol{k}}\right\rangle}{N^2S_{k'}S_k}\frac{\left\langle \rho^*_{\boldsymbol{k'}} e^{\int_{t'}^t \mathrm{d}s\Omega^\dagger(s)}\rho_{\boldsymbol{k}}\right\rangle}{N^2S_{k'}S_k}. \tag{2.57}$$

Translational invariance can only be conserved in this approximation for the constraint, $\boldsymbol{k'} = \boldsymbol{k}(t,t')$. Rewriting the upper expression with evaluation of the Kronecker-δs and replacing the summation over discrete wave–vectors by an wave–vector integration yields,

$$\boldsymbol{\sigma}(t) = \int_0^t \mathrm{d}t' \int \frac{\mathrm{d}^3k}{2\,(2\pi)^3}\frac{V^{(1)}_{\boldsymbol{k}(t,t'),\boldsymbol{k}(t,t')}V^{(2)}_{\boldsymbol{k},\boldsymbol{k}}}{S_k^2}\left(\frac{\left\langle \rho^*_{\boldsymbol{k}(t,t')} e^{\int_{t'}^t \mathrm{d}s\Omega^\dagger(s)}\rho_{\boldsymbol{k}}\right\rangle}{NS_{k(t,t')}}\right)^2 \tag{2.58}$$

$$= \int_0^t \mathrm{d}t' \int \frac{\mathrm{d}^3k}{2\,(2\pi)^3}\boldsymbol{k}(t,t')\boldsymbol{\kappa}(t')\boldsymbol{k}(t,t')\frac{\boldsymbol{k}\otimes\boldsymbol{k}}{kk(t,t')}\frac{S'_kS'_{k(t,t')}}{S_k^2}\phi^2_{k(t,t')}(t,t'). \tag{2.59}$$

2.3.5. Transient density correlation functions

In the last equation, eq. (2.59), the transient density correlation function is defined as,

$$\phi_{\boldsymbol{k}}(t,t') = \frac{\left\langle \rho^*_{\boldsymbol{k}} e^{\int_{t'}^t \mathrm{d}s\Omega^\dagger(s)}\rho_{\bar{\boldsymbol{k}}(t,t')}\right\rangle}{NS_k}. \tag{2.60}$$

In order to describe the density correlation functions, which remain invariant under spacial translations, it is necessary to introduce the advected density fluctuations,

$$\left|\rho_{\bar{\boldsymbol{k}}(t,t')}\right\rangle = e_{+}^{-\int_{t'}^{t} \mathrm{d}s\delta\Omega^{\dagger}(s)} \left|\rho_{\boldsymbol{k}}\right\rangle, \tag{2.61}$$

with the adjoint operator,

$$\delta\Omega^{\dagger}(t) = \sum_{i} \boldsymbol{r}_i \cdot \boldsymbol{\kappa}^{T}(t) \cdot \boldsymbol{\nabla}_i. \tag{2.62}$$

Analogously to eq. (2.61), the authors of ref. [14] define,

$$\left\langle\rho_{\bar{\boldsymbol{k}}^{*}(t,t')}\right| = \left\langle\rho_{\boldsymbol{k}}\right| e_{-}^{\int_{t'}^{t} \mathrm{d}s\overline{\delta\Omega^{\dagger}}(s)}, \tag{2.63}$$

where the advection operator acts to the left and the operator, $\overline{\delta\Omega^{\dagger}}(t)$, has to be chosen as,

$$\overline{\delta\Omega^{\dagger}}(t) = \sum_{i} \boldsymbol{r}_i \cdot \boldsymbol{\kappa}^{T}(t) \cdot (\boldsymbol{\nabla}_i + \boldsymbol{F}_i), \tag{2.64}$$

to obtain the scalar product as wanted,

$$\langle f_{\boldsymbol{k}}^{*} | g_{\boldsymbol{k}} \rangle = \int \mathrm{d}\Gamma\ \psi_{\mathrm{eq}} f_{\boldsymbol{k}}^{*}(\Gamma) g_{\boldsymbol{k}}(\Gamma). \tag{2.65}$$

With the propagator,

$$U(t,t') = e_{-}^{\int_{t'}^{t} \mathrm{d}s\Omega^{\dagger}(s)} e_{+}^{-\int_{t'}^{t} \mathrm{d}s\delta\Omega^{\dagger}(s)}, \tag{2.66}$$

it is possible to write the transient density correlation function,

$$\phi_{\boldsymbol{k}}(t,t') = \frac{\left\langle \rho_{\boldsymbol{k}}^{*} e_{-}^{\int_{t'}^{t} \mathrm{d}s\Omega^{\dagger}(s)} \rho_{\bar{\boldsymbol{k}}(t,t')} \right\rangle}{NS_k} = \frac{\langle \rho_{\boldsymbol{k}}^{*} U(t,t') \rho_{\boldsymbol{k}} \rangle}{NS_k}. \tag{2.67}$$

Using time–dependent projection operators,

$$\mathcal{P}(t,t') = \sum_{\boldsymbol{k}} \left|\rho_{\bar{\boldsymbol{k}}(t,t')}\right\rangle \left\langle\rho_{\bar{\boldsymbol{k}}(t,t')}^{*}\right| \tag{2.68}$$

$$\mathcal{Q}(t,t') = 1 - \mathcal{P}(t,t'), \tag{2.69}$$

the authors of ref. [14] find the following Zwanzig–Mori equation for the transient density correlation function,

$$\partial_t \phi_{\boldsymbol{k}}(t,t') + \Gamma_{\boldsymbol{k}}(t,t')\phi_{\boldsymbol{k}}(t,t') + \int_{t'}^{t} \mathrm{d}s M_{\boldsymbol{k}}(t,s,t')\phi_{\boldsymbol{k}}(s,t') = \Delta_{\boldsymbol{k}}(t,t'). \tag{2.70}$$

A remainder term, $\Delta_{\boldsymbol{k}}(t,t')$, will not be discussed in this section. The initial decay rate $\Gamma_{\boldsymbol{k}}(t,t')$ depends on a Hermitian operator, $\Omega_a^\dagger(t,t')$,

$$\Gamma_{\boldsymbol{k}}(t,t') = -\frac{\left\langle \rho_{\boldsymbol{k}}^* \Omega_a^\dagger(t,t') \rho_{\boldsymbol{k}} \right\rangle}{N S_{\bar{k}(t,t')}} = \frac{\bar{k}^2(t,t')}{S_{\bar{k}(t,t')}}, \tag{2.71}$$

with the operator,

$$\Omega_a^\dagger(t,t') = e_-^{\int_{t'}^t \mathrm{d}s \overline{\delta\Omega^\dagger}(s)} \Omega_{\mathrm{eq}}^\dagger e_+^{-\int_{t'}^t \mathrm{d}s \delta\Omega^\dagger(s)}. \tag{2.72}$$

The memory kernel can be written as,

$$M_{\boldsymbol{k}}(t,s,t') = -\frac{\left\langle \rho_{\boldsymbol{k}}^* \Omega_a^\dagger(s,t') e_-^{\int_s^t \mathrm{d}s' \mathcal{G}(s',t')} \mathcal{G}(t,t') \rho_{\boldsymbol{k}} \right\rangle}{N S_{\bar{k}(s,t')}}, \tag{2.73}$$

using the operator,

$$\mathcal{G}(t,t') = e_-^{\int_{t'}^t \mathrm{d}s \delta\Omega^\dagger(s)} \mathcal{Q}(t,t') \Omega_{\mathrm{eq}}^\dagger e_+^{-\int_{t'}^t \mathrm{d}s \delta\Omega^\dagger(s)}. \tag{2.74}$$

2.3.6. Generalized friction kernel

In order to express the dynamics in terms of a generalized friction kernel, $m_{\boldsymbol{k}}(t,s,t')$, the authors of ref. [14] perform a split of the dynamics into a reducible and an irreducible part following Chichocki and Hess [15]. A discussion, why this step is performed, can be found in ref. [16]. Starting with the time derivative of the propagator $\tilde{U}(t,s,t') = e_-^{\int_s^t \mathrm{d}s' \mathcal{G}(s',t')}$,

$$\partial_t \tilde{U}(t,s,t') = \tilde{U}(t,s,t') \mathcal{G}(t,t'), \tag{2.75}$$

$\mathcal{G}(t,t')$ is split using the non–Hermitian, time–dependent projection operators

$$\tilde{\mathcal{P}}(t,t') = \sum_{\boldsymbol{k}} |\rho_{\boldsymbol{k}}\rangle \frac{1}{\left\langle \rho_{\boldsymbol{k}}^* \Omega_a^\dagger(t,t') \rho_{\boldsymbol{k}} \right\rangle} \left\langle \rho_{\boldsymbol{k}}^* \Omega_a^\dagger(t,t') \right|, \tag{2.76}$$

$$\tilde{\mathcal{Q}}(t,t') = 1 - \tilde{\mathcal{P}}(t,t'), \tag{2.77}$$

$$\partial_t \tilde{U}(t,s,t') = \tilde{U}(t,s,t') \mathcal{G}(t,t') \tag{2.78}$$

$$= \tilde{U}(t,s,t') \mathcal{G}(t,t') \left(\tilde{\mathcal{P}}(t,t') + \tilde{\mathcal{Q}}(t,t') \right) \tag{2.79}$$

$$= \tilde{U}(t,s,t') \mathcal{G}_{\mathrm{red}}(t,t') + \tilde{U}(t,s,t') \mathcal{G}_{\mathrm{irr}}(t,t'). \tag{2.80}$$

The term $\tilde{U}(t,s,t')\mathcal{G}_{\mathrm{red}}(t,t')$ is treated like an inhomogeneity to solve the equation,

$$\tilde{U}(t,s,t') = e_-^{\int_s^t \mathrm{d}s' \, \mathcal{G}_{\mathrm{irr}}(s',t')} + \int_s^t \mathrm{d}t'' \, \tilde{U}(t'',s,t') \mathcal{G}_{\mathrm{red}}(t'',t') e_-^{\int_{t''}^t \mathrm{d}s' \, \mathcal{G}_{\mathrm{irr}}(s',t')}. \tag{2.81}$$

To obtain the generalized friction kernel, the authors then take matrix elements by multiplying the term, $\langle B_{\boldsymbol{k}}^*(s,t')| = \left\langle \rho_{\boldsymbol{k}}^* \Omega_a^\dagger(s,t') \right|$, from the left and the term,$|A_{\boldsymbol{k}}(t,t')\rangle = |\mathcal{G}(t,t')\rho_{\boldsymbol{k}}\rangle$,

from the right,

$$\left\langle B^*_{\boldsymbol{k}}(s,t')\tilde{U}(t,s,t')A_{\boldsymbol{k}}(t,t')\right\rangle = \left\langle B^*_{\boldsymbol{k}}(s,t')e_-^{\int_s^t \mathrm{d}s'\ \mathcal{G}_{\mathrm{irr}}(s',t')}A_{\boldsymbol{k}}(t,t')\right\rangle \tag{2.82}$$

$$+\int_s^t \mathrm{d}t''\ \left\langle B^*_{\boldsymbol{k}}(s,t')\tilde{U}(t'',s,t')\mathcal{G}_{\mathrm{red}}(t'',t')e_-^{\int_{t''}^t \mathrm{d}s'\ \mathcal{G}_{\mathrm{irr}}(s',t')}A_{\boldsymbol{k}}(t,t')\right\rangle \tag{2.83}$$

and with the generalized friction kernel,

$$m_{\boldsymbol{k}}(t,s,t') = \frac{\left\langle B^*_{\boldsymbol{k}}(s,t')e_-^{\int_s^t \mathrm{d}s'\ \mathcal{G}_{\mathrm{irr}}(s',t')}A_{\boldsymbol{k}}(t,t')\right\rangle}{NS_{\bar{\boldsymbol{k}}(s,t')}\Gamma_{\boldsymbol{k}}(s,t')\Gamma_{\boldsymbol{k}}(t,t')}, \tag{2.84}$$

the following relation between diffusion and friction kernel is obtained,

$$M_{\boldsymbol{k}}(t,s,t') = -\Gamma_{\boldsymbol{k}}(s,t')m_{\boldsymbol{k}}(t,s,t')\Gamma_{\boldsymbol{k}}(t,t') - \int_s^t \mathrm{d}t''\ M_{\boldsymbol{k}}(t'',s,t')m_{\boldsymbol{k}}(t,t'',t')\Gamma_{\boldsymbol{k}}(t,t'). \tag{2.85}$$

Eq. (2.70) is rewritten as a Volterra equation of the second kind,

$$\phi_{\boldsymbol{k}}(t,t') = -\frac{1}{\Gamma_{\boldsymbol{k}}(t,t')}\int_{t'}^t \mathrm{d}s\ M_{\boldsymbol{k}}(t,s,t')\phi_{\boldsymbol{k}}(s,t') - \frac{1}{\Gamma_{\boldsymbol{k}}(t,t')}\left(\frac{\partial}{\partial t}\phi_{\boldsymbol{k}}(t,t') - \Delta_{\boldsymbol{k}}(t,t')\right), \tag{2.86}$$

and the second term is treated as an inhomogeneity, to finally yield the following form of the equation of motion,

$$\partial_t\phi_{\boldsymbol{k}}(t,t') + \Gamma_{\boldsymbol{k}}(t,t')\left(\phi_{\boldsymbol{k}}(t,t') + \int_{t'}^t \mathrm{d}s\ m_{\boldsymbol{k}}(t,s,t')\partial_{t'}\phi_{\boldsymbol{k}}(s,t')\right) = \tilde{\Delta}_{\boldsymbol{k}}(t,t'). \tag{2.87}$$

The remainder term on the right hand side is identified as,

$$\tilde{\Delta}_{\boldsymbol{k}}(t,t') = \frac{1}{S_k}\left\langle \rho^*_{\boldsymbol{k}}e_-^{\int_s^t \mathrm{d}s'\ \mathcal{G}_{\mathrm{irr}}(s',t')}\mathcal{G}(t,t')\rho_{\boldsymbol{k}}\right\rangle. \tag{2.88}$$

To express the memory kernel as a functional of the transient density correlation functions, the propagator is approximated,

$$e_-^{\int_s^t \mathrm{d}s'\ \mathcal{G}_{\mathrm{irr}}(s',t')} \approx e_-^{\int_s^t \mathrm{d}s'\ \mathcal{G}_{\mathcal{Q}}(s',t')\tilde{\mathcal{Q}}(s',t')}, \tag{2.89}$$

with the operator, $\mathcal{G}_{\mathcal{Q}}(t,t') = e_-^{\int_{t'}^t \mathrm{d}s\overline{\delta\Omega^\dagger}(s)}\mathcal{Q}(t,t')\Omega^\dagger_{\mathrm{e}}e_+^{-\int_{t'}^t \mathrm{d}s\delta\Omega^\dagger(s)}$. This approximation is motivated by setting two strain energy operators to zero. The authors of ref. [14] argue, that this is necessary and give further insight in their motivation.

The remainder term vanishes, when the same approximation is applied. A second approx-

imation, following from the same argument,

$$e_+^{-\int_{t'}^{s}\mathrm{d}s'\delta\Omega^\dagger(s')} \approx e_+^{-\int_{t'}^{s}\mathrm{d}s'\overline{\delta\Omega^\dagger}(s')}, \tag{2.90}$$

is applied to the memory kernel, that reads after these approximations,

$$m_{\boldsymbol{k}}(t,s,t') = \frac{\left\langle \rho^*_{\bar{\boldsymbol{k}}(s,t')}\Omega_e^\dagger\mathcal{Q}(s,t')e_+^{-\int_{t'}^{s}\mathrm{d}s'\overline{\delta\Omega^\dagger}(s')}e_-^{\int_{s}^{t}\mathrm{d}s'\,\mathcal{G}_\mathcal{Q}(s',t')\tilde{\mathcal{Q}}(s',t')}e_-^{\int_{t'}^{t}\mathrm{d}s\delta\Omega^\dagger(s)}\mathcal{Q}(t,t')\Omega_e^\dagger\rho_{\boldsymbol{k}}\right\rangle}{NS_{\bar{\boldsymbol{k}}(s,t')}\Gamma_{\boldsymbol{k}}(s,t')\Gamma_{\boldsymbol{k}}(t,t')}. \tag{2.91}$$

With the time–dependent projection operator onto density pairs,

$$\mathcal{P}_2(t,t') = \sum_{\boldsymbol{q}>\boldsymbol{p}} \frac{\left|\rho_{\bar{\boldsymbol{q}}(t,t')}\rho_{\bar{\boldsymbol{p}}(t,t')}\right\rangle\left\langle\rho^*_{\bar{\boldsymbol{q}}(t,t')}\rho^*_{\bar{\boldsymbol{p}}(t,t')}\right|}{N^2S_{\bar{\boldsymbol{q}}(t,t')}S_{\bar{\boldsymbol{p}}(t,t')}}, \tag{2.92}$$

the numerator of the memory kernel is approximated,

$$\left\langle \rho^*_{\bar{\boldsymbol{k}}(s,t')}\Omega_e^\dagger\mathcal{Q}(s,t')\mathcal{P}_2(s,t')e_+^{-\int_{t'}^{s}\mathrm{d}s'\overline{\delta\Omega^\dagger}(s')}e_-^{\int_{s}^{t}\mathrm{d}s'\,\mathcal{G}_\mathcal{Q}(s',t')\tilde{\mathcal{Q}}(s',t')}e_-^{\int_{t'}^{t}\mathrm{d}s\delta\Omega^\dagger(s)}\mathcal{P}_2(t,t')\mathcal{Q}(t,t')\Omega_e^\dagger\rho_{\boldsymbol{k}}\right\rangle \tag{2.93}$$

$$\approx \sum_{\substack{\boldsymbol{q}>\boldsymbol{p},\\ \boldsymbol{q}'>\boldsymbol{p}'}} \frac{V^{(1)}_{\boldsymbol{kqp}}(s,t')V^{(2)}_{\boldsymbol{kq'p'}}(t,t')}{N^2}\left\langle \rho^*_{\bar{\boldsymbol{q}}(t,t')}\rho^*_{\bar{\boldsymbol{p}}(t,t')}e_+^{-\int_{t'}^{s}\mathrm{d}s'\overline{\delta\Omega^\dagger}(s')}e_-^{\int_{s}^{t}\mathrm{d}s'\,\mathcal{G}_\mathcal{Q}(s',t')\tilde{\mathcal{Q}}(s',t')}e_-^{\int_{t'}^{t}\mathrm{d}s\delta\Omega^\dagger(s)}\rho_{\bar{\boldsymbol{q}}(t,t')}\rho_{\bar{\boldsymbol{p}}(t,t')}\right\rangle, \tag{2.94}$$

with the vertex functions,

$$V^{(1)}_{\boldsymbol{kqp}}(s,t') = \frac{\left\langle \rho^*_{\bar{\boldsymbol{k}}(s,t')}\Omega_e^\dagger\mathcal{Q}(s,t')\rho_{\bar{\boldsymbol{q}}(s,t')}\rho_{\bar{\boldsymbol{p}}(s,t')}\right\rangle}{NS_{\bar{\boldsymbol{q}}(s,t')}S_{\bar{\boldsymbol{p}}(s,t')}}, \tag{2.95}$$

$$V^{(2)}_{\boldsymbol{kq'p'}}(t,t') = \frac{\left\langle \rho^*_{\bar{\boldsymbol{q}}'(t,t')}\rho^*_{\bar{\boldsymbol{p}}'(t,t')}\mathcal{Q}(t,t')\Omega_e^\dagger\rho_{\bar{\boldsymbol{k}}'(t,t')}\right\rangle}{NS_{\bar{\boldsymbol{q}}'(t,t')}S_{\bar{\boldsymbol{p}}'(t,t')}}. \tag{2.96}$$

Using the Ornstein–Zernike direct correlation function [17],

$$c_q = \frac{1}{\rho}\left(1-\frac{1}{S_q}\right), \tag{2.97}$$

with the particle number density, $\rho = N/V$, and the factorization approximation for triplet

static structure factors, $S_{kqp} \approx S_k S_q S_p$, the vertices are expressed as,

$$V^{(1)}_{\boldsymbol{kqp}}(s,t') = \bar{\boldsymbol{k}}(s,t') \left(\bar{\boldsymbol{q}}(s,t') c_{\bar{q}(s,t')} + \bar{\boldsymbol{p}}(s,t') c_{\bar{p}(s,t')} \right) \rho \delta_{\bar{\boldsymbol{k}},\bar{\boldsymbol{q}}+\bar{\boldsymbol{p}}}, \tag{2.98}$$

$$V^{(2)}_{\boldsymbol{kq'p'}}(t,t') = \bar{\boldsymbol{k}}'(t,t') \left(\bar{\boldsymbol{q}}'(s,t') c_{\bar{q}'(s,t')} + \bar{\boldsymbol{p}}(s,t') c_{\bar{p}'(s,t')} \right) \rho \delta'_{\bar{\boldsymbol{k}}',\bar{\boldsymbol{q}}'+\bar{\boldsymbol{p}}}. \tag{2.99}$$

Again the four–point correlation function is split into two–point correlation functions and the $\mathcal{Q}$–projected irreducible dynamics are replaced by the full dynamics,

$$\left\langle \rho^*_{\bar{\boldsymbol{q}}(t,t')} \rho^*_{\bar{\boldsymbol{p}}(t,t')} e_+^{-\int_{t'}^{s} \mathrm{d}s' \overline{\delta\Omega^\dagger}(s')} e_-^{\int_{s}^{t} \mathrm{d}s' \, \mathcal{G}_{\mathcal{Q}}(s',t') \bar{\mathcal{Q}}(s',t')} e_-^{\int_{t'}^{t} \mathrm{d}s \delta\Omega^\dagger(s)} \rho_{\bar{\boldsymbol{q}}(t,t')} \rho_{\bar{\boldsymbol{p}}(t,t')} \right\rangle \tag{2.100}$$

$$\approx N^2 S_{\bar{\boldsymbol{q}}(s,t')} S_{\bar{\boldsymbol{p}}(s,t')} \phi_{\bar{\boldsymbol{k}}(s,t')}(t,s) \phi_{\bar{\boldsymbol{p}}(s,t')}(t,s) \delta_{\boldsymbol{q},\boldsymbol{q}'} \delta_{\boldsymbol{k},\boldsymbol{k}'}. \tag{2.101}$$

This gives the memory kernel in its final approximation,

$$m_{\boldsymbol{k}}(t,s,t') = \frac{\rho}{16\pi^3} \int \mathrm{d}q^3 \frac{S_{\bar{\boldsymbol{k}}(t,t')} S_{\bar{\boldsymbol{q}}(s,t')} S_{\bar{\boldsymbol{p}}(s,t')}}{\bar{k}^2(s,t') \bar{k}^2(t,t')} V^{(1)}_{\boldsymbol{kqp}}(s,t') V^{(2)}_{\boldsymbol{kqp}}(t,t') \phi_{\bar{\boldsymbol{q}}(s,t')}(t,s) \phi_{\bar{\boldsymbol{p}}(s,t')}(t,s), \tag{2.102}$$

with the integration over $\boldsymbol{q}$–space carried out under the restriction, $\boldsymbol{p} = \boldsymbol{q} - \boldsymbol{k}$.

2.3.7. Glass transition

Without flow, viz. $\boldsymbol{\kappa} = \boldsymbol{0}$, the memory kernel is equivalent to the kernel in quiescent MCT [18]. In the long–time limit, the solutions of eq. (2.87),

$$\lim_{t\to\infty} \phi_{\boldsymbol{k}}(t) = f_{\boldsymbol{k}}, \tag{2.103}$$

$$\lim_{t\to\infty} m_{\boldsymbol{k}}(t,0,0) = \mathcal{F}(f), \tag{2.104}$$

fulfill the following equation [12],

$$\mathcal{F}(f) = \frac{f_{\boldsymbol{k}}}{1 - f_{\boldsymbol{k}}}. \tag{2.105}$$

With the Percus–Yevick structure factor for hard spheres [19, 20], this equation has a bifurcation at a critical packing fraction, $\varphi_c = 0.517$, when aside from the trivial solution, $f_{\boldsymbol{k}} = 0$, a finite solution, $f^c_{\boldsymbol{k}}$, occurs.

A finite solution, $f^c_{\boldsymbol{k}}$, in the asymptotic limit, $t \to \infty$, means that the density fluctuations have not completely decorrelated, even after infinite time. Fourier back transformation to real space can show [21], that the correlation of the asymptotic position and its initial position does not vanish in a small region around it,

$$f(\boldsymbol{r}) = \int \frac{\mathrm{d}^3 q}{(2\pi)^3} e^{-i\boldsymbol{q}\boldsymbol{r}} f_{\boldsymbol{q}}. \tag{2.106}$$

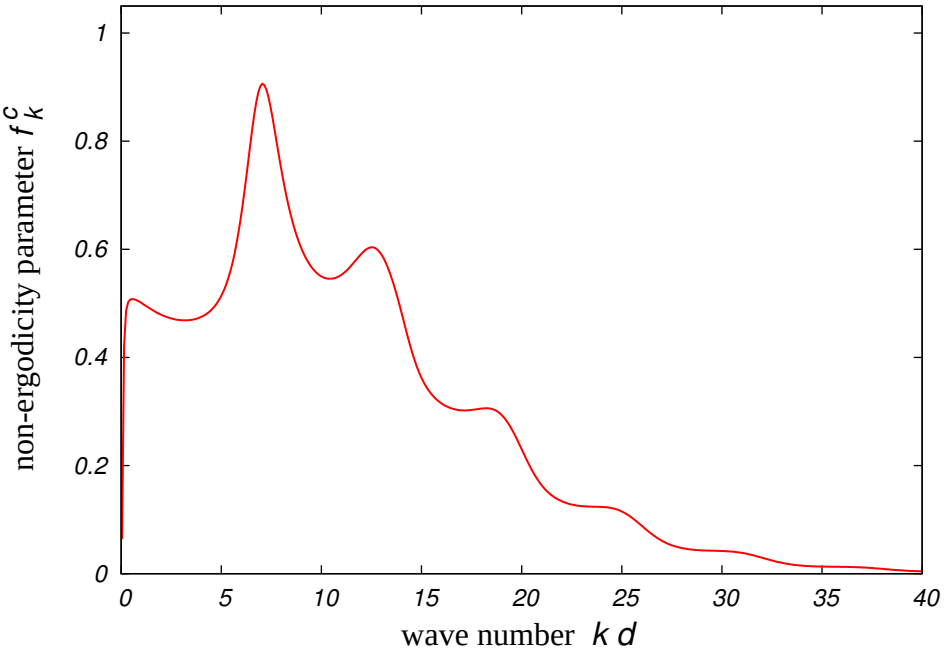

Figure 2.1.: Finite asymptotic solutions for the density correlators, $f_{\boldsymbol{k}}^c$, as functions of their wave number ,$k = |\boldsymbol{k}|$. The results have been computed on a quasi one–dimensional $\boldsymbol{k}$–grid with the wave–number times particle diameter, kd, running from 0.2 to 39.8 with step size, $\Delta h = 0.4$, using the Percus–Yevick structure factor for hard spheres and the Ornstein–Zernike direct correlation functions at a packing fraction, $\varphi = 0.52$.

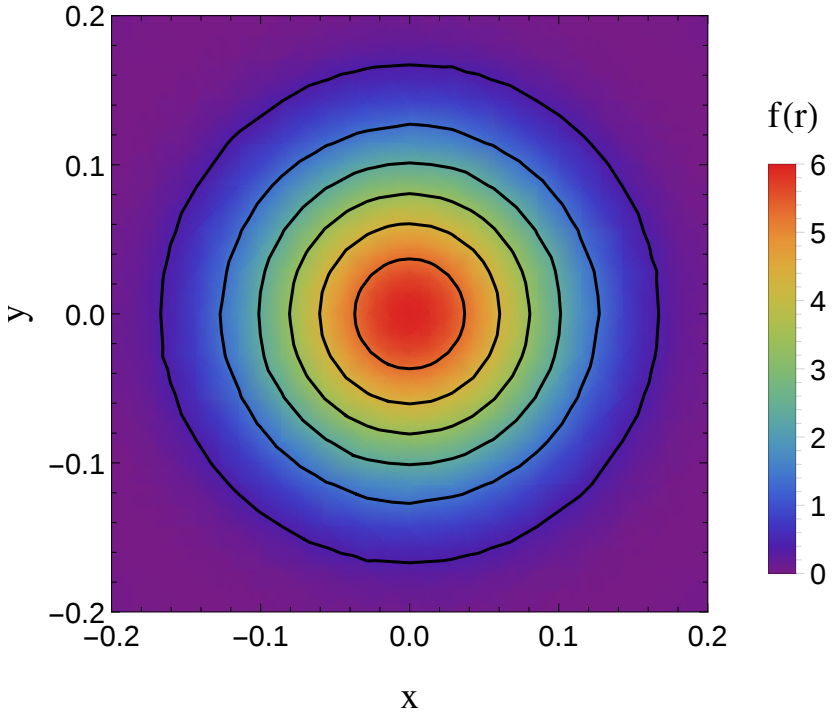

Figure 2.2.: Density plot of the Fourier transform of the non–ergodicity parameter, $f(\boldsymbol{r})$, in the x, y–plane. Black contour lines mark steps of 1 for the function, $f(\boldsymbol{r})$.

The nonvanishing collective probability around the initial position is shown in fig. 2.2, the Fourier transform of the non–ergodicity parameter, $f(\boldsymbol{r})$ can be understood as a collective probability for each particle to have moved by the vector, $\boldsymbol{r}$, from its initial position. This gives rise to a picture of interpretation, that each particle is caged by its neighboring particles (fig. 2.3). In a fluid, a particle will explore its own entire phase space. In the asymptotic limit, density correlation have to vanish. In contrast, the finite solutions, $f_{\boldsymbol{k}} \neq 0$, imply that the ergodicity is broken. Therefore $f_{\boldsymbol{k}}$ are also called non–ergodicity parameters.

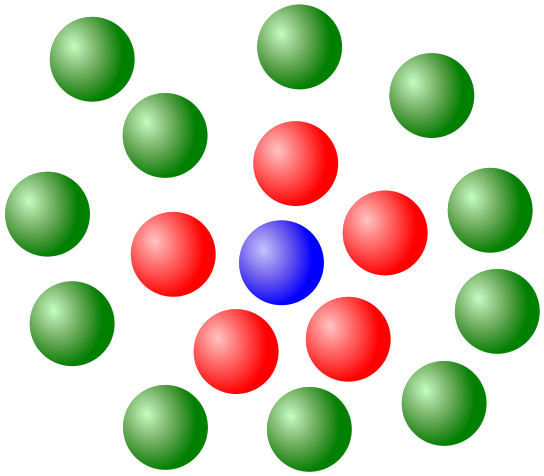

Figure 2.3.: Schematic illustration of the caging effect. Each single particle (e.g. the blue particle) is surrounded by its neighbors (red), which constrain the blue particle's available phase space.

2.3.8. β–scaling

At small distances from the critical density of the glass transition, $\varepsilon \propto \frac{\varphi_c - \varphi}{\varphi_c}$, the equation for the nonergodicity parameter, eq. (2.105), has two solutions [18],

$$f_q = f_q^c \pm (1 - f_c)^2 \sqrt{\frac{\varepsilon}{1-\lambda}} e_q^c, \tag{2.107}$$

which coalesce at the critical density, $\varepsilon = 0$. This bifurcation of the solutions is a cusp singularity [22]. A more detailed discussion on bifurcation theory and catastrophe theory can be found in [23].

In ref. [18], a proof is given, that the set of coupled equations for the slow variables, eq. (2.87), reduces to an equation for a single scalar function. The time evolution is determined by a single dangerous mode.

Consequently, one can factorize the density correlation function close to the glass transition [24],

$$\phi_{\boldsymbol{q}}(t) - f_{\boldsymbol{q}}^c = h_{\boldsymbol{q}} \cdot \mathcal{G}(t), \tag{2.108}$$

into an amplitude, $h_{\boldsymbol{q}}$, and the scaling function, $\mathcal{G}(t)$. This scaling function, $\mathcal{G}(t)$, has been studied for the quiescent model [25], an isotropic approximation of MCT–ITT [13] and, regarding also the anisotropy, for MCT–ITT [26]. Up to the orders, ε, $(\dot\gamma t)^2$, the scaling function, $\mathcal{G}(t)$, solves the following β-scaling function,

$$\varepsilon - c^{\dot\gamma}(\dot\gamma t)^2 + \lambda \mathcal{G}^2(t) = \frac{\mathrm{d}}{\mathrm{d}t} \int_0^\infty \mathrm{d}t' \mathcal{G}(t - t')\mathcal{G}(t'). \tag{2.109}$$

This equation is valid only for a constant shear rate. In the quiescent MCT the summand, $c^{\dot\gamma}(\dot\gamma t)^2$, vanishes. For any shear flow, which breaks time–translational symmetry, the equation above does not hold. The scaling function for time–dependent flow, $\mathcal{G}(t,t')$, depends on two time parameters. But within time regimes, when the shear flow can be approximated by any time–translational invariant version, viz. for negligible small accumulated strains, $\gamma(t,t') \ll 1$, or within time regimes of steady flow, $\gamma(t,t') = \dot\gamma\ (t-t')$, the time–translational symmetric equation, eq. (2.109), is a valid approximation.

2.4. Schematic $\mathsf{F}_{12}^{(\dot\gamma)}$–model

In the previous section, I discussed that close to the glass transition, the dynamics can be described with a single scalar time–dependent function, $\mathcal{G}(t)$. This motivates the replacement of the full, $\boldsymbol{q}$–vector dependent dynamics by a scalar model, which provides the same scaling as in eq. (2.109).

One example of such a scalar model is the schematic $F_{12}^{(\dot\gamma)}$–model. The schematic model simplifies the mode coupling equations by restricting them to a single normalized mode, $\phi(t,t')$. This single mode solves an equation of a similar form as eq. (2.87),

$$\partial_t \phi(t,t') + \Gamma \left(\phi(t,t') + \int_{t'}^{t} \mathrm{d}t'' m(t,t'',t') \partial_{t'} \phi(t'',t') \right) = 0. \tag{2.110}$$

The initial conditions at the time, $t = t'$, are

$$\phi(t,t) = 1, \tag{2.111}$$

$$\partial_t \phi(t,t')|_{t=t'} = -\Gamma. \tag{2.112}$$

The memory kernel is a functional of the correlator, $m(t) = \mathcal{F}[\phi]$. The $F_{12}^{(\dot\gamma)}$–model without shear, $\dot\gamma = 0$, uses a polynomial ansatz with a linear and a quadratic coupling [27], in order to capture the shear–induced loss of memory caused by shear advection of the vertices in eqs. (2.98), (2.99), the model is extended to include the h–functions [28],

$$m(t,t'',t') = h_1(t,t') h_2(t,t'') h_3(t'',t') \left(\nu_1 \phi(t,t'') + \nu_2 \phi^2(t,t'') \right). \tag{2.113}$$

Without shear, the h–functions are equal to one and the schematic model of quiescent MCT is recovered. This model has been studied in detail in refs. [27, 18].

The parameters, ν_1, and ν_2, are chosen as,

$$\nu_1 = 2\sqrt{2} - 2 + \varepsilon \frac{f_c}{1-f_c}, \tag{2.114}$$

$$\nu_2 = 2. \tag{2.115}$$

This set ensures, that in the absence of shear, the schematic model features at the separation parameter, $\varepsilon = 0$, a type B glass transition [27]. This is the same type found in MCT for hard–spheres at the critical packing fraction [25].

As in previous implementations of the schematic model [28], I set the function, h_3, to unity. In order to be consistent with the schematic model employed for steady shear [29, 30, 31, 32], I set the function, h_1, to unity as well, repeating the choice that was made in ref. [33]. The h–function is defined as,

$$h_2(t,t') = \frac{\gamma_c^2}{\gamma_c^2 + \gamma(t,t')}, \tag{2.116}$$

with the accumulated strain, $\gamma(t,t') = \int_{t'}^{t} \mathrm{d}s\dot{\gamma}(s)$, and a strain scale, γ_c, which sets the scale for the decay of the transient density correlator. This form was originally chosen because it shows for steady shear the same scaling behaviour as an isotropic approximated version of MCT–ITT [29]. A generalization of the h–functions for other types of flow than simple shear has been introduced in ref. [28].

2.4.1. β–scaling

Analogously to the previous section, one finds for the β–regime a scaling of the mode

$$\phi(t) = f_c + (1-f_c)^2\mathcal{G}(t) + \mathcal{O}(\varepsilon). \tag{2.117}$$

This ansatz leads to the following equation for the scaling function, $\mathcal{G}(t)$, up to the orders, ε, and $(\dot{\gamma}t)^2$,

$$\varepsilon - c^{\dot{\gamma}}(\dot{\gamma}t)^2 + \lambda\mathcal{G}^2(t) = \frac{d}{dt}\int_0^t dt'\, \mathcal{G}(t-t')\mathcal{G}(t'). \tag{2.118}$$

This equation is identical with the β–scaling equation of MCT–ITT, eq. (2.109). Therefore, one identifies the parameters of the schematic model, ε, λ, with the separation and the exponent parameter of MCT.

For $\varepsilon = 0$, and $\dot{\gamma} = 0$, the ansatz, $\mathcal{G}(t) = (t/t_0)^{-x}$, solves the scaling equation (2.109) under the following constraint for the exponent, x, and the exponent parameter,

$$\lambda = \frac{\Gamma^2(1-x)}{\Gamma(1-2x)}. \tag{2.119}$$

For $1/2 \leq \lambda < 1$, this transcendental equation has two solutions for the exponent, x,

$$a > 0 \qquad \text{and} \qquad 1 \geq -b > 0. \tag{2.120}$$

The parameter, λ, is called the exponent parameter, as it generates the critical exponents of

the β–relaxation. This solution is equivalent to the density correlator,

$$\phi(t,t') \approx f_c + (1-f)^2 \left(\frac{t-t'}{t_0}\right)^{-a}, \qquad \text{for short times,} \tag{2.121}$$

$$\phi(t,t') \approx f_c - (1-f)^2 \left(\frac{t-t'}{\tau_\alpha}\right)^{b}, \qquad \text{for intermediate times,} \tag{2.122}$$

with time constants, t_0, τ_α. The later is called v. Schweidler law [34].

The intrinsic time scales of the scaling equation can be analyzed by using its homogeneity properties [13]. Introducing an arbitrary scale, $\Omega > 0$, the authors of ref. [13] show, that the scaling function fulfills,

$$\mathcal{G}(t,\varepsilon,\dot\gamma) = \Omega^a \, \hat{\mathcal{G}}\left(\hat t = \frac{t}{t_0}\Omega, \hat\varepsilon = \varepsilon\Omega^{-2a}, \hat{\dot\gamma} = \dot\gamma t_0 \Omega^{-1-a}\right). \tag{2.123}$$

The following power–series ansatz,

$$\mathcal{G}(t) = t^u \sum_{n=0} \alpha_n t^{\nu n}, \tag{2.124}$$

has proven useful [35, 13, 26]. Inserting the ansatz into the scaling equation leads to,

$$\varepsilon - c^{\dot\gamma}(\dot\gamma t)^2 = \alpha_0^2 \Gamma_{0,0} t^{2u} + 2\alpha_0\alpha_1\Gamma_{0,1} t^{2u+\nu} + \sum_{n=2} t^{2u+n\nu} \sum_{n'=0}^{n} \Gamma_{n-n',n'} \alpha_{n-n'}\alpha_{n'}, \tag{2.125}$$

with the abbreviation $\Gamma_{n,n'}$ defined as

$$\Gamma_{n,n'} = \frac{\Gamma(1+u-n\nu)\Gamma(1+u+n'\nu)}{\Gamma(1+2u+(n+n')\nu)} - \lambda. \tag{2.126}$$

For glassy solutions, $\varepsilon > 0$, and without imposed shear, $\dot\gamma = 0$, choosing $u = 0$, leads to a solution. The constant term of the power series has to fulfill, $\alpha_0 = \sqrt{\frac{\varepsilon}{1-\lambda}}$. This means that the non–ergodicity parameter in the glass is [29, 31],

$$\phi(t\to\infty) = f_\varepsilon = f_c + (1-f_c)^2\sqrt{\frac{\varepsilon}{1-\lambda}}. \tag{2.127}$$

The two–parameter scaling law, eq. (2.123), defines the corresponding time scale,

$$t_\varepsilon = t_0 \varepsilon^{-\frac{1}{2a}}. \tag{2.128}$$

For fluid solutions, $\varepsilon < 0$, and without imposed shear flow, $\dot\gamma = 0$, the second solution of

eq. (2.119), b, is connected to a second power law [29, 31],

$$\mathcal{G}(t) = \left(\frac{t}{\tau_\alpha}\right)^b, \tag{2.129}$$

with the time scale, τ_α, which can be determined by the two–parameter scaling law, eq. (2.123),

$$\tau_\alpha = t_0 \hat{\tau}_0 |\varepsilon|^{-\gamma}, \tag{2.130}$$

with a second constant, τ^0, determined by numerical computation, tab. 2.1.

For a constant shear rate, $\dot{\gamma} = \text{const.}$, the scaling function merges for long times into an asymptote [29, 31],

$$\mathcal{G}(t) = -\frac{t}{\tau_{\dot{\gamma}}}, \tag{2.131}$$

with the time scale of the shear–induced decay, $\tau_{\dot{\gamma}}$, set by the shear rate,

$$\tau_{\dot{\gamma}} = \frac{1}{|\dot{\gamma}|}\sqrt{\frac{\lambda - \frac{1}{2}}{c^{(\dot{\gamma})}}}. \tag{2.132}$$

The numerical computed value of the exponent parameter for a Percus–Yevick structure factor is, $\lambda = 0.735$ [25]. For the F^{12}–model, $\lambda = \frac{1}{\sqrt{2}}$, is conventionally chosen [29]. The solutions of the transient equation are then approximately given by the values of tab. 2.1.

λ	v_1^c	v_2^c	f_c
0.707	2.00	0.828	0.293
a	b	γ	$\frac{1}{2a}$
0.324	0.629	2.34	1.54
t_0	$\hat{\tau}_0$	α^*	β^*
0.426	1.71	0.021	0.864

Table 2.1.: Parameters for the $\mathrm{F}_{12}^{(\dot{\gamma})}$–model, parameters of the first row and the critical exponents can be determined analytically in dependence of λ, the scales of the last row are found numerically and identical to the results of ref. [31] .

2.4.2. Dynamic moduli

The scaling laws can be seen in the spectra of the linear storage modulus, $G'(\omega)$, and the linear loss modulus, $G''(\omega)$, defined by,

$$G'(\omega) = \omega \int_0^\infty \mathrm{d}t' \sin(\omega t') G_{\mathrm{eq}}(t'), \tag{2.133}$$

$$G''(\omega) = \omega \int_0^\infty \mathrm{d}t' \cos(\omega t') G_{\mathrm{eq}}(t') \quad \text{or} \tag{2.134}$$

$$G'(\omega) + iG''(\omega) = i\omega \int_0^\infty \mathrm{d}t' e^{-i\omega t'} G_{\mathrm{eq}}(t'). \tag{2.135}$$

The last formula gives the moduli as real and imaginary part of the Laplace transform of the equilibrium shear modulus.

If I approximate the generalized shear modulus, $G_{\mathrm{eq}}(t)$, for the short time dynamics in accordance with the solution of the β–scaling equation,

$$G_{\mathrm{eq}}(t) \approx G_0 \left(f^2 + 2f(1-f)^2 \left(\frac{t}{t_0} \right)^{-a} \right), \tag{2.136}$$

the resulting moduli are,

$$G'(\omega) + iG''(\omega) = G_0 f^2 + 2G_0 f(1-f)^2 \left(i\omega t_0\right)^a \Gamma(1-a). \tag{2.137}$$

Analogously, I receive for the intermediate time regime with,

$$G_{\mathrm{eq}}(t) \approx G_0 f^2 - 2G_0 f(1-f)^2 \left(\frac{t}{\tau_\alpha} \right)^b, \tag{2.138}$$

the resulting moduli,

$$G'(\omega) + iG''(\omega) = G_0 f^2 - 2G_0 f(1-f)^2 \left(i\omega \tau_\alpha\right)^{-b} \Gamma(1+b). \tag{2.139}$$

The α–decay is often fitted by Kohlrausch functions [36] for longer times, as they agree with the t^{-b}–decay. For even longer times it can be fitted by an exponential,

$$G_{\mathrm{eq}}(t) \approx G_0 f^2 \exp\left(-\tilde{\alpha} \frac{t}{\tau_\alpha} \right), \tag{2.140}$$

with some constant, $\tilde{\alpha}$. The respective linear storage and loss modulus for this exponential

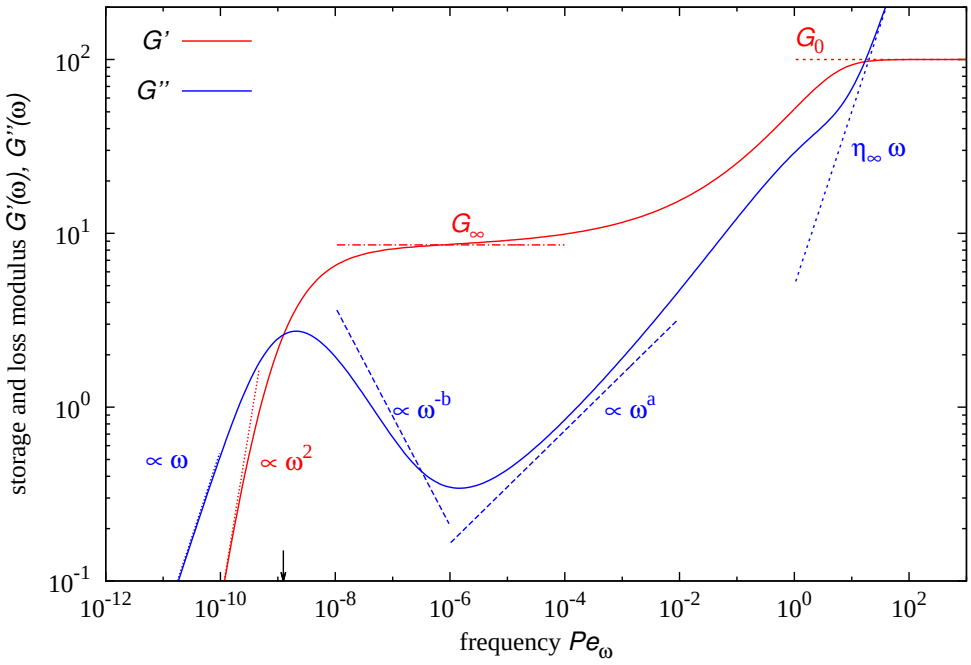

Figure 2.4.: Linear storage modulus, $G'(\omega)$, (red) and linear loss modulus, $G''(\omega)$, (blue) in the fluid regime, $\varepsilon = -10^{-4}$. The red short dashed line marks $G_0 = 100$, the red dash–dotted line marks G_∞, the red and blue dotted lines show the small–frequency approximation of eq. (2.142), the blue dashed lines show the power laws for an exponent parameter, $\lambda = \frac{1}{\sqrt{2}}$,the blue short–dashed line gives the contribution of the high–frequency viscosity, eq. (2.144).

fit are,

$$G'(\omega) + iG''(\omega) = G_0 f^2 \left(\frac{\omega^2}{\frac{\tilde{\alpha}^2}{\tau_\alpha^2} + \omega^2} + i \frac{\tilde{\alpha}}{\tau_\alpha} \frac{\omega}{\frac{\tilde{\alpha}^2}{\tau_\alpha^2} + \omega^2} \right). \tag{2.141}$$

In the lowest order, the small frequency approximation of the result above,

$$G'(\omega) + iG''(\omega) = G_0 f^2 \left(\frac{\tau_\alpha^2}{\tilde{\alpha}^2} \omega^2 + i \frac{\tau_\alpha}{\tilde{\alpha}} \omega \right), \tag{2.142}$$

with a linear storage modulus increasing quadratically in the frequency, ω, and the linear loss modulus increasing linearly in the frequency, shows a good agreement for small frequencies, $\omega \ll \frac{2\pi}{\tau_\alpha}$, with the results from the schematic model, as it is shown in fig. 2.4.

When the generalized shear modulus is extended with an additional term,

$$G_{\mathrm{eq}}(t) + \eta_\infty^\omega \delta(t), \tag{2.143}$$

the high–frequency viscosity, η_∞^ω, will add the following term to the linear loss modulus,

$$G''(\omega) + \eta_\infty^\omega \omega, \tag{2.144}$$

and does not affect the storage modulus.

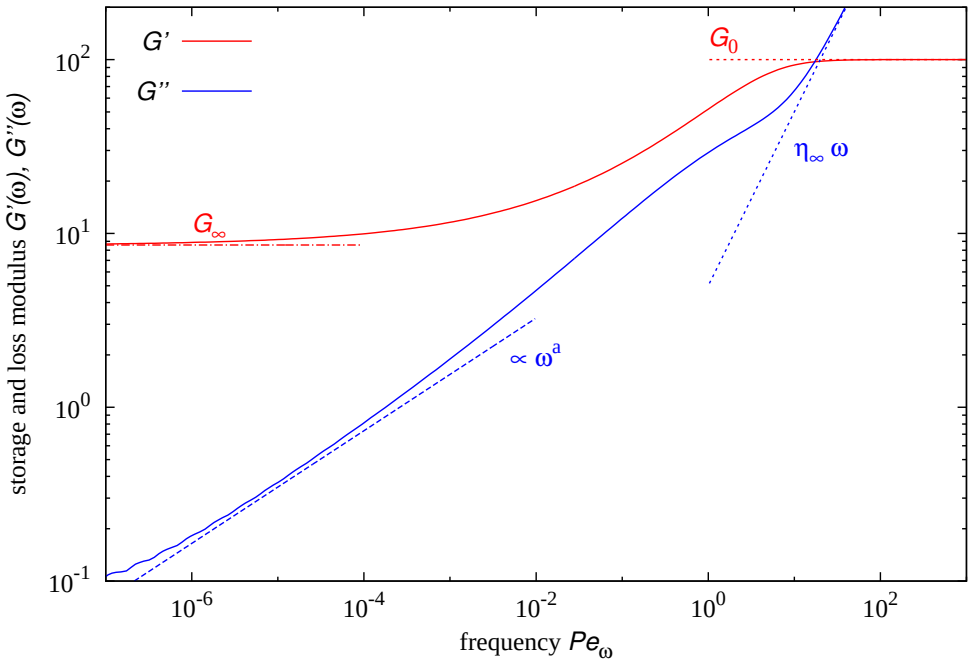

Figure 2.5.: Linear storage modulus, $G'(\omega)$, (red) and linear loss modulus, $G''(\omega)$, (blue) as they would appear in the glassy regime. These moduli have been computed with a separation parameter, $\varepsilon = -10^{-7}$, in the fluid regime for numerical efficiency, but the plot range has been restricted to the part, in which the result agrees with the moduli in the glassy regime. The red short dashed line marks $G_0 = 100$, the red dash–dotted line marks G_∞, the blue dashed line shows the power law, $G''(\omega) \propto \omega^a$, for an exponent parameter, $\lambda = \frac{1}{\sqrt{2}}$, the blue short–dashed line gives the contribution of the high–frequency viscosity, eq. (2.144).

2.4.3. Stress vertex

The transient density correlation function, $\phi^2_{\boldsymbol{k}}(t,t')$, as a function of the wave vector, $\boldsymbol{k}$, is bounded by zero and one at every time point. Therefore, one can apply the mean value theorem pointwise to the integrand in eq. (2.59). The resulting expression is mathematical identical to the stress term in eq. (2.59),

$$\boldsymbol{\sigma}(t) = \int_0^t \mathrm{d}t' \phi^2_{\tilde{\boldsymbol{k}}}(t,t') \int \frac{\mathrm{d}^3 k}{2\,(2\pi)^3} \frac{V^{(1)}_{\boldsymbol{k}(t,t'),\boldsymbol{k}(t,t')} V^{(2)}_{\boldsymbol{k},\boldsymbol{k}}}{S_k^2} \tag{2.145}$$

$$= \int_0^t \mathrm{d}t' \phi^2_{\tilde{\boldsymbol{k}}}(t,t') \int \frac{\mathrm{d}k^3}{2(2\pi)^3} \left[\frac{\partial}{\partial t'} \left(\boldsymbol{k}\cdot\mathbf{B}(t,t')\cdot\boldsymbol{k}\right)\right] \frac{\boldsymbol{k}\otimes\boldsymbol{k}}{kk(t,t')} \left[\frac{S'_k S'_{k(t,t')}}{S_k^2}\right]. \tag{2.146}$$

Because the mean modes, $\phi_{\tilde{\boldsymbol{k}}}(t,t')$, are obtained pointwise, their time dependence is unknown. But the time dependence of the stress integral can be approximated. For simple shear, the off–diagonal σ_{xy}–element of the stress tensor is of interest,

$$\sigma_{xy}(t) = \int_0^t \mathrm{d}t' \int \frac{\mathrm{d}k^3}{2(2\pi)^3} \dot{\gamma}(t') \frac{k_x^2 k_y(t,t') k_y}{kk(t,t')} \left[\frac{S'_k S'_{k(t,t')}}{S_k^2}\right] \phi^2_{\boldsymbol{k}(t,t')}(t,t') \tag{2.147}$$

$$= \int_0^t \mathrm{d}t' \int \frac{\mathrm{d}k^3}{2(2\pi)^3} \dot{\gamma}(t') \frac{k_x^2 k_y(t,t') k_y}{kk(t,t')} \left[\frac{S'_k S'_{k(t,t')}}{S_k^2}\right] \left(f_{\boldsymbol{k}(t,t')} + h_{\boldsymbol{k}(t,t')}\mathcal{G}(t,t')\right)^2. \tag{2.148}$$

In the last step, Götze's factorization theorem has been inserted. One can identify,

$$\begin{aligned}
\sigma_{xy}(t) = &\int_0^t \mathrm{d}t' \int \frac{\mathrm{d}k^3}{2(2\pi)^3} \dot{\gamma}(t') \frac{k_x^2 k_y(t,t') k_y}{kk(t,t')} \left[\frac{S'_k S'_{k(t,t')}}{S_k^2}\right] f^2_{\boldsymbol{k}(t,t')} \\
&+ \int_0^t \mathrm{d}t' \int \frac{\mathrm{d}k^3}{2(2\pi)^3} \dot{\gamma}(t') \frac{k_x^2 k_y(t,t') k_y}{kk(t,t')} \left[\frac{S'_k S'_{k(t,t')}}{S_k^2}\right] 2 f_{\boldsymbol{k}(t,t')} h_{\boldsymbol{k}(t,t')} \mathcal{G}(t,t') \\
&+ \int_0^t \mathrm{d}t' \int \frac{\mathrm{d}k^3}{2(2\pi)^3} \dot{\gamma}(t') \frac{k_x^2 k_y(t,t') k_y}{kk(t,t')} \left[\frac{S'_k S'_{k(t,t')}}{S_k^2}\right] h^2_{\boldsymbol{k}(t,t')} \mathcal{G}^2(t,t') \qquad (2.149) \\
= &\int_0^t \mathrm{d}t' \dot{\gamma}(t') v_\sigma(t,t') \left(f^2 + 2f\lambda^2 \mathcal{G}(t,t') + \lambda^4 \mathcal{G}^2(t,t')\right). \qquad (2.150)
\end{aligned}$$

The factorization ansatz,

$$G(t,t') = v_\sigma(t,t')\phi(t,t')^2, \tag{2.151}$$

which factorizes the generalized shear modulus into a function, $v_\sigma(t,t')$, given by the vertices, $V^{(1)}_{\boldsymbol{k}(t,t'),\boldsymbol{k}(t,t')}$, and $V^{(2)}_{\boldsymbol{k},\boldsymbol{k}}$, and the transient density correlators, is only exact at the bifurcation point, $\varepsilon, \dot{\gamma} \to 0$. In quiescent MCT, the vertex function, $v_\sigma(t,t')$, is a constant, because the wave vectors are not advected, $\boldsymbol{k}(t,t') = \boldsymbol{k}$, without flow, $\gamma(t,t') = 0$. This constant stress–vertex, motivated by the results for quiescent MCT, has also been used in the schematic

model for flowing dispersions [37, 31, 38, 39, 40].

The stress vertex function, $v_\sigma(t,t')$, as defined in eq. (2.149), depends only implicitly on time via the time dependence of the accumulated strain, $\gamma(t,t')$, that enters in the strain–advected wave vectors.

When the scaling function, $\mathcal{G}(t,t')$, is small, the dominating term of the stress vertex is the first summand of eq. (2.149),

$$I_1(t,t') = \int \frac{\mathrm{d}k^3}{2(2\pi)^3} \frac{k_x^2 k_y(t,t') k_y}{k k(t,t')} \left[\frac{S_k' S_{k(t,t')}'}{S_k^2} \right] f^2_{\boldsymbol{k}(t,t')}. \tag{2.152}$$

The crucial part of its time dependence is a dephasing of the derivatives of the static structure factor, S_k' and $S_{k(t,t')}'$ [41]. The product of the derivatives can even become negative. At a certain strain, these negative contributions dominate the integral, $I_1(t,t')$, and it becomes negative.

For simple shear deformation, the integral, I_1, can be easily computed on a three–dimensional $\boldsymbol{k}$–grid in spherical coordinates, with kd running from 0.2 to 39.8 with the step size, $\Delta h = 0.4$, the inclination angle, ϑ, running from 0 to $199/200\pi$ and the azimuthal angle, φ, running from 0 to $199/100\pi$ in steps of $\pi/100$ to receive the result shown in fig. 2.6. close to the glass transition, the resulting vertex function does show a strong dependence on the density of the hard–sphere system. The numerical resolution of kd, ϑ and φ varies the resulting vertex approximately by a constant factor. Therefore, it is shown in fig. 2.6 normalized by the initial value, $I_1(0,0)$. The qualitative transient time dependence is an algebraic decay crossing zero at a fixed strain followed by a slower decay to zero. MCT is known to overestimate the strain scale of this yielding. The results, shown in fig. are rescaled by a factor, $\gamma_{\mathrm{res}} = 3.12$, to shift the point when the function, I_1, equals zero to the strain, $\gamma = 10\%$, which agrees with an empirical Lindemann criterion of shear melting [40].

To describe this time dependence of the stress–vertex function, the following ansatz was chosen [32],

$$v_\sigma(t,t') = G_0 \left(1 - \left(\frac{\gamma(t,t')}{\gamma^*} \right)^2 \right) \exp\left(- \left(\frac{\gamma(t,t')}{\gamma^{**}} \right)^2 \right). \tag{2.153}$$

Originally this ansatz was developed by fitting the resulting shear modulus of an isotropic approximation and experimental measurements, but the comparison in the inset of fig. 2.6 shows also a good agreement of the vertex function for the initial decay with the respective quantity from the microscopic theory, although the shape of the negative part cannot be sufficiently captured by the compressed exponential in eq. (2.153). The phenomenological stress–vertex function can also be found with the squares replaced by the exponents 4 [32, 42]. This choice of setting both exponents to four was made for an improved agreement with the experiments. As my major objective is to discuss results for the schematic model, I restrict the stress vertex to the form which shows best agreement with the underlying microscopically motivated theory.

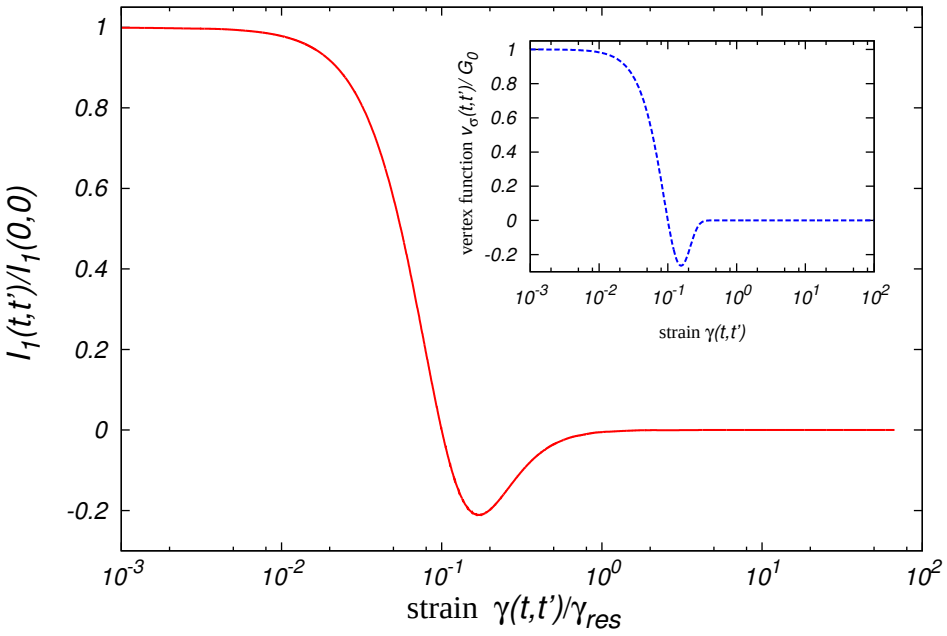

Figure 2.6.: Rescaled integral term, $I_1(t,t')/I_1(0,0)$, as function of the accumulated strain, $\gamma(t,t')$, (red). The accumulated strain has been rescaled by the strain, $\gamma_{\text{res}} = 3.12$. $I_1(t,t')$ is computed on a $\boldsymbol{k}$–grid with the wave–number times particle diameter, kd, running from 0.2 to 39.8 with step size, $\Delta h = 0.4$, the inclination angle, ϑ, running from 0 to $199/200\pi$ and the azimuthal angle, φ, running from 0 to $199/100\pi$ in steps of $\pi/100$, at a packing fraction, $\varphi = 0.52$.
The inset shows the vertex function, $v_\sigma(t,t')/G_0$, from eq. (2.153) rescaled by the instantaneous modulus, G_0, as a function of the accumulated strain, $\gamma(t,t')$ (blue, dashed).

The factorization ansatz for the generalized shear modulus in eq. (2.151) works in a direct comparison between the schematic model and MCT–ITT results [32] asymptotically close to the glass–transition point, viz. $|\varepsilon| \ll 1, \dot\gamma \ll 1$. For higher shear rates, preasymptotic corrections have to be made, and the strain scales of the vertex function, eq. (2.153), increase with the shear rate.

With a constant vertex function, $v_\sigma(t,t') = G_0$, the high shear rate viscosity $\eta^\dot\gamma_\infty$ has been determined [37],

$$\eta^\dot\gamma_\infty = \lim_{\dot\gamma\to\infty} \frac{\sigma(\dot\gamma)}{\dot\gamma} = \eta^\omega_\infty + \frac{G_0}{2\Gamma}, \tag{2.154}$$

with the high–frequency viscosity, η^ω_∞, eq. (2.144). The preasymptotic correction for the vertex strain scale, γ_*, in ref. [32] indicate, that γ_* increases faster than linear in the shear rate, $\dot\gamma$. Other parameters have been kept independent of the shear rate, so that in the limit of high shear rates, the generalized shear modulus, $G(t,t')$, decays exponentially and the decay is not dominated by the vertex function,

$$\lim_{\dot\gamma\to\infty} \gamma_* \gg \frac{\dot\gamma}{\Gamma}. \tag{2.155}$$

If this extrapolated limit holds, the asymptotic of the flow curve for high shear rates is the same as in ref. [37].

To emphasize, that eq. (2.153) is just one possible choice for a vertex function, I introduce another example,

$$v_\sigma(t,t') = G_0 \left(1 - \frac{\left(\frac{\gamma(t,t')}{\gamma^{**}}\right)^4}{1 - \left(\frac{\gamma(t,t')}{\gamma^{*}}\right)^2 + \left(\frac{\gamma(t,t')}{\gamma^{**}}\right)^4} \right), \tag{2.156}$$

which captures the shape of the stress overshoot, or the dip in the modulus better, at cost of the agreement for smaller times.

The influence of the dephasing of the structure–factor derivatives, the time–dependence of the stress vertices is shown in the following chapter.

3. Reversal of the shear flow

In this chapter, I will discuss the results of the schematic MCT model for a simple time–dependent shear protocol.

In the subsequent section, I will introduce the reversal of shear flow and the numerical methods I used to study the problem. The following sections present the results in dependence on what would be the control parameters in an experimental setup, the strain of the preshear before the reversal, γ_+, the separation parameter, ε, that corresponds to a relative packing fraction and the shear rate, $\dot{\gamma}$.

3.1. Shear reversal

One way to probe a materials viscoelasticity and to study the importance of the stress–vertex function, $v_\sigma(t,t')$, is to apply a simple shear protocol of a non constant shear rate $\dot{\gamma}(t) \neq \text{const}$. In such a protocol, the accumulated strain is not time–translational invariant anymore, which gives insight how the response is affected by the symmetry of the equations of the model under time translations.

One example of this is the shear reversal, the shear rate is kept constant up to some time–point; then its sign is reversed,

$$\dot{\gamma}(t) = \begin{cases} 0 & \text{for } t < 0, \\ +\dot{\gamma} & \text{for } 0 < t < t_w, \\ -\dot{\gamma} & \text{for } t > t_w. \end{cases} \tag{3.1}$$

This shear protocol leads to the following time dependence of the accumulated strain,

$$\gamma(t,t') = \begin{cases} \dot{\gamma}\,(t-t') & \text{for } 0 < t' < t < t_w, \\ \dot{\gamma}\,(2t_w - (t+t')) & \text{for } 0 < t' < t_w < t, \\ -\dot{\gamma}\,(t-t') & \text{for } t_w < t'. \end{cases} \tag{3.2}$$

Dense amorphous materials close to the glass transition show under this protocol a response rich in phenomenons.

For start–up steady shear, these materials exhibit an increase of the shear stress, followed by a stress overshoot, before finally reaching a steady state of constant stress. After a reversal

of the shear flow, the stress might have a stress overshoot with the opposite sign, or rather a stress undershoot, but it will decrease in its magnitude after a shear reversal. The slope of the stress response as a function of the strain, the stress–strain curve, will also decrease, which corresponds to a softening of the material. These changes in the transient material properties depending on their history have been studied in the past by Johann Bauschinger [43]. The dependence of a materials yielding under applied stress on the direction of a previous load, viz. compressional or tensile load, is therefore denoted as the Bauschinger effect. As the mechanism that affects the yielding after shear reversal is related to the Bauschinger effect, in ref. [33] the reversal of shear–flow is studied under the scope that the phenomena of history–dependent response can be generalized. The memory effects are studied in a molecular dynamics simulation and the schematic model to rationalize the Bauschinger effect. The schematic model of MCT provides new insights in explaining the Bauschinger effect as a history–dependent transient response phenomenon and is confirmed by a molecular–dynamics (MD) simulation, which connects the macroscopic stress response to microscopic particle motion.

Bauschinger effects are observed as well for amorphous solids in stress-controlled protocols [44] and in the flow–controlled equivalent [45].

The stress response of a viscoelastic material differs significantly from the stress response of a linear elastic solid or a Newtonian fluid. For a linear elastic solid, the relation between stress and strain is linear [46]. In the case of simple shear, the relation between shear stress and shear strain reads,

$$\sigma = G\gamma, \tag{3.3}$$

with shear stress, σ, shear strain, γ and the elastic shear modulus or Young modulus, G. On reversal of the direction of strain, the stress would decrease linearly along the same line it was increased before. The deformation of an linear elastic solid is reversible.

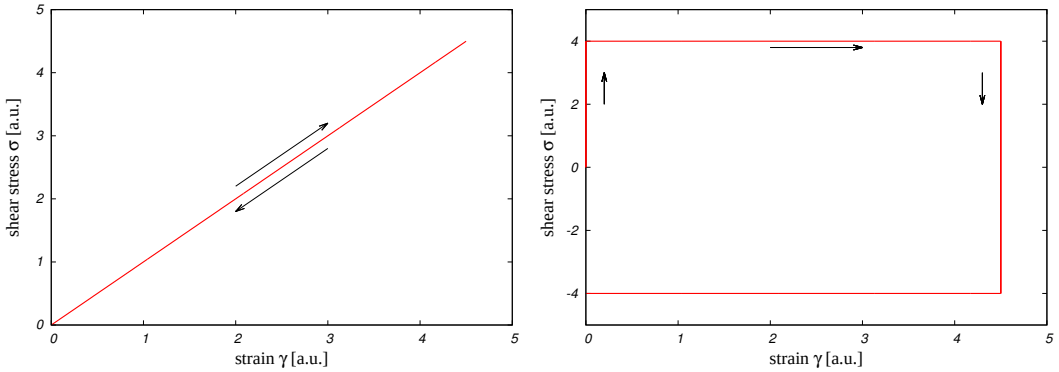

Figure 3.1.: Left panel: Stress–strain curve of a shear–flow reversal for a linear elastic solid. Right panel: Shear reversal for a Newtonian fluid.

3. Reversal of the shear flow

A Newtonian liquid on the other hand relates the shear stress, σ, and shear rate, $\dot{\gamma}$, linearly,

$$\sigma = \eta\dot{\gamma}, \tag{3.4}$$

with the Newtonian shear viscosity, η. If one imposes simple shear with a steady shear rate upon a Newtonian liquid, the shear stress jumps immediately to the value in accordance with eq. (3.4), when the direction of shear is reversed, the stress will jump immediately to the negative value. All of the work imposed on the Newtonian liquid to shear it, has been dissipated and it will not be restored on reversal unlike the work imposed on a linear elastic solid.

3.1.1. Solving shear reversal with the schematic model

To compute the shear stress, the schematic MCT model of sec. 2.4 is adapted. The shear protocol of the reversal enters via the shear rate in the constitutive equation,

$$\sigma = \int_{-\infty}^{t} \mathrm{d}t' \gamma(t') G(t, t', [\dot{\gamma}]), \tag{3.5}$$

the strain dependence of the stress–vertex function,

$$v_\sigma(t, t') = G_0 \left(1 - \left(\frac{\gamma(t, t')}{\gamma^*}\right)^2\right) \exp\left(-\left(\frac{\gamma(t, t')}{\gamma^{**}}\right)^2\right), \tag{3.6}$$

and the strain–dependence of the so called h–functions in the memory kernel,

$$h(t, t') = \frac{1}{1 + \left(\gamma(t, t')/\gamma_c\right)^2}. \tag{3.7}$$

As the memory kernel is not time–translational invariant for the reversal of shear, eq. (2.110) has to be solved with explicit dependence on the time parameters, t and t', for $0 < t' < t_w < t$. The time dependence simplifies to a time–translational invariant dependence on the time difference, $t - t'$, for $0 < t' < t < t_w$ and $t_w < t'$. For reasons of numerical efficiency, this motivates that I solve only the not time–translational invariant regime with two time–parameters. I simplify the numerical equations for the latter two time regimes, so they depend only on a single time parameter, $t - t'$.

The equations are discretized as described in sec. A.1. The time–step duration is doubled every N steps. N is a number between 2000 and 4000 and chosen with the constraint, that the prestrain is reached exactly at a time step, before the duration is doubled again.

3.1.2. Broken time–translational symmetry

The continuous time translational symmetry of eq. (2.87) is broken for any non–steady flow. The equation,

$$\phi(t, t') = \phi(t - t', 0), \tag{3.8}$$

does not hold for a shear rate which varies in time.

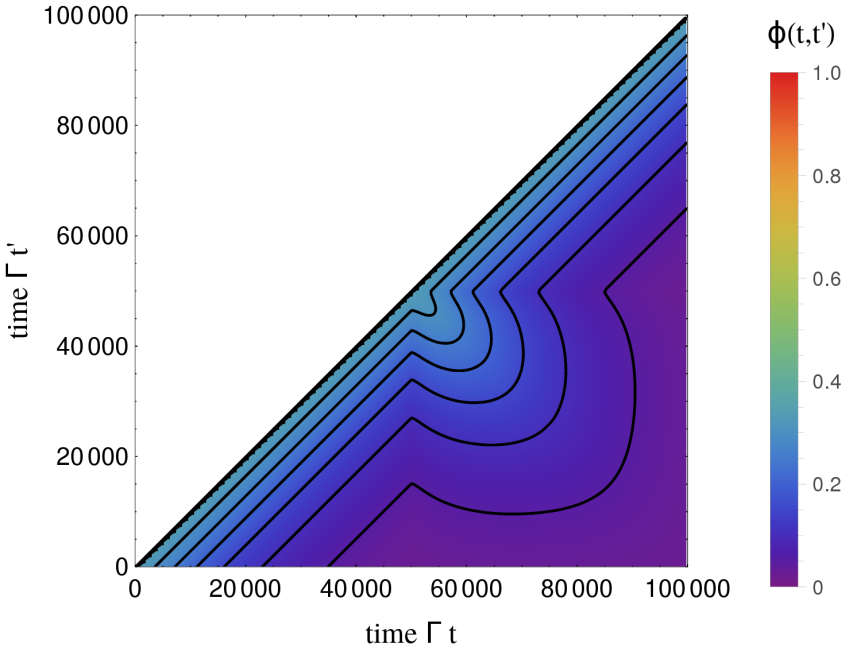

Figure 3.2.: Transient density correlator, $\phi(t, t')$, as a function of the two time parameters, t and t', rescaled by the initial decay rate, Γ. Contour lines mark values in steps of 0.05 of the density correlator.

Fig. 3.2 shows the solutions for the density correlator which was obtained by the methods described in the previous section. The time of reversal is in the middle of the t– and the t'–axis, respectively. The region for $t' > t$ is non–causal. The remaining half of the time plane is separated by the reversal into three parts. The two triangular sections in the lower left and upper right corner correspond to those times when the accumulated strain is given by, $\gamma(t, t') = +\dot{\gamma}(t - t')$, and ,$\gamma(t, t') = -\dot{\gamma}(t - t')$ respectively.

Therefore, the equation of motion is invariant under time translations within each of these time domains. The solutions for the density correlator in these two time domains have been computed by equations with a single time parameter. The square in the lower right corner of the time plane is the time domain, in which the accumulated strain is given by eq. (3.2), and thus the time–translational symmetry is broken. The density correlator does not depend

on the time difference, $t - t'$, but is a function explicitly of both time parameters. Physically the resulting correlator shows, that the structural relaxation is slowed down by the reversal if it is compared to the shear induced relaxation for steady shear.

This result shows the the density correlator is not a function of the strain, displayed in fig. 3.3. The density correlator, $\phi(t, t')$, decreases fast, when the absolute value of the accumulated strain, $|\gamma(t, t')|$, is large, which corresponds to the red and purple areas in fig. 3.3. But the density correlator, $\phi(t, t')$, decreases as well, when the difference of the time parameters, $t - t'$, is increased. This is easily seen along the line of, $t + t' = 2t_w$, the red dashed diagonal in fig. 3.3. Along this diagonal, the accumulated strain remains zero. But the density correlator decays, albeit very slowly.

In ref. [33], Th. Voigtmann introduced a generalized Maxwell model to explain the history dependence of the stress response. The constitutive of the generalized Maxwell model is of the same form as eq. (3.5). Simplifying the complex two–time dependence of the transient density correlator, the model captures shear–thinning , $e^{-(t-t')\cdot|\dot{\gamma}(t')|/\tilde{\gamma}_c}$. The generalized shear modulus reads,

$$G_M(t, t') = v_\sigma(t, t')e^{-(t-t')\cdot|\dot{\gamma}(t')|/\tilde{\gamma}_c}. \tag{3.9}$$

Comparing the results of the generalized Maxwell model with the results of the schematic MCT model enables an estimation, how the history–dependent stress response is affected by the complex time dependence of the transient density correlator shown in fig. 3.2.

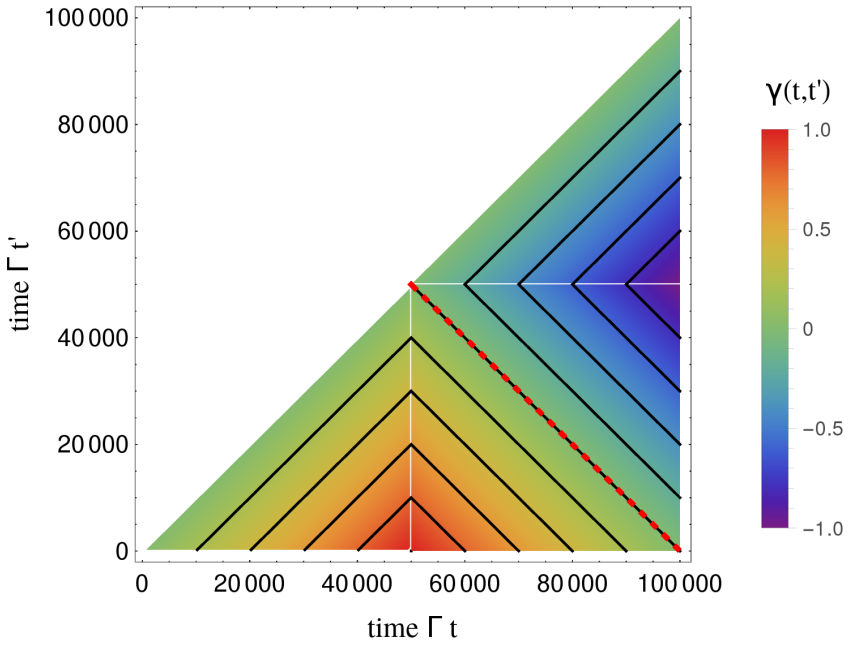

Figure 3.3.: Accumulated strain, $\gamma(t, t')$, as a function of the two time parameters, t and t', rescaled by the initial decay rate, Γ. Contour lines mark values in steps of 0.2 of the strain, $\gamma(t, t')$. The dashed red line marks the line of zero strain, $\gamma(t, t') = 0$.

3.2. Preshear–strain dependence

A hysteresis for a strain recovery is associated with yielding [47]. In ref. [33], we discussed two regimes of elasticity–dominated and plasticity–dominated prestrain.

3.2.1. Hysteresis in the stress–strain curve

Pe_0	ε	G_0	Γ	γ_c	γ^*	γ^{**}
10^{-5}	10^{-3}	100	100	0.35	0.1	0.12

Table 3.1.: $F_{12}^{(\dot{\gamma})}$–parameters used in the MCT computations for this section.

As it is shown in fig. 3.4, the stress response in the elasticity–dominated regime is not linearly elastic, but might rather be called anelastic. The deviation from a linear stress–strain relation is mostly caused by the structural relaxation in the short–time diffusion and the fast β–process. The enclosed area of the stress–strain curve corresponds to the energy that was dissipated by those two processes during the steady shear.

At larger prestrain, a crossover to the plasticity–dominated regime occurs. The strain, needed to reverse the stress completely, does not increase further. In this regime, the strain–

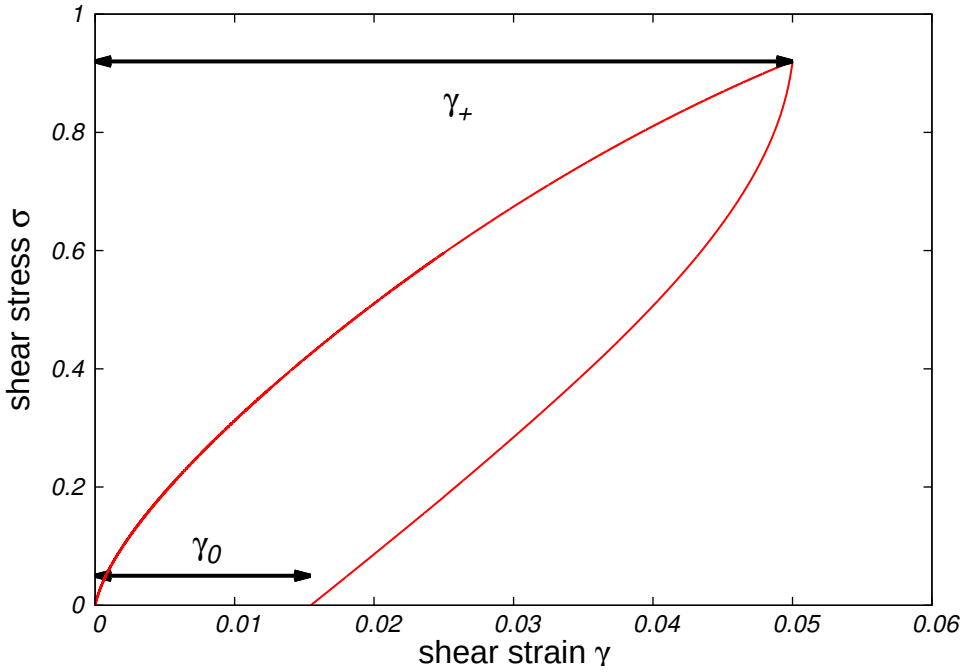

Figure 3.4.: Stress vs. strain curve for a shear reversal at preshear strain, $\gamma_+ = 0.05$, with parameters as stated in tab. 3.1.

induced relaxation is the dominant mechanism and the contribution of the β–relaxation becomes less important.

The viscoelasticity or anelasticity is quantified by the residual strain, γ_0, that the system still experiences after the shear stress has been decreased to zero. The prestrain, γ_+, which marks the onset of a residual strain, is interpreted to be the true yield strain in strain–recovery experiments on amorphous polymers [48]. The shear protocol in these experiments differs from the shear–reversal protocol, eq. (3.1), as in the experiment a larger shear rate has been imposed than for the preshear. Fig.3.6 shows that the prestrain dependence of this quantity can be divided into two regimes. For small prestrains, $\gamma_+ \lessapprox 0.1$, the residual strain, γ_0, grows linearly with the preshear strain, γ_+, but its slope is significantly smaller than one. At larger prestrains, $\gamma_+ \gtrapprox 0.3$, the residual strain is given by the prestrain minus a constant, $\gamma_0 \approx \gamma+ - 0.11$, which accounts for the initial anelasticity.

The viscoelasticity can be visualized by comparing the prestrain, γ_+, in one direction and the respective strain in the reversed direction, $|\gamma_0 - \gamma_+|$, applied to unload the shear stress again to its original amplitude of zero shear stress. Fig. 3.6 displays how the required strain to unload the shear stress depends on the previously applied prestrain. As it is shown in the figure, a linear elastic solid requires the same strain on reversal as was applied previously, to unload. In a Newtonian fluid, the unloading is instantaneously and the strain needed for unloading the stress is constantly zero. For the viscoelastic glass and dense fluids, the

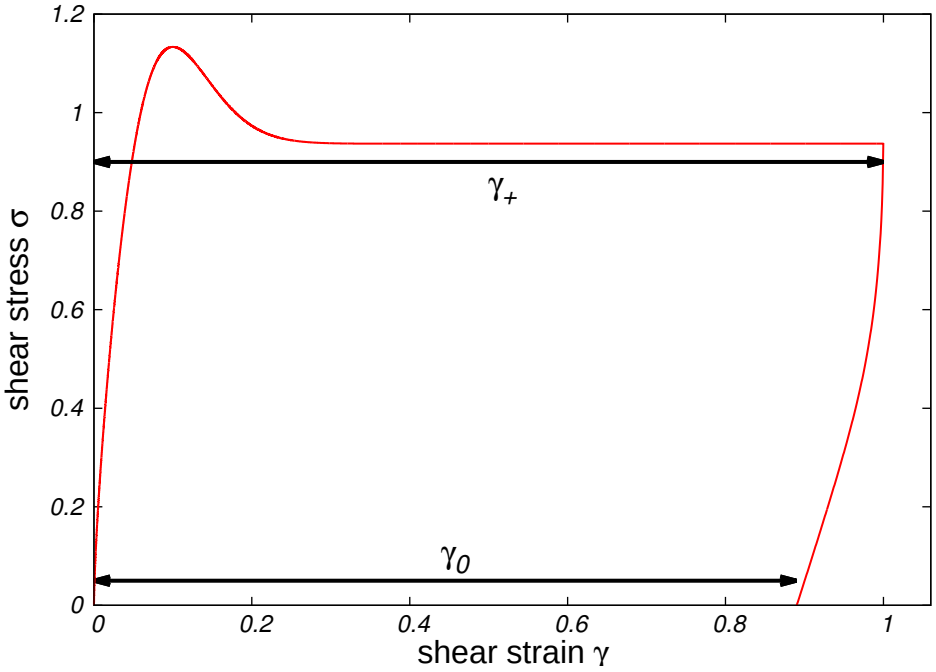

Figure 3.5.: Stress vs. strain curve for a shear reversal at preshear strain, $\gamma_+ = 1.00$, with parameters as stated in tab. 3.1.

required strain for the unloading follows qualitatively the shape of the stress–strain curve of startup–flow.

In the anelastic regime, the unload strain, $|\gamma_+ - \gamma_0|$, grows linearly with the prestrain, albeit with a factor of proportionality smaller than one. This shallow ramp is a result of the dissipation in the fast β–process, eq. (2.121), and for very small prestrains it is due to the diffusive short–time dynamics, eq. (2.112).

The unload strain, $|\gamma_+ - \gamma_0|$, peaks at a strain larger than γ^*, the strain of maximal stress. For larger prestrains, the strain required to unload the stress stays constant as for the Newtonian fluid. This is expected for preshear strains, which mark the onset of a non–equilibrium steady state. In contrast to the Newtonian fluid, the initial (an)elastic response shifts the unload strain to a nonzero value. The residual strain, γ_0, is determined numerically by a linear interpolation between two data points, the numerical error can be estimated through the fluctuations which the unload strain, $|\gamma_+ - \gamma_0|$, shows for large prestrains, γ_+.

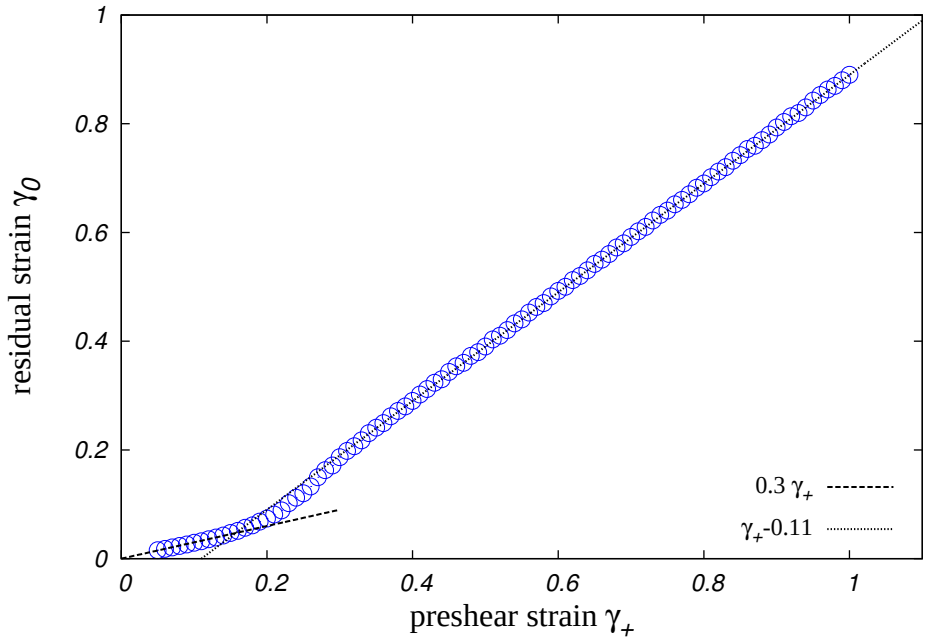

Figure 3.6.: Residual strain, γ_0, at the point of zero shear stress, $\sigma = 0$, after a shear reversal. Blue circles show the results for the schematic model computed with the parameters given in tab. 3.1. The dashed line highlights the initial increase of the residual strain, γ_0, with approximately $0.3 \times \gamma_+$, the dotted line shows the asymptotic linear dependence on the preshear strain, γ_+, with an offset of approximately 0.11.

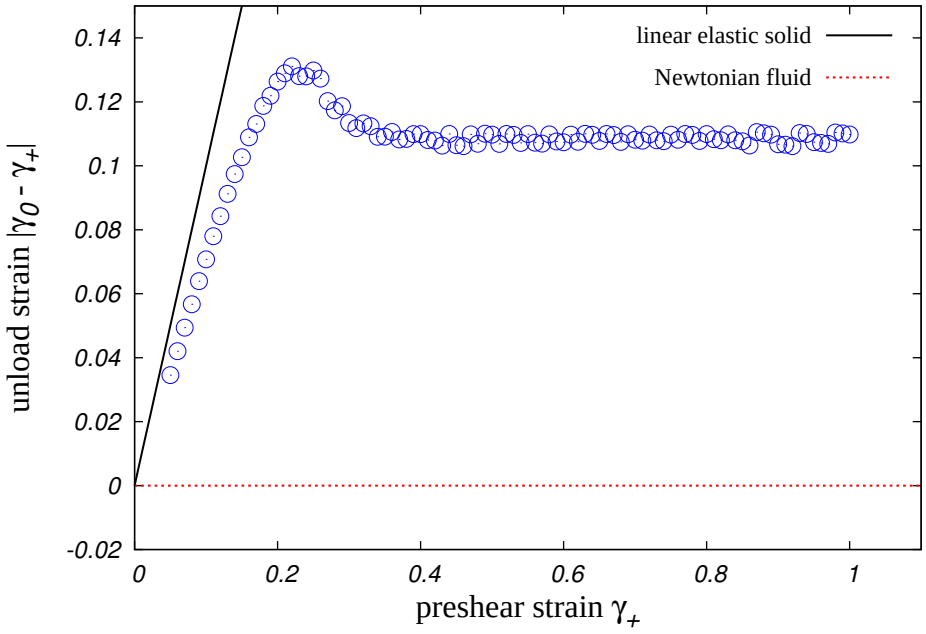

Figure 3.7.: Unload strain, $|\gamma_0 - \gamma_+|$, vs. preshear strain, γ_+. Blue circles show the results for the schematic model for parameters as in tab. 3.1. For comparison, the full black line shows the result for a linear elastic solid and the dotted red line the respective result for a Newtonian fluid.

3.2.2. Decreasing stress overshoots

The most notable effect after the reversal of the shear flow are the decreasing stress overshoots. This phenomenon becomes more prominent with increasing prestrain, γ_+. Fig. 3.8 shows the decreased overshoot, quantified by its stress value, σ_{peak}. It is smaller than the peak of the start–up shear stress. In order to separate the discussion from the effects of a flow curve, discussed for schematic models in refs. [31, 32], I focus on the relative height of the stress overshoot compared to the steady–state stress, σ_{steady}. After a reversal of the shear flow, the long–time limit of the shear stress, σ_{steady}, changes its sign but not its magnitude.

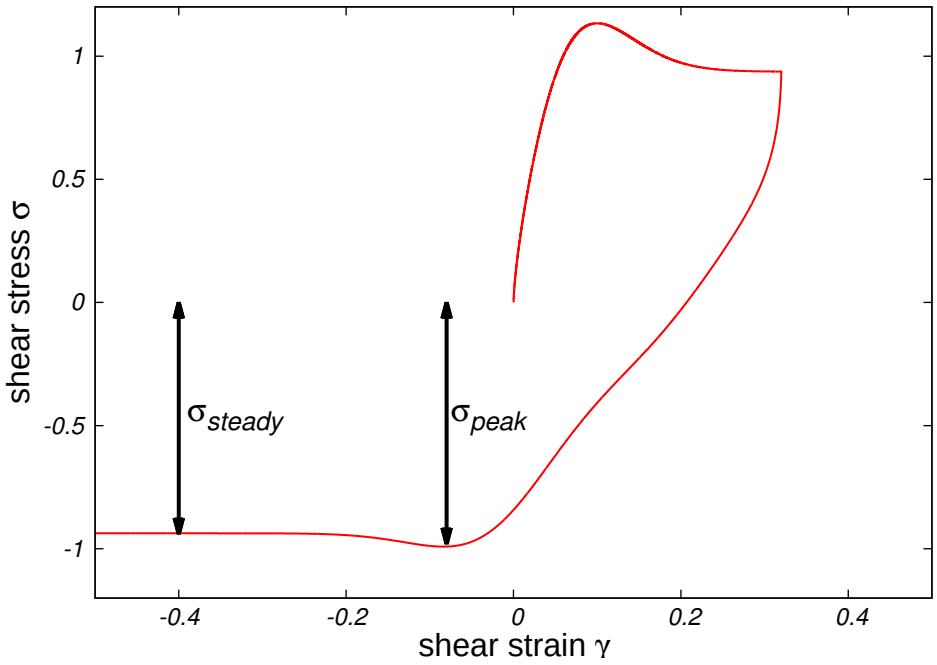

Figure 3.8.: Stress vs. strain curve for a shear reversal at prestrain, $\gamma_+ = 0.32$, with the separation parameter, $\varepsilon = 10^{-3}$, and the shear rate, $Pe_0 = 10^{-3}$, and the other parameters as in tab. 3.1.

A direct comparison of the stress–strain curves for start–up flow and the resulting stress–strain curve after a reversal of the flow from fig. 3.8 in absolute values of the stress and strain is given by fig. 3.9. After the reversal, the stress overshoot has noticeable decreased compared to overshoot of the start–up curve.

In the anelastic regime, i.e. for small preshear strains, γ_+, the height of the stress overshoot after the reversal of the shear flow is almost unchanged compared to the overshoot of a start–up curve. Fig. 3.8 shows that the height of the stress overshoot after the reversal, σ_{peak}, is significantly smaller, when the prestrain, γ_+, approaches the strain ,γ^*, which marks the strain value at which the stress overshoot occurs. The overshoot height after the reversal as

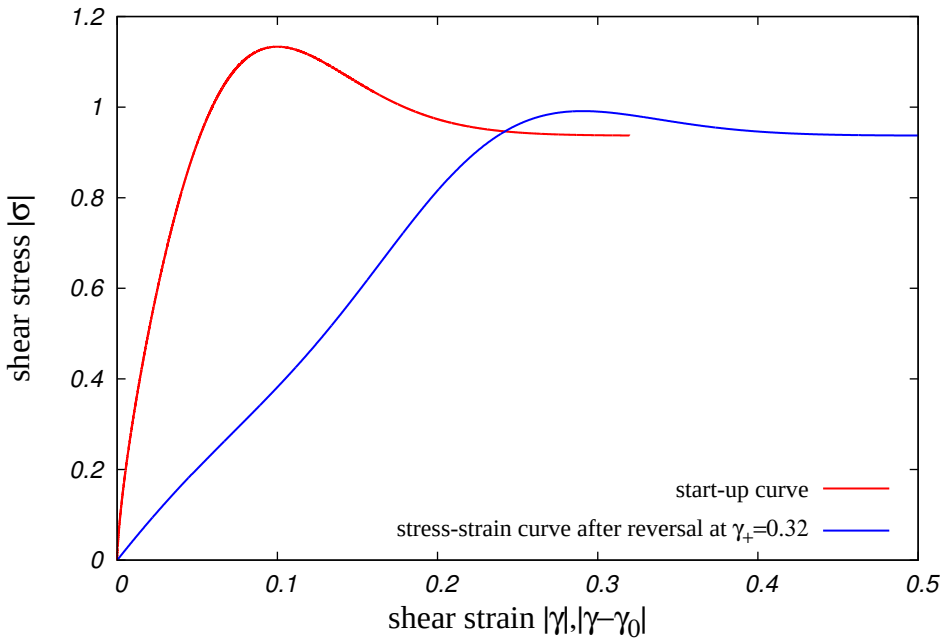

Figure 3.9.: Absolute shear stress, $|\sigma|$, vs. shear strain, $|\gamma|$, and shifted shear strain, $|\gamma - \gamma_0|$, for start–up flow (red) and after a reversal of the flow at a prestrain, $\gamma_+ = 0.32$, (blue), respectively. All parameters as in fig. 3.8

a function of the prestrain starts to decrease fast, until it almost vanishes for a reversal in the steady–state. The relative overshoot height, $\frac{\sigma_{peak}}{\sigma_{steady}} - 1$, as a function of the prestrain, γ_+, decays like a compressed exponential. The shape of the result in fig. 3.10 depends in the $F_{12}^{\dot{\gamma}}$–model strongly on the form of the stress–vertex function, $v_\sigma(t, t')$. As the stress–vertex function, $v_\sigma(t, t')$, given in eq. (2.153), does not fully capture the shape of the stress overshoot, the results cannot be overgeneralized. With the methods of studying the vanishing overshoot after a shear reversal with the schematic model, it is not likely to find a universality that quantitatively holds also for the microscopic MCT–ITT approach, experimental observations and the results of simulations on particle level.

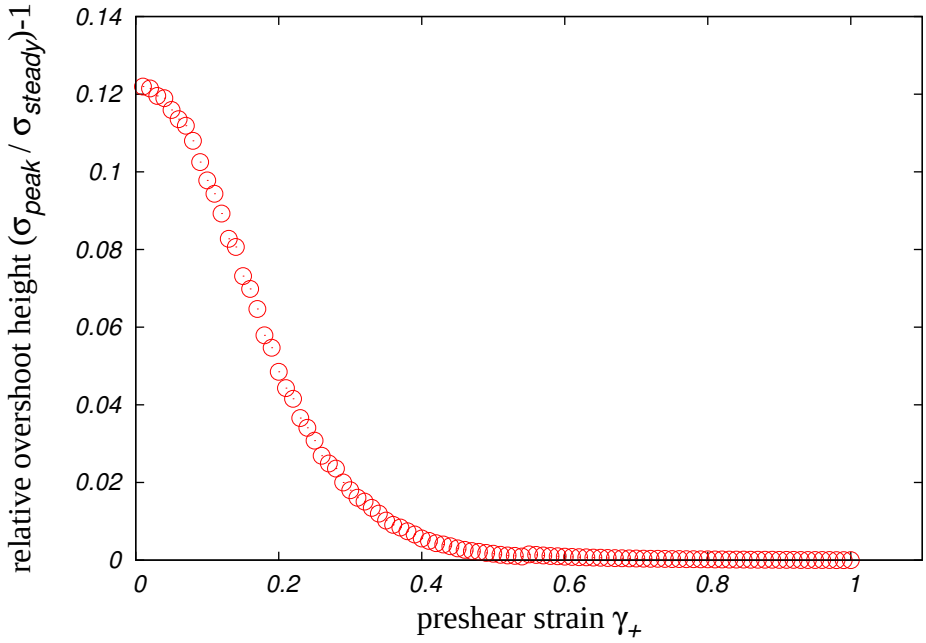

Figure 3.10.: Relative height of the stress overshoot, $\frac{\sigma_{peak}}{\sigma_{steady}} - 1$, after a reversal of shear flow at prestrain, γ_+, with the separation parameter, $\varepsilon = 0$, the shear rate, $Pe_0 = 10^{-5}$, and the other parameters s in tab. 3.1.

3.2.3. Softening

The third phenomenon observable after a shear reversal is the apparently softer stress response, i.e., the slope of the stress–strain curve after reversal is lower compared to the slope of a start–up curve, fig. 3.11. As the slope for the stress–strain curve is given by the linear shear modulus G_∞, I will name the slope after a shear reversal the effective modulus G_{eff}.

The effective modulus is computed as the difference quotient of the slope of the stress–strain curve at the strain, $|\gamma - \gamma_0| = 0.028$. After a shear reversal, the slope of the stress–strain curve, G_{eff}, seems smaller than the slope, G_∞, of the start–up stress–strain curve. This can be seen in the direct comparison of both stress–strain curves in fig. 3.12.

Fig. 3.13 shows, how the apparent elasticity in form of the effective shear modulus, G_{eff}, depends on the preshear strain, γ_+. By construction, the effective modulus is equal to the plateau modulus of the glass for vanishing preshear. The strain, $|\gamma - \gamma_0| = 0.028$, at which the difference quotient is evaluated, has been chosen as a strain, at which the shear modulus for start–up strain reaches the plateau shear modulus, G_∞. For larger preshear strains, $\gamma_+ > 0$, the effective shear modulus after the reversal of the shear flow is smaller. It exhibits its minimal value at a preshear strain, which coincides with the preshear strain, at which the unload strain, $|\gamma_0 - \gamma_+|$, has its maximum. For larger preshear strains, the effective

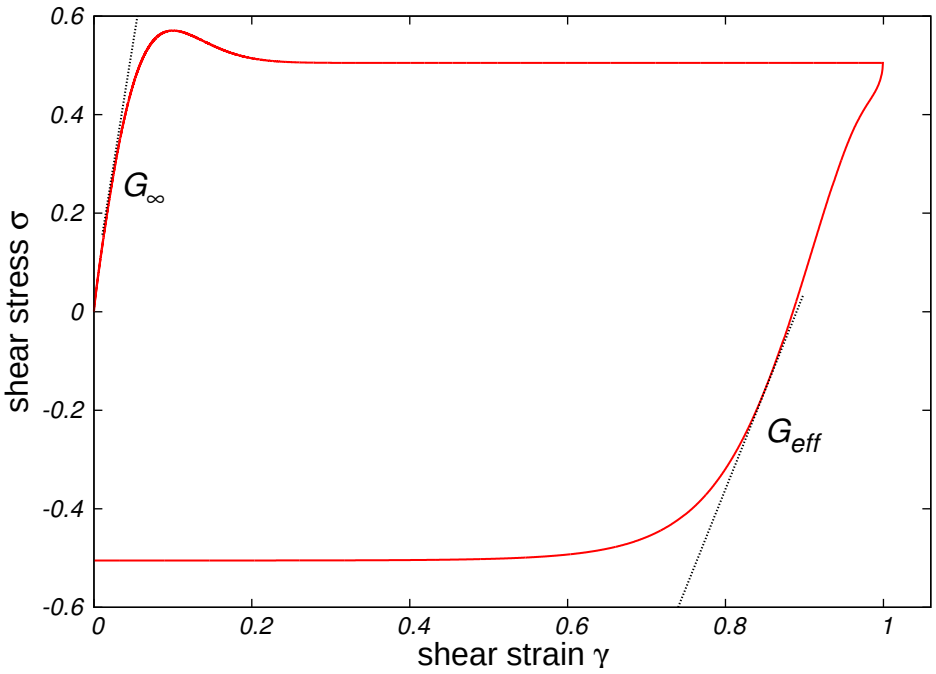

Figure 3.11.: Stress vs. strain curve for a shear reversal at the preshear strain, $\gamma_+ = 1$, with the separation parameter, $\varepsilon = 0$, the bare Peclét number, $Pe_0 = 10^{-5}$, and the other parameters as int tab. 3.1. The decreased apparent shear modulus, G_{eff}, after the reversal and the linear shear modulus, G_∞, of the start–up curve are indicated by the respective dotted black lines.

shear modulus remains constant. This hints, that the preshear has indeed approached a non–equilibrium steady state for the preshear.

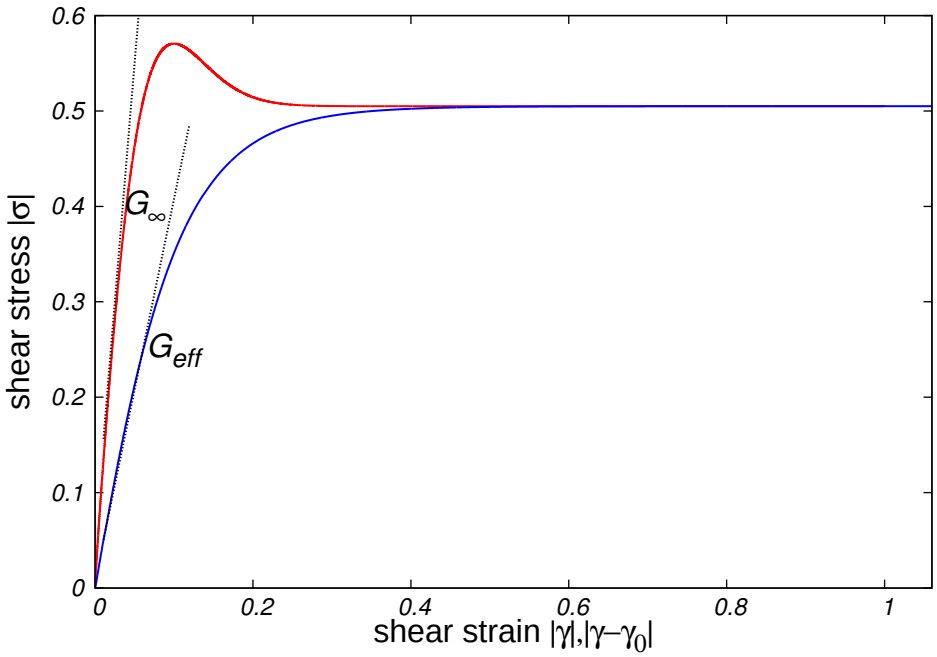

Figure 3.12.: Absolute stress, $|\sigma|$, vs. strain, γ, and shifted strain, $|\gamma - \gamma_0|$, for start–up flow (red) and the resulting stress–strain curve after a reversal of the flow a a prestrain of $\gamma_+ = 0.32$ (blue), respectively, from fig.3.8. The decreased apparent shear modulus, G_{eff}, after the reversal and the linear shear modulus, G_∞, of the start–up curve are indicated by the respective dotted black lines.

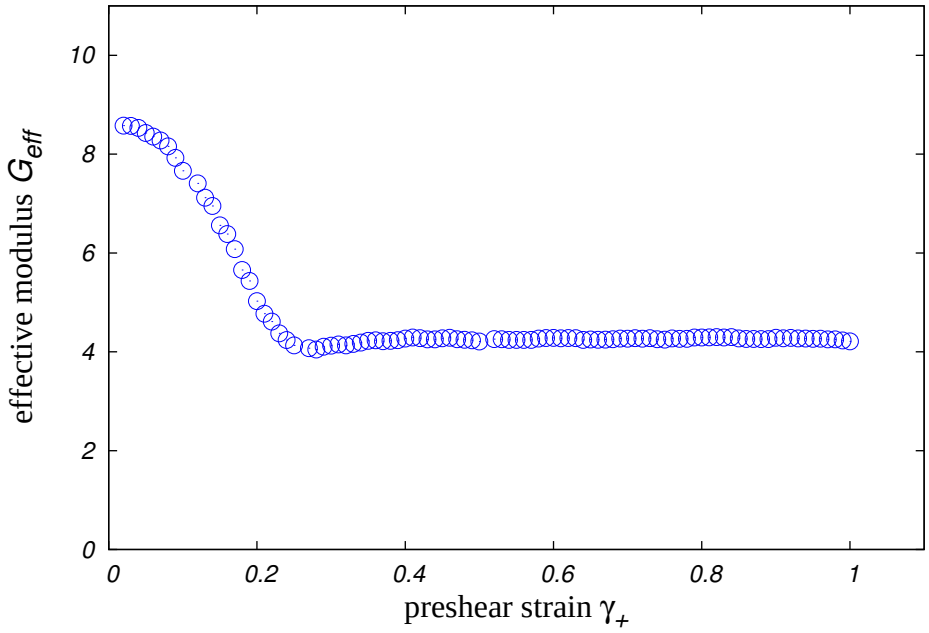

Figure 3.13.: Effective shear modulus, G_{eff}, as function of the preshear strain, γ_+, for the separation parameter, $\varepsilon = 0$, the bare Peclét number, $Pe_0 = 10^{-5}$, and the other parameters as in tab. 3.1.

3.3. Density dependence

3.3.1. Unload strain $|\gamma_0 - \gamma_+|$

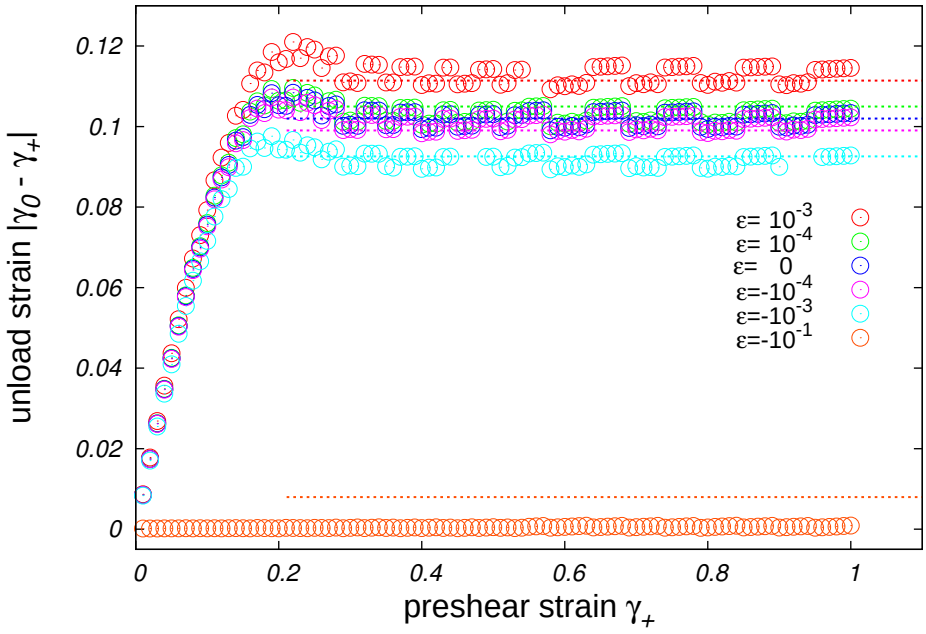

Figure 3.14.: Unload strain, $|\gamma_0 - \gamma_+|$, vs. preshear strain, γ_+, for six separation parameters, $\varepsilon = -10^{-1}, -10^{-3}, -10^{-4}, 0, 10^{-4}, 10^{-3}$, increasing from the bottom to the top the bare Peclét number, $Pe_0 = 10^{-5}$, and the other parameters as in tab. 3.1. Dashed lines highlight that the result for large preshear strain, γ_+, is shifted proportional to the square root of the separation parameter, $+\sqrt{\varepsilon}$, for the glassy curves and, $-\sqrt{\varepsilon}$, for the fluid curves.

The variation of the strain, $|\gamma_0 - \gamma_+|$, required to unload the shear–stress response to a previously applied preshear strain, γ_+, is shown in fig. 3.14. The initial anelastic regime and the following regime of plastic flow seem separated by a maximum of the unload strain as a function of the prestrain. This separation is observed for each separation parameter except the one corresponding to the lowest packing fraction, viz. $\varepsilon = -10^{-1}$. As the α–relaxation time, τ_α, diverges at the glass transition, eq. 2.130, there exists a density for each shear rate, $\dot{\gamma}$, so that the dressed Péclet or Weissenberg number is smaller than one, $Pe = \dot{\gamma}\tau_\alpha < 1$. For these low densities and shear rates, I do not probe the nonlinear response of the material anymore. The shear modulus decays so fast, that it remains almost unaffected by the imposed shear flow. For the lowest separation parameter, $\varepsilon = -10^{-1}$, the result of the unload strain is so close to the expected result of the unload strain for a Newtonian fluid, as shown in fig. 3.7, that an initial anelastic regime cannot be identified. In fact, the

unload strain for the smallest separation parameter, $\varepsilon = -10^{-1}$, is so small, that it is of the same size as the numerical error of the linear interpolation, used to determine the residual strain, γ_0. Closer to the glass transition, the unload strain, $|\gamma_+ - \gamma_0|$, remains constant after a shear–flow reversal approximately at a preshear strain, $\gamma_+ \gtrsim 0.3$. This unload strain after large preshear strains scales with the density. The deviation from the result at the glass transition, $\varepsilon = 0$, is proportional to the square root of the separation parameter, $\sqrt{|\varepsilon|}$, for small separation parameters, $|\varepsilon| \ll 1$,

$$\lim_{\gamma_+ \to \infty} |\gamma_+ - \gamma_0(\varepsilon)| = |\gamma_+ - \gamma_0(\varepsilon = 0)| \pm c_{\gamma_0} \sqrt{|\varepsilon|}, \tag{3.10}$$

with a constant, c_{γ_0}.

3.3.2. Decreasing stress overshoot

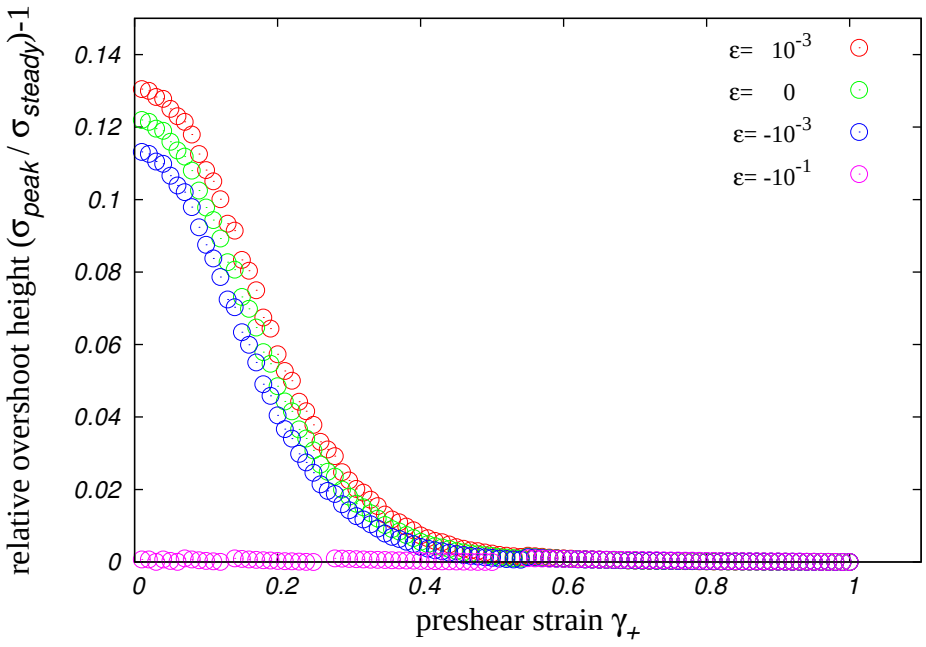

Figure 3.15.: Relative height of the stress overshoot, $\frac{\sigma_{peak}}{\sigma_{steady}} - 1$, after a shear reversal at the preshear strain, γ_+, for the separation parameters, $\varepsilon = 10^{-1}, 10^{-3}, 0, 10^{3},$, the bare Peclét number, $Pe_0 = 10^{-5}$, and the other parameters as in tab. 3.1.

If I keep the parameters of the stress vertex function, $v_\sigma(t, t')$, constant and vary only the separation parameter, ε, i.e., if I neglect preasymptotic corrections of the stress–vertex function, the relative overshoot height of the start–up strain curves increases with the separation parameter, ε. As the overshoot height of the start–up curves changes with the density, so

does the overshoot height after a shear reversal at a small preshear strain.

Far from the glass transition, $\varepsilon = 10^{-1}$, the fluid does not exhibit a stress overshoot and its stress response can be described by linear response theory. Trivially, the yielding does not change after a reversal of shear flow.

3.3.3. Softening

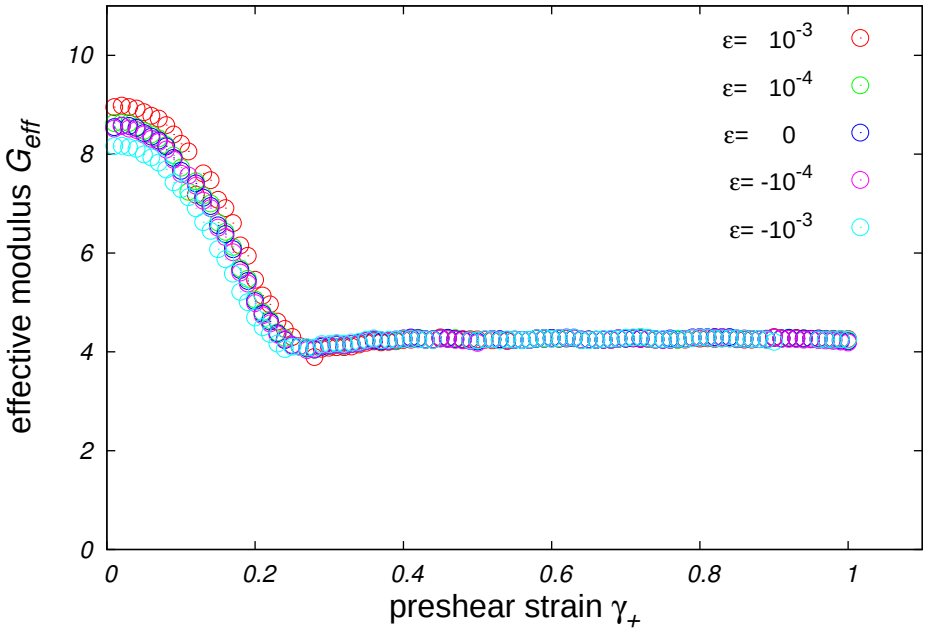

Figure 3.16.: Effective shear modulus, G_{eff}, as a function of the prestrain, γ_+, for the separation parameters, $\varepsilon = -10^{-3}, -10^{-4}, 0, 10^{-4}, 10^{-3}$, the bare Peclét number, $Pe_0 = 10^{-5}$, and the other parameters as in tab. 3.1.

The value of the effective shear modulus, G_{eff}, after a reversal of the shear flow, varies for small preshear strains, γ_+, with the square root of the separation parameter, $\sqrt{\varepsilon}$. This scaling is expected, as the plateau shear modulus depends on the nonergodicity parameter, f_ε, eq. (2.127). Fig. 3.16 shows the effective modulus for the shear rate, $Pe_0 = 10^{-5}$, and for various separation parameters. The effective modulus has been computed as the slope of the stress–strain curve at a fixed strain, $|\gamma_0 - \gamma| = 0.028$, because the slope of the start–up curve has approached the plateau modulus, G_∞, at this value for the strain, γ. The effective modulus as a function of the preshear strain, γ_+, decreases onto the value observed after a flow reversal in the steady state. The effective modulus after shear–flow reversal in the steady state is about half the size of the critical plateau modulus, G_∞^c, and it does not visibly depend on the separation parameter, ε. Results for the lowest separation parameter,

$\varepsilon = 10^{-1}$, cannot be given, as the α–relaxation time, τ_α, is smaller than the time it takes to strain a material up to the chosen strain scale, $|\gamma_0 - \gamma(t)| = 0.028$, at this shear rate, $Pe_0 = 10^{-5}$.

3.4. Shear–rate dependence

3.4.1. Unload strain $|\gamma_0 - \gamma_+|$

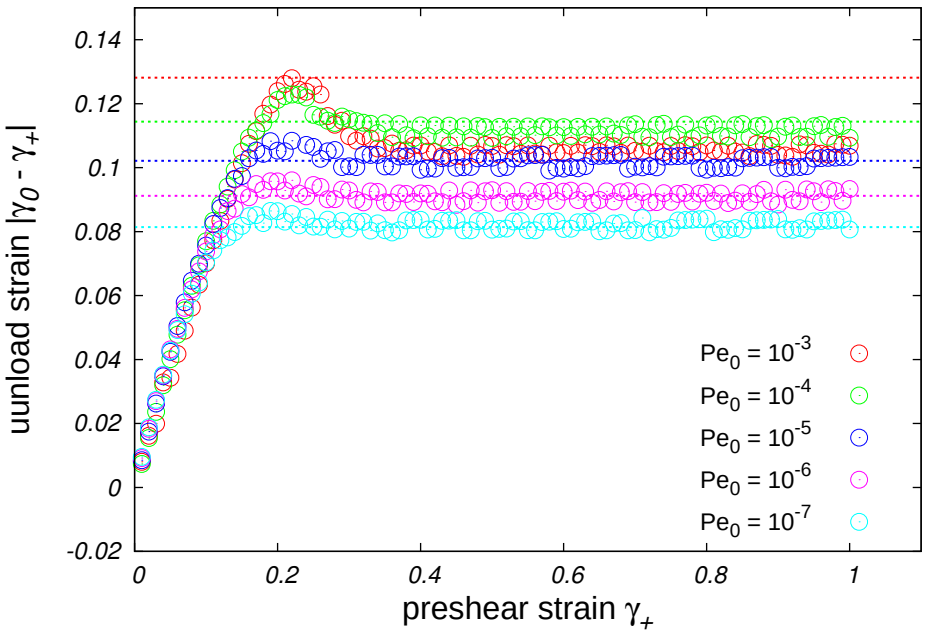

Figure 3.17.: Unload strain, $|\gamma_0 - \gamma_+|$, vs. preshear strain, γ_+, for a separation parameter, $\varepsilon = 0$, various shear rates, $Pe_0 = 10^{-7}, 10^{-6}, 10^{-5}, 10^{-4}, 10^{-3}$, and the other parameters as in tab. 3.1.

The strain, $|\gamma_0 - \gamma_+|$, required to unload the shear–stress response to a previously applied preshear strain does not show a significant shear–rate dependent scaling in the anelastic regime within the range of the accuracy of the results, fig. 3.17. In the regime of plastic flow, i.e., for larger preshear, the unload strain does scale with the shear rate. For the four lowest shear rates, i.e., close to the glass transition point, the unload strain is proportional to the logarithm of the shear rate, $|\gamma_0 - \gamma_+| \propto \log(\dot{\gamma})$. For the highest shear rate, $Pe_0 = 10^{-3}$, this scaling is does not hold. The yielding occurs before the shear modulus approaches the value of the plateau modulus, G_∞.

3.4.2. Decreasing stress overshoot

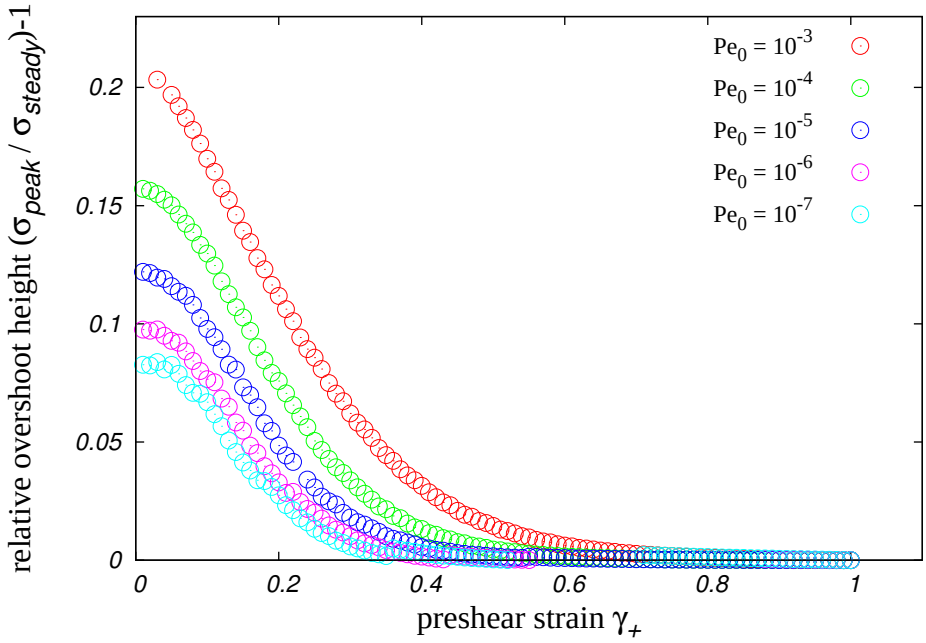

Figure 3.18.: Relative overshoot , $\frac{\sigma_{peak}}{\sigma_{steady}} - 1$, vs. preshear strain, γ_+, for a separation parameter, $\varepsilon = 0$, various shear rates, $Pe_0 = 10^{-7}, 10^{-6}, 10^{-5}, 10^{-4}, 10^{-3}$, and the other parameters as in tab. 3.1.

The relative height of the stress overshoots decreases as a compressed exponential of the preshear strain. The shear–rate dependence of the overshoot height is discussed for steady shear in ref. [32]. For vanishing preshear, the overshoot height shows the same dependence. The decay of the overshoot height as a function of the preshear strain is slower for larger shear rates.

3.4.3. Softening

Fig. 3.19 shows the effective modulus, G_{eff}, as the numerical derivative of the stress–strain curves at a fixed strain, $|\gamma(t) - \gamma_0| = 0.011$. The result for vanishing prestrains, γ_+, coincides only for the lowest shear rate with the corresponding bare Peclét number, $Pe_0 = 10^{-7}$, with the plateau shear modulus, G_∞. For the larger shear rates the generalized modulus is still larger than the plateau modulus. Therefore, fig. 3.19 shows the anelasticity for small times and motivates to evaluate the effective modulus at different strains, depending on the respective shear rates. In order to compare the effective modulus for each shear rate, I try to determine the strain, γ, for each shear rate. This is done in such a way, that the slope of a start–up curve does not deviate from the plateau modulus, G_∞, at that strain. The

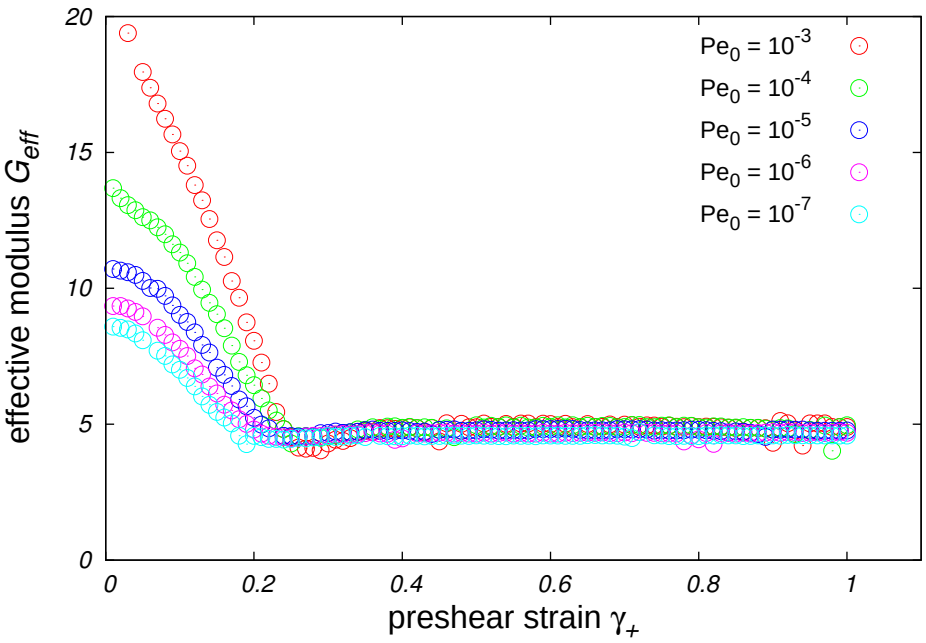

Figure 3.19.: Effective shear modulus G_{eff}, viz. the numerical derivative of the stress strain curve at $|\gamma(t) - \gamma_0| = 0.011$ as function of the previously applied strain.

values of the obtained strains are given in tab. 3.2. For the largest bare Péclet number, $Pe_0 = 10^{-3}$, the decay onto the plateau with the power law, t^{-a}, and the strain–induced yielding are overlapping, so that no intermediate plateau is observable. The resulting effective shear moduli, G_{eff}, as functions of the prestrain, γ_+, are shown in fig. 3.20.

By evaluating the effective moduli at the respective strains, it is ensured that the effective moduli are equal to the plateau modulus for vanishing preshear. The effective moduli decrease with increasing preshear strain until their minimal value at approximately the same preshear strain, at which the unload strain, $|\gamma_0 - \gamma_+|$, maximizes. For even larger preshear strains, the effective moduli increase again onto a value, which remains constant for further preshear. This asymptotic value for the effective modulus after large preshear decreases for increasing shear rates. When the flow is faster, the response is softer after a flow reversal. This result for the effective modulus, G_{eff}, contrasts with the dependence of the plateau modulus, G_∞, as a shear–rate independent quantity.

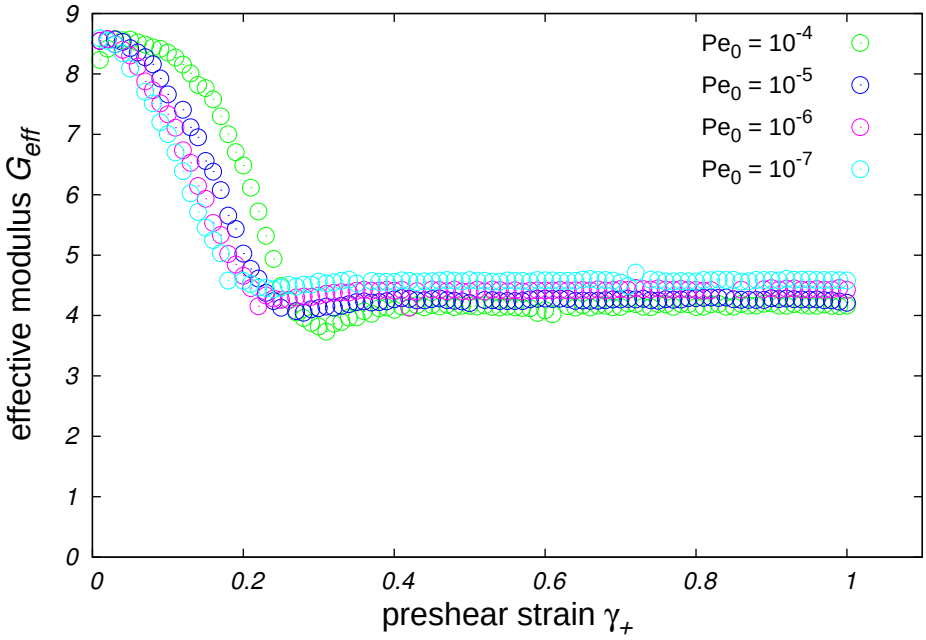

Figure 3.20.: Effective shear modulus G_{eff}, viz. the numerical derivative of the stress–strain curve at $|\gamma - \gamma_0| = 0.011, 0.018, 0.035, 0.043$, as function of the preshear strain, γ_+, for the separation parameter, $\varepsilon = 0$, and the other parameters as in tab. 3.2.

Pe_0	$\lvert\gamma(t) - \gamma_0\rvert$	ε	G_0	Γ	γ_c	γ^*	γ^{**}
10^{-7}	0.011	0	100	100	0.35	0.1	0.12
10^{-6}	0.018	0	100	100	0.35	0.1	0.12
10^{-5}	0.035	0	100	100	0.35	0.1	0.12
10^{-4}	0.043	0	100	100	0.35	0.1	0.12

Table 3.2.: F_{12} parameters used to compute the effective shear modulus, G_{eff}, as the slope of the stress strain curve at the respective strains, $|\gamma(t) - \gamma_0|$

In this chapter, I have shown the history–dependent response under shear reversal. The starting point, before applying preshear, is a quiescent glass or fluid at equilibrium. In this state, the material does not exhibit a macroscopic stress or strain. On the start–up of the preshear, the stress response increases with the preshear strain, the slope approaches the plateau modulus. At a critical strain, the stress response crosses over to a constant value. This crossover is observed in form of a stress overshoot. After a reversal of the shear flow, the stress decreases again, but at a nonvanishing strain. The stress decreases further, with smaller slope than for the response starting from a quiescent state. After the reversal, the stress overshoot has vanished or decreased compared to overshoots observed for start–up shear. I have discussed the preshear dependence of the residual strain, the relative overshoot

height and the apparent elasticity. Any of the quantities shows qualitative different results for preshear smaller and for preshear larger than a critical strain scale. This transition, the yielding transition, can be explained in the context of microscopic MCT [41, 26], the critical strain is connected to the maximal elastic deformation of the cages formed by neighboring particles. Further strain causes the cages to break and thus marks the onset of irreversible plastic flow. This corresponds to the onset of the nonlinearity of the response, a new type of dynamics compared to the quiescent scenario. The schematic MCT model predicts for any nonvanishing preshear strain a nonvanishing residual strain. Instead of an ideally elastic regime without residual strains and a sudden onset of the residual strain as signature of the yielding, the residual strain gradually increases with the preshear strain. Yielding causes a transition between the slow increase in the anelastic regime of preshear and the fast increase in the regime of plastic flow. That the unload strain, the difference of preshear and residual strain, remains constant for any preshear strain in the regime of plastic flow is consistent with its nature as a nonequilibrium steady state. The relative overshoot height decays smoothly with the applied preshear. The shape can be approximated by a compressed exponential function resulting in a still prominent overshoot after a flow reversal in the anelastic regime, and an almost vanished overshoot for a reversal in the steady state. I measure the slope of the stress–strain curve after a reversal of the shear flow at the respective strain corresponding to a point, when the slope of a start–up curve is equal to the plateau modulus. This slope decays with the preshear strain in the elastic regime and, after an undershoot, it remains constant for any preshear strain corresponding to the steady state. By varying the separation parameter, I have studied the density dependence of the preshear–dependent quantities. I can explain this dependence with the dependence of the plateau modulus on the separation parameter. This dependence goes back on the dependence of the nonergodicity parameter on the separation parameter, well–understood in quiescent MCT. The density dependence of the offset of the unload strain for large prestrains shows that the offset is a result of the initial anelasticity. For the relative overshoot height and the effective modulus the dependence on the separation parameter gradually vanishes with increasing preshear strain. Different shear rates, have also on impact on the history dependence. The unload strain, relative overshoot height and effective modulus, show a strong shear–rate dependent result for large preshear strains. This demonstrates the strong shear–rate dependence of the nonequilibrium steady state, the starting point after a reversal for large preshear strains, compared to the quiescent states, the starting points of start–up flow.

4. Inverted flow results

This chapter discusses the results for stress–controlled rheology obtained by numerical inversion of the model used in the previous chapter to describe rate–controlled rheology. The first section of this chapter introduces the method, how the strain response to an imposed stress is computed. The following sections, sec. 4.2, sec. 4.3 and sec. 4.4, discuss the subsequent time regimes of creep, or rather the strain response under constant stress. and connect the strain response to known dissipative processes of the glass and undercooled fluids. Sec. 4.5 summarizes the results for the strain response under constant stress and focuses on the implications on the yielding transition. Sec. 4.6 compares the theoretical results with the measurements from rheological experiments. The last section of this chapter, sec. 4.7, gives an overview of the strain response to imposed stress ramps.

4.1. Strain response

The concepts introduced in the previous sections to obtain the nonlinear stress response for applied shear can be inverted to find the matching mechanical response for a given stress.

In linear response theory, the generalized shear modulus, $G(t, t', [\dot{\gamma}(t'')])$ is approximated by the equilibrium modulus,

$$G(t, t', [\dot{\gamma}(t'')]) = G_{\mathrm{eq}}(t - t') + \mathcal{O}(\dot{\gamma}), \tag{4.1}$$

the higher orders in the external force, in this case the shear rate, are omitted.

The resulting Green–Kubo relation under the assumption that the system is at equilibrium at time, $t = 0$,

$$\sigma(t) = \int_0^t \mathrm{d}t' \; \dot{\gamma}(t') G_{\mathrm{eq}}(t - t'), \tag{4.2}$$

can be easily inverted to find the shear rate response to an applied stress,

$$\dot{\gamma}(t) = \int_0^t \mathrm{d}t' \; \sigma(t') \chi_{\mathrm{creep}}(t - t'), \tag{4.3}$$

with a generalized linear creep response function, $\chi_{\mathrm{creep}}(t)$.

The Laplace transforms of the linear response functions, $\mathcal{L}[\chi_{\mathrm{creep}}(t)] = \hat{\chi}_{\mathrm{creep}}(z), \mathcal{L}[G_{\mathrm{eq}}(t)] = \hat{G}_{eq}(z)$, fulfill a simple relation,

$$\hat{\chi}_{\mathrm{creep}}(z) = \frac{1}{\hat{G}_{\mathrm{eq}}(z)}, \tag{4.4}$$

which enables the the computation of linear creep response simply from the results of quiescent MCT.

However, the transition to nonlinear response is another question. I will solve the constitutive equation for the nonlinear stress response by numerical inversion as described in sec. A.1. The equations are discretized. The time–step duration is doubled every 8192 steps. The memory demand of an array of discretized time–correlation functions is close to the limit of the available random–access memory. The numerical inversion, as can be seen by the results in sec. 4.4,e.g. in fig. 4.15, is a well–conditioned problem for applied stresses far below the yield stress, $\sigma \ll \sigma_y$, and as well for applied stresses much larger than the yield stress, $\sigma \gg \sigma_y$. But close to the dynamical yield stress, small changes in the applied stress, $\sigma_y + \delta\sigma$, cause large changes in the resulting shear rate, $\dot{\gamma}(\sigma_y + \delta\sigma)$. As the condition number, $\frac{\|\dot{\gamma}(\sigma) - \dot{\gamma}(\sigma+\delta\sigma)\|}{\|\dot{\gamma}(\sigma)\|} \frac{\|\sigma\|}{\|\delta\sigma\|}$, increases for stresses, σ, close to the yield stress, the numerical inversion is ill–conditioned close to the yield stress. In order to keep the algorithm of the numerical inversion stable, each step has to be carried out with an increased relative accuracy, which magnifies the demands in memory and computation time.

4.2. Instantaneous creep

4.2.1. Instantaneous strain

In this part of the thesis, I want to study the strain response under constant applied stress, viz. creep.

The stress response to a step strain was studied in detail using the schematic model for time–dependent flows [49, 28, 40]. Ref. [40] distinguishes between instantaneous step strains and fast ramps. For the discussion of step stresses in this chapter, the results for instantaneous step strains, $\dot{\gamma}(t) = \gamma_0 \delta(t)$, are relevant. But one should keep in mind, that as the authors of ref. [40] argue, the schematic model is motivated by ITT–MCT for small bare Peclet numbers, $Pe_0 = \dot{\gamma}\tau_0$, and an instantaneous step is certainly outside the time regime of β–scaling. As a consequence, the interpretation of the constant, v_σ, as an instantaneous modulus, G_0, has to be taken with care.

The important result of step strains, from the perspective of studying step stress, is that an instantaneous step strain causes a step stress followed by a stress relaxation [28],

$$\sigma(t) = \gamma_0 G(t). \tag{4.5}$$

Inverting cause and effect, this stress relaxation is the reason, why a step stress cannot cause only a step strain response of the form, $\dot{\gamma}(t) = \gamma_0 \delta(t)$. The same processes, which cause the stress to relax (partially) after a step strain, have to be compensated by a delayed shear rate, $\delta\dot{\gamma}(t)$. The delayed shear rate is non–zero only for times, $t > 0$, if the stress is kept constant after an instantaneous step. This leads effectively to the ansatz for the strain response to an applied stress step, $\sigma(t) = \sigma\theta(t)$, that was originally used in ref. [50],

$$\dot{\gamma}(t) = \gamma_0 + \delta\dot{\gamma}(t). \tag{4.6}$$

The shear strain–rate response consists of an instantaneous elastic strain response, $\gamma_0\delta(t)$, and a delayed shear rate, $\delta\dot{\gamma}(t)$, which compensates the (partial) stress relaxation observed for step strains.

Therefore, the strain response of a stress step is composed of the instantaneous step response and the contributions of the delayed strain rate, $\gamma(t) = \gamma_0 \cdot \theta(t) + \int_0^t \mathrm{d}t' \, \dot{\gamma}(t')$. Then the solution of the constitutive equation becomes [50],

$$\sigma(t) = \int_{-\infty}^{t} \mathrm{d}t' \, \dot{\gamma}(t') \cdot G(t, t') \tag{4.7}$$

$$= \gamma_0 \cdot G(t, 0) + \int_0^t \mathrm{d}t' \, \dot{\gamma}(t') \cdot G(t, t'). \tag{4.8}$$

I will apply this approach to the schematic MCT–model, which was introduced in sec. 2.4, and study the strain rate which solves the constitutive equation for a constant stress step.

If I choose the product ansatz of ref. 2.4.3,

$$G(t, t') = v_\sigma(t, t') \, \phi^2(t, t'), \tag{4.9}$$

the term $G(t, 0)$ in eq.(4.8) becomes $G(0, 0) = G_0$ at time $t = 0$, if I set the applied stress, $\sigma(0) = \sigma$. For $t = 0$, the integral vanishes and the constitutive equation simplifies. The resulting equation is

$$\sigma(0) = \gamma_0 \cdot G_0. \tag{4.10}$$

This equation determines the instantaneous strain, γ_0, or instantaneously elastic response, as it is called in ref. [51], given as the applied stress over the instantaneous shear modulus, σ/G_0, fig. 4.1. In other publications [32, 33, 42], the instantaneous shear modulus is denoted by v_σ^* or ν_σ^0. It is a parameter in the schematic model, which sets the scale for the moduli and the stress.

As the creep response, $\gamma(t)$, scales with the stress, I will give the following results for creep curves for the rescaled strain, $\gamma(t)/\gamma_0$. The ratio between the creep strain, $\gamma(t)$, and the

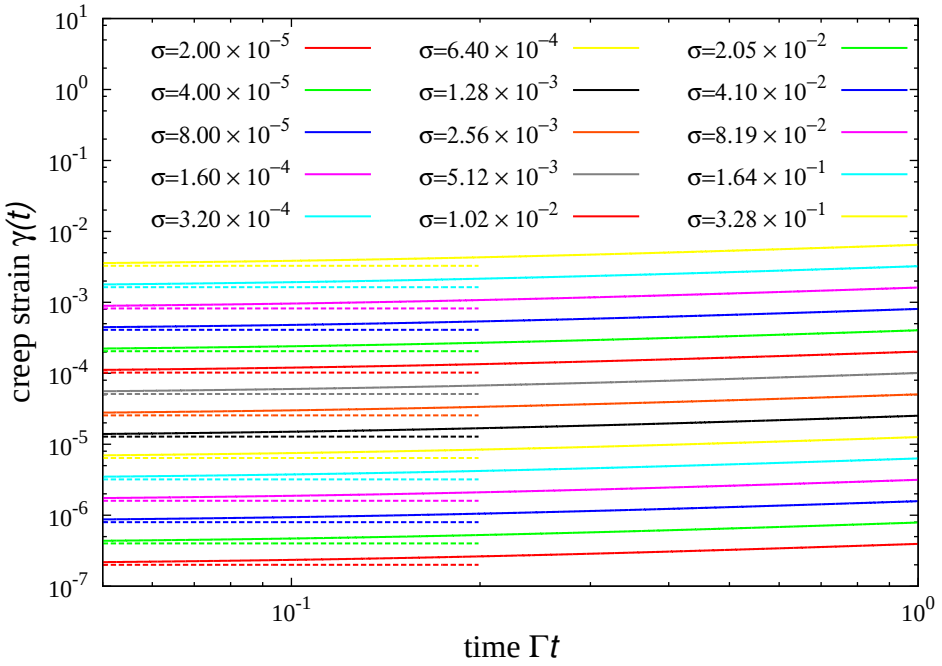

Figure 4.1.: Shear strain response, $\gamma(t)$, (full lines) for a given stress step, σ, separation parameter, $\varepsilon = 10^{-3}$, and the other parameters as in tab. 4.1. Dashed lines show the approximation, γ_0, for small times, $t \ll 1/\Gamma$.

applied stress, σ, is called the creep compliance,

$$J_c(t) = \frac{\gamma(t)}{\sigma}. \tag{4.11}$$

Therefore, the rescaled strain is equal to a dimensionless creep compliance, $J_c(t)G_0$.

G_0	Γ	γ_c	γ^*	γ^{**}
100	100	0.75	0.1	0.111

Table 4.1.: $F_{12}^{(\dot\gamma)}$–parameters used in the MCT computations for this section.

4.2.2. Instantaneous flow

As discussed in the previous subsection and in ref. [40], a step strain causes a step in stress, which will relax. The delayed strain rate, $\delta\dot\gamma(t)$, has to compensate this relaxation, i.e. the decay of the generalized shear modulus. For small times, $t - t' \ll 1$, instead of eq. (2.110), one can omit the memory integral and consider the following linear differential equation for

the density correlators,

$$\partial_t \phi(t,t') + \Gamma \phi(t,t') \approx 0, \tag{4.12}$$

with the initial conditions, $\phi(t,t) = 1$, and $\partial_t \phi(t,t')|_{t=t'} = -\Gamma$. This equation is solved by an exponentially decaying correlator,

$$\phi(t,t') \approx \exp\left(-\Gamma\,(t-t')\right). \tag{4.13}$$

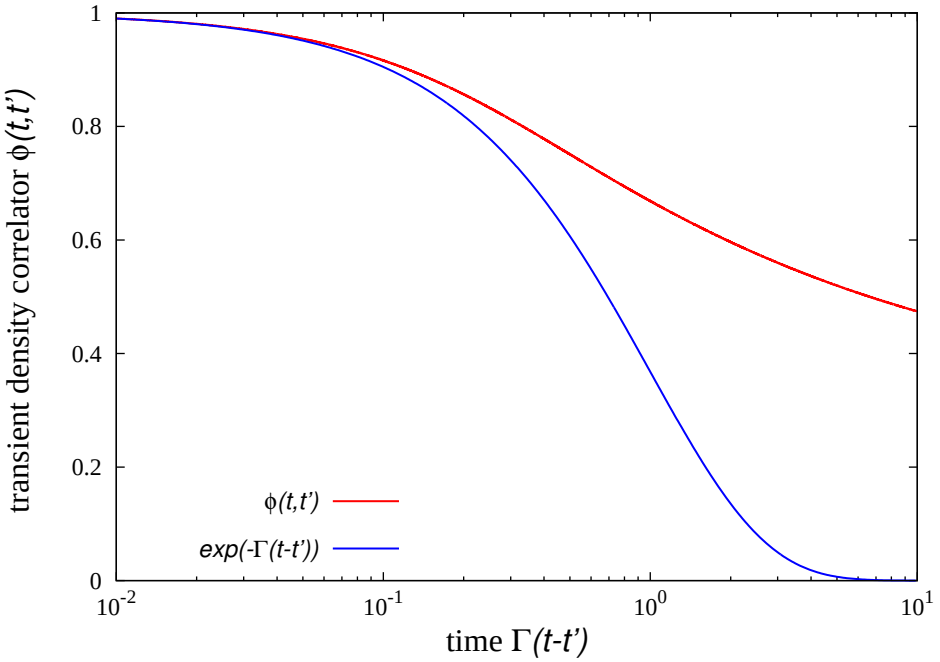

Figure 4.2.: Transient density correlator, $\phi(t,t')$, (red) for a given stress step, $\sigma = 10^{-2}$, separation parameter, $\varepsilon = 10^{-5}$, and the other parameters as in tab. 4.1 and its approximation, $\exp(-\Gamma(t-t'))$, (blue) for small times, $t - t' \ll 1$, rescaled by the initial decay rate, Γ.

The constitutive equation is then approximated by,

$$\sigma(t) \approx \gamma_0 \cdot G_0 \cdot \exp(-2\Gamma(t-0)) + \int_0^t \mathrm{d}t'\, \dot{\gamma}(t') \cdot G_0 \cdot \exp\left(-2\Gamma(t-t')\right) \tag{4.14}$$

$$\Leftrightarrow \int_0^t \mathrm{d}t'\, \dot{\gamma}(t') \cdot \exp\left(2\Gamma t'\right) = \left(\exp\left(2\Gamma t\right) - 1\right) \cdot \gamma_0, \tag{4.15}$$

which is solved by the delayed shear rate,

$$\dot{\gamma}_0 = \dot{\gamma}(t \to 0) = 2\Gamma\gamma_0 = 2\Gamma\frac{\sigma}{G_0}. \tag{4.16}$$

Hence, the solution for the strain for times, $0 < t \ll 1$, is given by,

$$\gamma(t) \approx \gamma_0 \cdot (1 + 2\Gamma \cdot t). \tag{4.17}$$

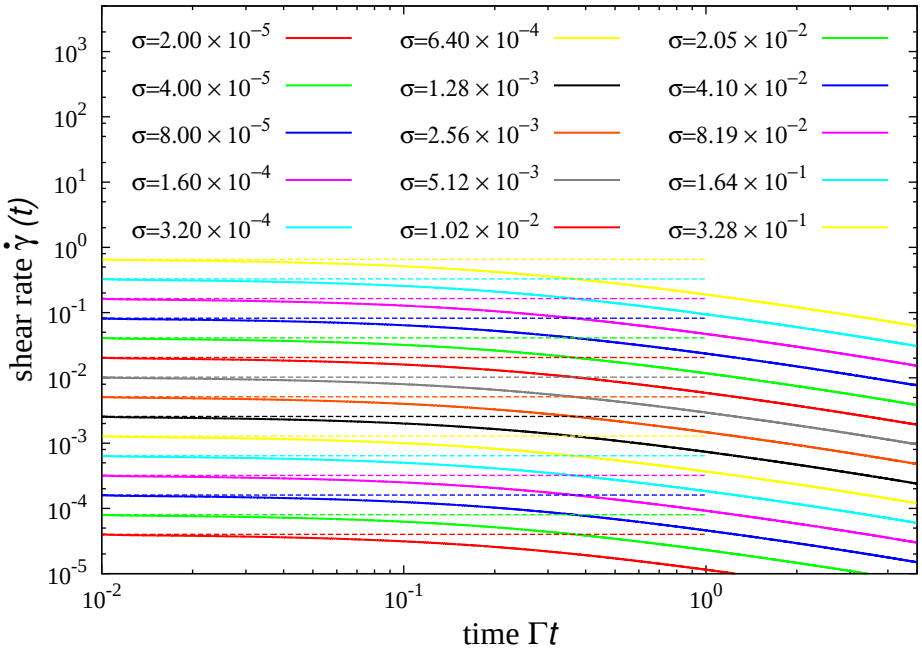

Figure 4.3.: Shear rate, $\dot{\gamma}(t)$, (full lines) for a given stress step, σ, separation parameter, $\varepsilon = 10^{-3}$, and the other parameters as in tab. 4.1. Dashed lines show the approximation, $2\Gamma\gamma_0$, for small times, $t \ll 1$.

In shear rate controlled rheology [37], the asymptotic stress for large shear rates for a constant stress–vertex function has been identified,

$$\sigma_\infty(\dot{\gamma} \to \infty) = \dot{\gamma} \int_0^\infty \mathrm{d}t' \; G_0 e^{-2\Gamma t'} \tag{4.18}$$

$$= \frac{\dot{\gamma} G_0}{2\Gamma}. \tag{4.19}$$

In sec. 2.4.3, I discuss that the same limit can be also received for a time–dependent stress–vertex function, if the strain scale of the vertex function, γ_*, rises faster than the strain scale of the asymptotic exponential decay, $\dot{\gamma}/\Gamma$. The result shows that the instantaneous shear rate of creep deformation, $\dot{\gamma} = \frac{2\Gamma\sigma}{G_0}$, is related to the high shear–rate asymptotic stress in previously applied models. The computations of the instantaneous creep response assume a finite elasticity, that remains unaffected when a step stress is applied. If the magnitude of the stress step approaches a critical stress scale, $\sigma \to G_0\gamma_*$, this is certainly not valid anymore,

as an instantaneous strain of this amplitude would deform the cages beyond the scale, at which they start to collectively break.

As the creep shear rate, $\dot{\gamma}(t)$, shows the trivial scaling as stated in eq. (4.17) and displayed in fig. 4.3 for small times, I will display further results for the creep shear rates rescaled by this initial shear rate, $\dot{\gamma}(t)/\dot{\gamma}_0$.

In quiescent mode–coupling theory [18], one finds an alternative version for the differentio–integral equation. This version contains also second derivatives. Analogously to the calculation above, I can omit the memory integral for small times, $t - t' \ll 1$, and obtain the following differential equation

$$\frac{\partial^2}{\Omega^2 \partial t^2}\phi(t,t') + \frac{\nu\partial}{\Omega^2\partial t}\phi(t,t') + \phi(t,t') \approx 0, \tag{4.20}$$

and the initial conditions are, $\phi(t,t) = 1$, and $\dot{\phi}(t,t) = 0$. This equation is solved by,

$$\phi(t,t') \approx \exp\left(-\frac{\nu t}{2}\right)\cos\left(\frac{1}{2}\sqrt{4\Omega^2-\nu^2}t\right) + \nu\frac{\sin\left(\frac{1}{2}\sqrt{4\Omega^2-\nu^2}t\right)}{\sqrt{4\Omega^2-\nu^2}}. \tag{4.21}$$

Using this approximation in the constitutive equation yields for the strain an approximate solution, which increases quadratically in time,

$$\gamma(t) \approx \gamma_0 \cdot (1 + \frac{1}{2}\Omega^2 t^2) + \mathcal{O}(t^3). \tag{4.22}$$

4.3. Creep resulting from the β–process

4.3.1. Fast β–process

β–scaling shows, that at the critical packing fraction of the glass transition, $\varepsilon = 0$, the density correlator decays, $\phi(t) \approx f_c + (1-f_c)^2\left(\frac{t}{t_0}\right)^{-a}$.

If one inserts this approximation in eq. (4.7),

$$\sigma(t) = \int_0^t \mathrm{d}t'\dot{\gamma}(t')G_0\left(f_c^2 + 2f_c(1-f_c)^2\left(\frac{t-t'}{t_0}\right)^{-a} + (1-f_c)^4\left(\frac{t-t'}{t_0}\right)^{-2a}\right), \tag{4.23}$$

a Laplace transformation, defined as,

$$\mathcal{LT}\left[f(t)\right](z) \equiv \hat{f}(z) = \int_0^\infty \mathrm{d}t \quad e^{-zt}f(t), \tag{4.24}$$

is helpful to find approximate solutions.

The Laplace transform of the constitutive equation reads,

$$\frac{\sigma}{z} \approx z\hat{\gamma}(z)G_0\left(\frac{f_c^2}{z} + 2f_c(1-f_c)^2 t_0^a \Gamma(1-a) z^{-1+a} + (1-f_c)^4 t_0^{2a}\Gamma(1-2a)z^{-1+2a}\right), \quad (4.25)$$

and it is solved for the Laplace transform of the shear rate, $\dot{\gamma}(t)$,

$$\mathcal{LT}\left[\dot{\gamma}(t)\right] = z\hat{\gamma}(z) \approx \frac{\sigma}{G_0 f_c^2}\frac{1}{1+\frac{2(1-f_c)^2\Gamma(1-a)t_0^a}{f_c}z^a + \frac{(1-f_c)^4\Gamma(1-2a)t_0^{2a}}{f_c^2}z^{2a}} \quad (4.26)$$

$$= \frac{\sigma}{G_\infty}\frac{1}{1+\frac{2(1-f_c)^2\Gamma(1-a)t_0^a}{f_c}z^a + \frac{(1-f_c)^4\Gamma(1-2a)t_0^{2a}}{f_c^2}z^{2a}}. \quad (4.27)$$

Instead of finding an exact inverse transform to obtain the shear rate, the expression above can be differently approximated for three time regimes.

If $|z| \gg 1/t_0$, the third term of the denominator will dominate,

$$z\hat{\gamma}(z) \approx \frac{\sigma}{G_\infty}\frac{1}{(}1-f_c)^4\frac{\Gamma(1-2a)t_0^{2a}}{f^2}z^{2a} \quad (4.28)$$

$$\dot{\gamma}(t) \approx \frac{\sigma}{G_0}\mathcal{LT}^{-1}\left[\frac{1}{(1-f_c)^4\Gamma(1-2a)t_0^{2a}}z^{-2a}\right] \quad (4.29)$$

$$= \frac{\sigma}{G_0}\frac{1}{(1-f_c)^4\Gamma(1-2a)\Gamma(2a)t_0^{2a}}t^{-1+2a}. \quad (4.30)$$

The regime of $|z| \gg 1/t_0$, is equivalent to the short–time regime, $t \ll t_0$, so the approximation obtained for the shear rate would only hold for short times. But for those times the approximation of eq. (4.23) does not hold, the density correlator has, $\phi(t,t) = 1$ and $\partial_t\phi(t,t')|_{t=t'} = -\Gamma$, as initial conditions. I discussed the evolution of the creep on short times in the previous section, the the Laplace transform, $z\hat{\gamma}(z)$, is only relevant asymptotically, $|z| \ll 1$, to determine the long–time evolution of the glassy dynamics.

4.3.2. Andrade creep

At inter mediate values of $|z|$, the middle term of the denominator in eq. (4.26) becomes dominant

$$z\hat{\gamma}(z) \approx \frac{\sigma}{G_\infty}\frac{1}{\frac{2(1-f_c)^2\Gamma(1-a)t_0^a}{f_c}z^a} \quad (4.31)$$

$$\dot{\gamma}(t) \approx \frac{\sigma}{G_\infty}\mathcal{LT}^{-1}\left[\frac{f_c}{2(1-f_c)^2\Gamma(1-a)t_0^a}z^{-a}\right] \quad (4.32)$$

$$= \frac{\sigma}{G_\infty}\frac{f_c}{2(1-f_c)^2\Gamma(1-a)\Gamma(a)t_0^a}t^{-1+a}. \quad (4.33)$$

This power law is not an asymptotic power law as it is only dominant on intermediate times. Additionally, due to the fact, that the approximation in eq. (4.23) does not agree

with the initial conditions of the schematic model, it does not agree with the computations. It is mentioned here nevertheless, because $\dot{\gamma}(t) \propto t^{-1+a}$ is close to so–called Andrade creep $\dot{\gamma}(t) \propto t^{-2/3}$ found for metal wires [52] and simulations for dislocation dynamics [53]. If one takes the initial strain step (4.8) into account, the corresponding strain reads,

$$\gamma(t) \approx \gamma_0 \left(1 + \frac{1}{2f_c(1-f_c)^2 a\Gamma(1-a)\Gamma(a)t_0^a} t^a \right), \tag{4.34}$$

which reminds of Andrade's result [52],

$$l(t) = l_0 \left(1 + \beta t^{\frac{1}{3}} \right), \tag{4.35}$$

where the result of the schematic MCT–model is, $\beta = \frac{1}{2f_c(1-f_c)^2 a\Gamma(1-a)\Gamma(a)t_0^a}$. Andrade's exponential long–time behaviour is discussed in sec. 4.4.5.

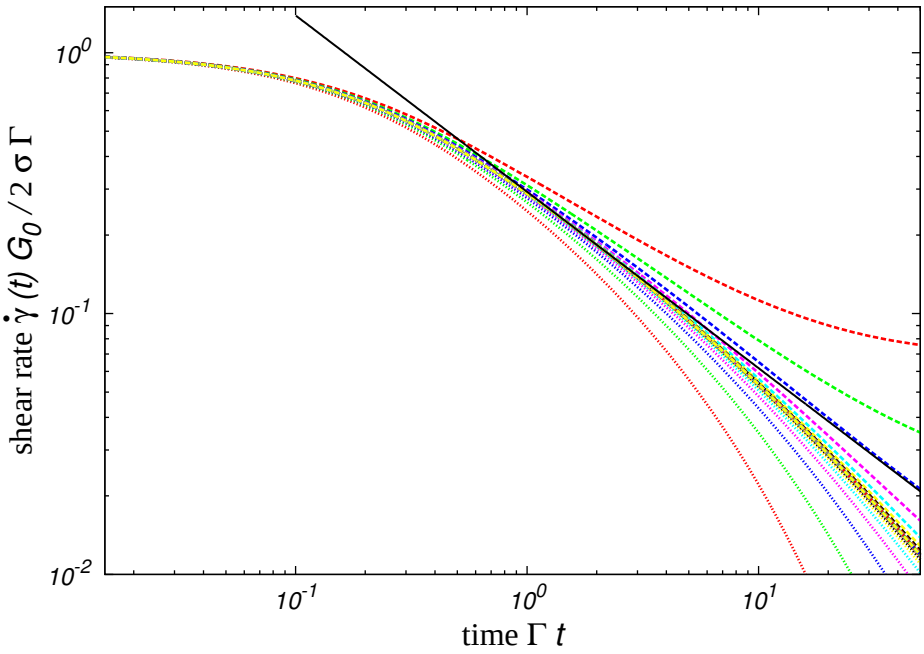

Figure 4.4.: Creep shear rate, $\dot{\gamma}(t)$, rescaled by the instantaneous shear rate as a function of rescaled time, Γt, for a given stress step, $\sigma = 10^{-6}$, various separation parameters, $\varepsilon = -10^1, \ldots, 10^{-1}$, and the other parameters as in tab. 4.1 compared to shear rate prediction, $\frac{\sigma}{G_\infty} \frac{f}{2\Gamma(1-a)\Gamma(a)t_0^a} t^{-1+a}$. For an enhanced comparison, the result from eq. (4.33) has been multiplied with a factor of 0.48 (full black line).

4.3.3. Asymptotic result for the fast β–creep

The long-time results for the shear rate of the fast β–process are found if one considers $|z| \ll 1/t_0$, then the third term in the denominator of eq. (4.26) can be neglected and the expression for the Laplace transform of the shear rate can be expanded as a geometric series,

$$z\hat{\gamma}(z) \approx \frac{\sigma}{G_\infty} \frac{1}{1 + \frac{2(1-f_c)^2\Gamma(1-a)t_0^a}{f} z^a} \tag{4.36}$$

$$= \frac{\sigma}{G_\infty} \left(1 - \frac{2(1-f_c)^2\Gamma(1-a)t_0^a}{f_c} z^a + \mathcal{O}\left(z^{2a}\right)\right) \tag{4.37}$$

$$\dot{\gamma}(t) \approx \frac{\sigma}{G_\infty} \mathcal{LT}^{-1}\left[1 - \frac{2(1-f_c)^2\Gamma(1-a)t_0^a}{f_c} z^a\right] \tag{4.38}$$

$$= \frac{\sigma}{G_\infty} \left(\delta(t) - \frac{2(1-f_c)^2\Gamma(1-a)t_0^a}{f_c\Gamma(-a)} t^{-1-a}\right) \tag{4.39}$$

$$= \frac{\sigma}{G_\infty} \left(\delta(t) + \frac{2(1-f_c)^2 a t_0^a}{f_c} t^{-1-a}\right). \tag{4.40}$$

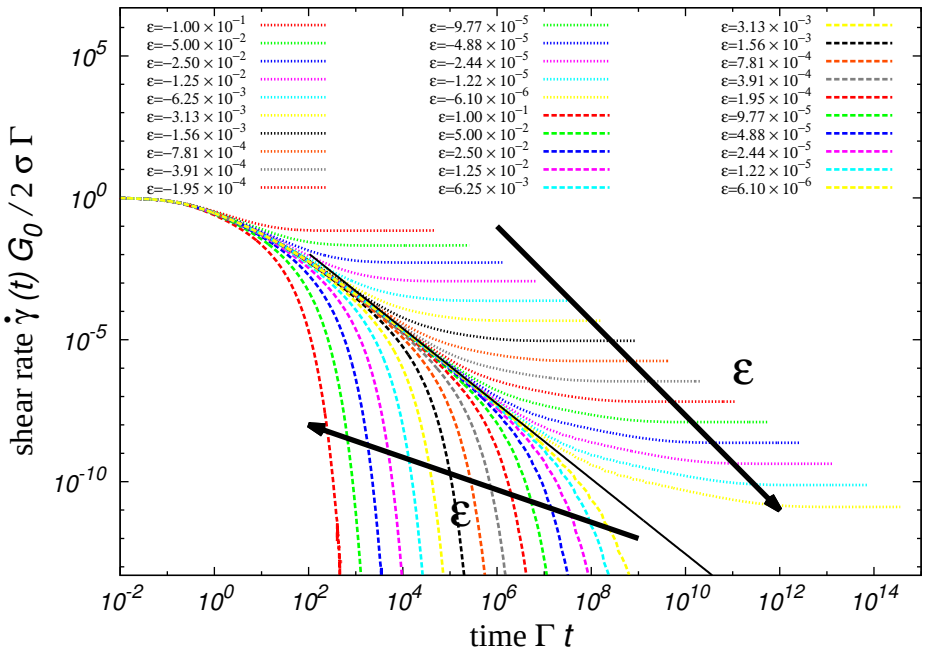

Figure 4.5.: Creep shear rate, $\dot{\gamma}(t)$, rescaled by the instantaneous shear rate as a function of the rescaled time, Γt, for a stress step, $\sigma = 10^{-6}$, various separation parameters, ε and the other parameters as in tab. 4.1. Dashed lines correspond to positive separation parameters, dotted lines to the negative separation parameters.

Close to the glass transition, $\varepsilon \approx 0$, the creep shear rate, $\dot{\gamma}$, approaches the asymptotic prediction from eq.(4.40) as shown in fig. 4.5. The figure shows the results for a very small

stress value, $\sigma = 10^{-6}$, as the numerical computations run faster for the small stress values, but does not change significantly for stresses up to 10^5 times larger.

4.3.4. Strain Plateau

The results of sec. 4.3 show that for stresses below the dynamical yield stress, $\sigma \ll \sigma_y$, the shear rate decays faster than logarithmically, $1/t$. The stressed glass behaves similar as a deformed solid and is strained up to a finite strain,

$$\gamma(t) \approx \gamma_\infty \left(1 - \frac{2t_0^a}{f_c} t^{-a}\right), \tag{4.41}$$

with the asymptotic limit in zeroth order,

$$\gamma_\infty \approx \frac{\gamma_0}{f_c^2} = \frac{\sigma}{G_\infty}. \tag{4.42}$$

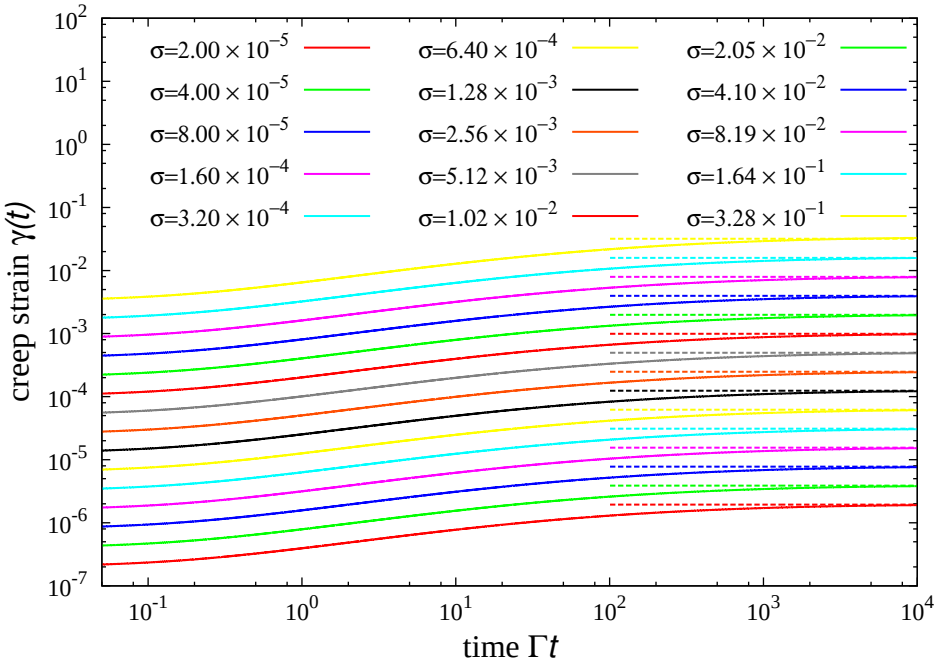

Figure 4.6.: Creep strain, $\gamma(t)$, (full lines) for various stress steps, σ, the separation parameter, $\varepsilon = 0$, and the other parameters as in tab. 4.1. The dashed lines show the corresponding plateau strains, $\gamma_\infty = \sigma/G_\infty$.

Fig. 4.6 proves, that the plateau strain, γ_∞, is proportional to the applied stress, σ.

This is the strain expected from an elastic solid with constant elastic shear modulus,

$G(t) = G_\infty$. The constitutive equation for this case reads,

$$\sigma(t) = \int_0^t \mathrm{d}t' \dot{\gamma}(t') G_\infty = G_\infty \int_0^t \mathrm{d}t' \dot{\gamma}(t'). \tag{4.43}$$

The existence of such states, when the internal stresses in the glass are stationary for a vanishing shear rate, $\dot{\gamma} = 0$, are known within the framework of MCT from the results for residual stresses [42, 54].

For simple shear, Hooke's law for the shear stress reads,

$$\sigma = G_\infty \gamma_\infty = G_0 f_c^2 \gamma_\infty, \tag{4.44}$$

and it is found to hold up to a density dependent stress scale, the yield stress σ_y. Deeper in the glass, for $\varepsilon > 0$, the asymptotic strain depends on the separation parameter,

$$\gamma_\infty(\varepsilon) = \frac{\sigma}{G_\infty(\varepsilon)} = \frac{\sigma}{G_0 \left(f_c + \lambda^2 \sqrt{\frac{\varepsilon}{1-\lambda}} + \mathcal{O}(\varepsilon) \right)^2}, \tag{4.45}$$

with the dependence of the nonergodicity parameter, $f_\varepsilon = f_c + \lambda^2 \sqrt{\frac{\varepsilon}{1-\lambda}} + \mathcal{O}(\varepsilon)$, following from (4.45). Fig. 4.7 shows, how the asymptotic strain in the glass depends on the separation parameter.

At the time, $t_\varepsilon = t_0 \varepsilon^{-\frac{1}{2a}}$, the power–law of the β–relaxation crosses over to an exponential decay onto the plateau,

$$\phi(t, t') \approx f_c + \lambda^2 \sqrt{\frac{\varepsilon}{1-\lambda}} \left(1 + \alpha^* \exp\left(-\beta^* t / t_\varepsilon\right)\right). \tag{4.46}$$

As the scaling function fulfills the scaling law of eq.(2.123), the time scale of the exponential decay is, $t_\varepsilon = t_0 \varepsilon^{-\frac{1}{2a}}$. For the efficiency of notations I will use the abbreviations,

$$f_\varepsilon = f_c + \lambda^2 \sqrt{\frac{\varepsilon}{1-\lambda}}, \tag{4.47}$$

$$\alpha_\varepsilon = \lambda^2 \sqrt{\frac{\varepsilon}{1-\lambda}} \alpha^*. \tag{4.48}$$

This exponential decay induces an exponential decay of the shear rate,

$$\dot{\gamma}(t) \approx \gamma_0 \mathcal{L}\mathcal{T}^{-1} \left[\frac{\beta^* + t_\varepsilon z}{\beta^* f_\varepsilon^2 + 2\alpha_\varepsilon t_\varepsilon z + f_\varepsilon^2 t_\varepsilon z} \right] \tag{4.49}$$

$$= \gamma_0 \frac{2\alpha_\varepsilon \beta^*}{(2\alpha_\varepsilon + f_\varepsilon^2)^2} \exp\left(-\frac{\beta^* f_\varepsilon^2}{(2\alpha_\varepsilon + f_\varepsilon^2) t_\varepsilon} t \right). \tag{4.50}$$

Terms containing only constants and delta–distributions have been omitted.

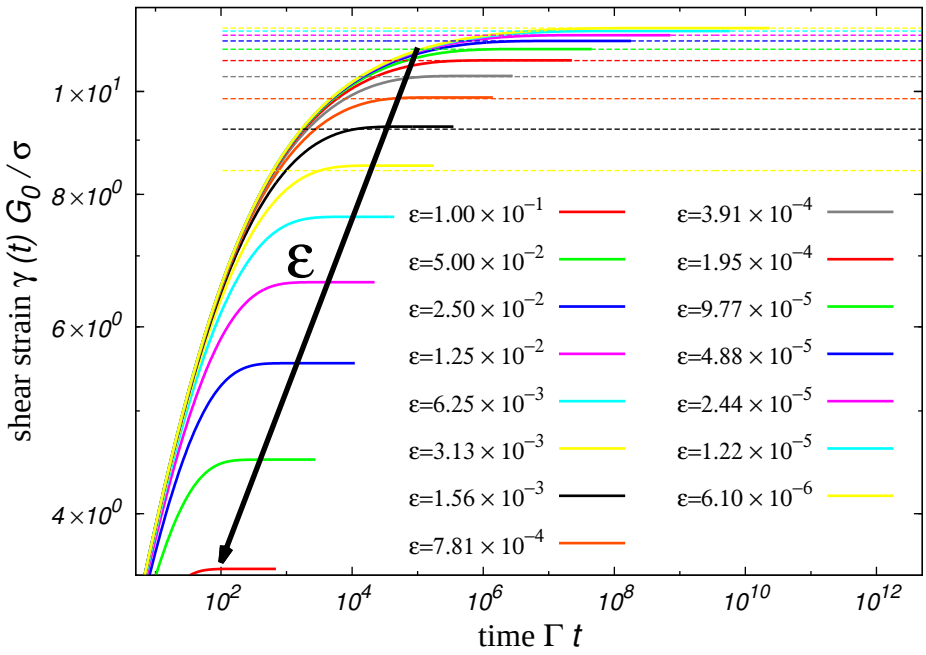

Figure 4.7.: Creep strain, $\gamma(t)$, rescaled by the instantaneous strain (full lines) for a stress step, $\sigma = 10^{-6}$, various separation parameters, ε, and the other parameters as in tab. 4.1. The dashed lines show the corresponding plateau strains, $\gamma_\infty = \sigma/G_\infty$.

Close to the glass transition, this exponential decay agrees with the numerical computed shear rate for various separation parameters, ε, as is shown in fig. 4.8. As the non–ergodicity parameter in eq. (4.47), f_ε, is obtained from β–scaling, the agreement between the estimated exponential decay and the computed curves is only comparable for densities sufficiently close to the glass transition, $|\varepsilon| \ll 1$.

At the same time, when the creep curve reached a plateau, the transient density correlation function, $\phi(t, 0)$, of the schematic model is close to its nonergodicity parameter, f. The time–evolution close to the nonergodicity parameter is based on the β–scaling of MCT–ITT. This implies that the transient time–correlation function of the density modes, $\phi_{\boldsymbol{q}(t,t')}(t, 0)$, are close to their respective nonergodicity parameters, $f_{\boldsymbol{q}}$. Inverse Fourier transformation, as in sec. 2.3.7, yields a collective probability, $f(\boldsymbol{r})$, for a particle to have moved from its initial position by the distance, $\boldsymbol{r}(t, t')$. Fig. 4.9 shows the result, the distorted version of the quiescent cage. For the figure, I have chosen the strain of the distortion at a strain, $\gamma = 10\%$, too large for the linear response approximation, but smaller distortions are barely significant on a linear scale.

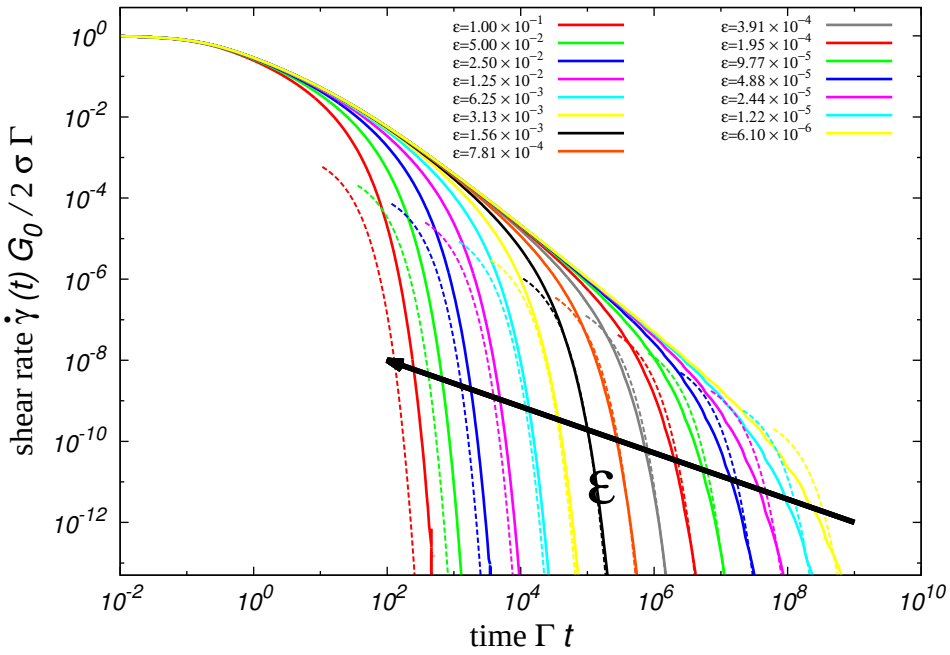

Figure 4.8.: Creep shear rate, $\dot{\gamma}(t)$, rescaled by the instantaneous shear rate as a function of the rescaled time, Γt, for a stress step, $\sigma = 10^{-6}$, various separation parameters, ε and the other parameters as in tab. 4.1. Dashed lines correspond to the exponential decay predicted by eq. (4.50).

4.3.5. Logarithmic creep

The asymptotic creep law, eq. (4.40), and the exponentially decaying creep, eq. (4.50), are in contrast to the results found in experiments [55, 56], and also the predictions by a generalized Maxwell model [50] and theories for soft glasses [57].

For the mentioned experiments and theories, the asymptotic shear rate decays as

$$\dot{\gamma}(t \to \infty) \propto t^{-1}. \tag{4.51}$$

Its integral, the strain, will creep logarithmically.

For the schematic model, I do not find such a decay, slopes proportional to t^{-1} exist only in the crossovers between power laws.

4.3.6. Intermediate time creep, the von Schweidler law

In the fluid, the second solution, eq. (2.122), of of the β-correlator equation induces another power law for the creep for longer times, $t \approx \tau_\alpha$. Solving the corresponding constitutive

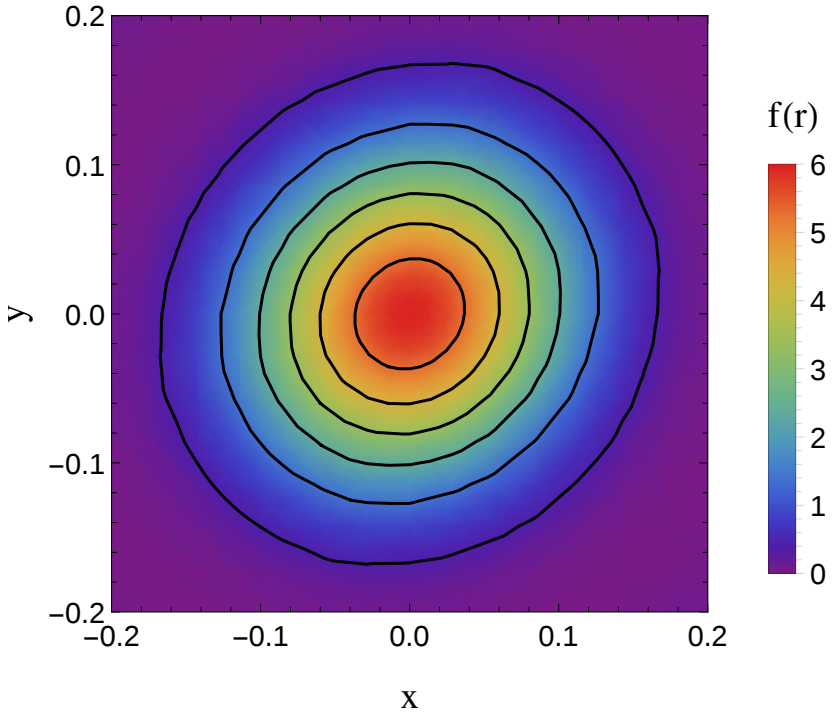

Figure 4.9.: Density plot of the Fourier transform of the non–ergodicity parameter, $f(\boldsymbol{r})$, in the plane of shear direction, x, and gradient direction, y, at a packing fraction, $\varphi = 0.52$, and the strain, $\gamma = 0.1$. Black contour lines mark steps of 1 for the function, $f(\boldsymbol{r})$.

equation,

$$\sigma(t) \approx \int_0^t \mathrm{d}t' \dot{\gamma}(t') G_0 \left(f_c^2 - 2(1-f_c)^2 f_c \left(\frac{t-t'}{\tau_\alpha} \right)^b \right), \tag{4.52}$$

analogously as eq. (4.40), yields for the shear rate,

$$z\hat{\dot{\gamma}}(z) \approx \frac{\sigma}{G_\infty} \frac{1}{1 - \frac{2(1-f_c)^2 \Gamma(1+b) \tau_\alpha^{-b}}{f_c} z^{-b}} \tag{4.53}$$

$$= \frac{\sigma}{G_\infty} \left(1 + \frac{2(1-f_c)^2 \Gamma(1+b)}{f_c \tau_\alpha^b} z^{-b} + \mathcal{O}(z^{-2b}) \right) \tag{4.54}$$

$$\dot{\gamma}(t) \approx \frac{\sigma}{G_\infty} \mathcal{L}\mathcal{T}^{-1} \left[1 + \frac{2(1-f_c)^2 \Gamma(1+b)}{f_c \tau_\alpha^b} z^{-b} + \mathcal{O}(z^{-2b}) \right] \tag{4.55}$$

$$\approx \frac{\sigma}{G_\infty} \left(\delta(t) + \frac{2(1-f_c)^2 b}{f_c \tau_\alpha^b} t^{-1+b} \right). \tag{4.56}$$

When the time approaches the α–decay time, τ_α, the shear rate will deviate from the

previously stated power law, eq. (4.40), and decrease approximately as,

$$\dot{\gamma}(t) \approx \frac{\gamma_0}{f_c^2} \frac{2(1-f_c)^2 \tau_\alpha^{-b} b}{f_c} t^{-1+b}. \tag{4.57}$$

Fig. 4.10 shows this power law, which becomes more prominent closer to the glass transition. For the curves computed far from the glass transition the scaling does not hold. Closer the the glass transition, the onset of the creep with the power law from eq. (4.57), is shifted to later times, as the α–decay time, τ_α, diverges. At this long times, numerical errors in the result for the shear rate start to have an impact, as can be seen in fig. 4.10 for the two separation parameters closest to the glass transition, $\varepsilon = 1.22 \times 10^{-5}$, and 6.10×10^{-6}.

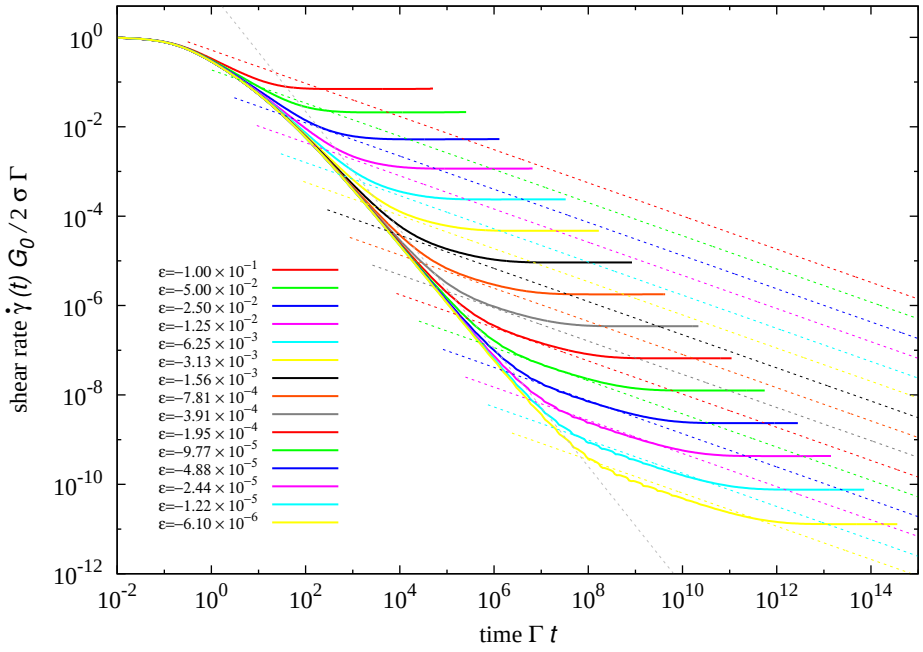

Figure 4.10.: Creep shear rate, $\dot{\gamma}(t)$, rescaled by the instantaneous shear rate as a function of the rescaled time, Γt, for a stress step, $\sigma = 10^{-6}$, various separation parameters, ε and the other parameters as in tab. 4.1. Dashed lines correspond to the v. Schweidler–induced creep predicted by eq. (4.57), the gray dashed line shows the asymptotic power law of eq. (4.40) for a comparison.

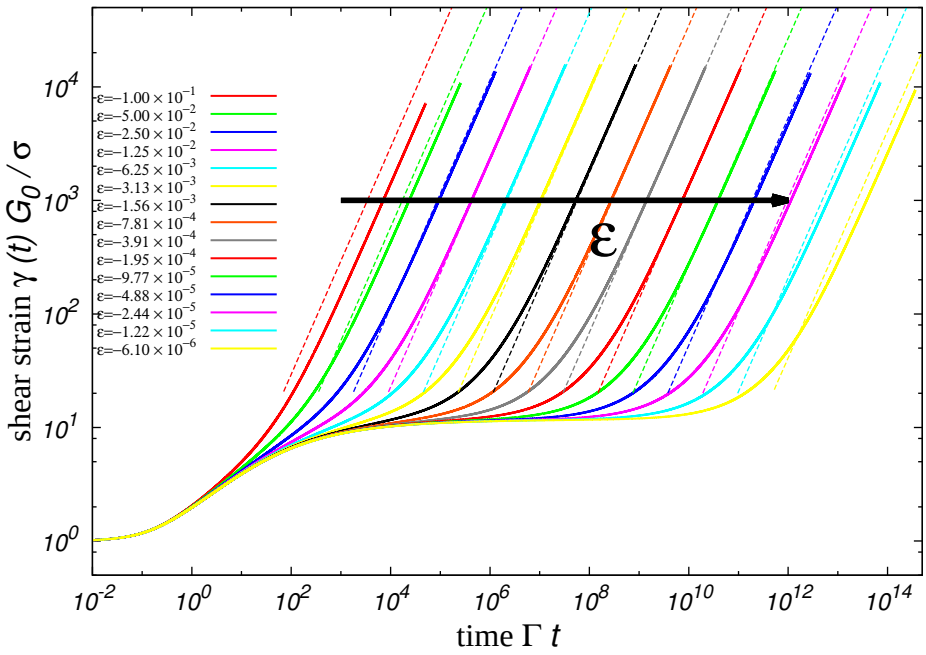

Figure 4.11.: Creep strain, $\gamma(t)$, rescaled by the instantaneous strain as a function of rescaled time, Γt, for a given stress step, $\sigma = 10^{-6}$, for various separation parameters corresponding to a fluid, i.e. $\varepsilon < 0$, and the other parameters as in tab. 4.1. Dashed lines show the asymptotic linear increase predicted by eq. (4.60).

4.4. Flow regime, steady–state creep

4.4.1. Linear fluid

The asymptotic behaviour of the strain in the fluid is always flow, $\gamma \propto t$, the strain increases linearly in time. This linear increase can be mapped to strain–controlled situations. The relation between the given stress, σ, and the obtained long–time limit for the shear rate, $\dot{\gamma}_\infty$, is the same found for a given shear rate, $\dot{\gamma}$, and the obtained long–time limit of the stress, σ_∞. If the stresses are sufficiently small, that the creep response can be approximately described as linear response, the α–process shows good agreement with Kohlrausch fits [58]. For the longest times, the Kohlrausch laws can be replaced by exponential fits, as I have discussed in sec. 2.4.2. Exponential fits restrict the time domain, in which they show a good agreement for the obtained approximation, further than Kohlrausch fits, but they have the advantage of being easier to handle under Laplace and inverse Laplace transformations. Following the assumptions that an exponential fit agrees with the MCT results on long–time scales, the generalized shear modulus obeys, $G(t) = f_c^2 e^{-2c_\alpha t/\tau_\alpha}$, with a constant, c_α, introduced to compensate the replacement of the Kohlrausch law, $e^{-(t/\tau_\alpha)^b}$, by an exponential, $e^{-c_\alpha t/\tau_\alpha}$. For the parameters as used in tab. 2.1, the constant is, $c_\alpha = 3.9$.

The long–time limit for the shear rate in the linear–response flowing state is given by,

$$\dot{\gamma}(t) \approx \frac{\gamma_0}{f_c^2} \mathcal{L}\mathcal{T}^{-1} \left[1 + \frac{2c_\alpha}{z\tau_\alpha} \right] \tag{4.58}$$

$$= \frac{\gamma_0}{f_c^2} \left(\delta(t) + \frac{2c_\alpha}{\tau_\alpha} \right). \tag{4.59}$$

The corresponding strain increases linearly in time,

$$\gamma(t) \approx \frac{\gamma_0}{f_c^2} \frac{2c_\alpha}{\tau_\alpha} t. \tag{4.60}$$

The exponential fit has to fulfill the two–parameter scaling law, eq. (2.123), the decay time, τ_α, is consequently the α–decay time from eq. (2.130).

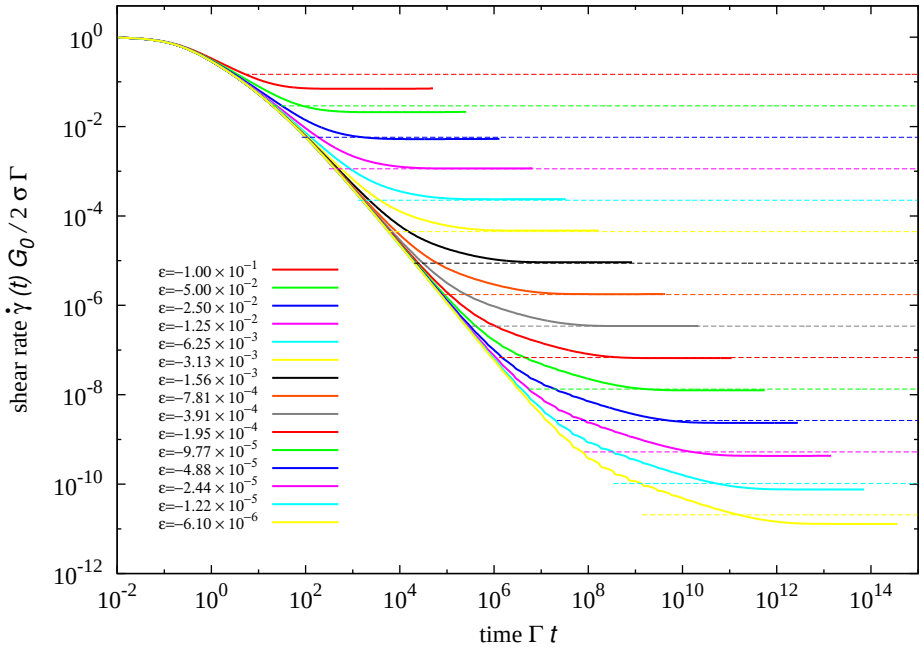

Figure 4.12.: Creep shear rate, $\dot{\gamma}(t)$, rescaled by the instantaneous shear rate as a function of rescaled time, Γt, for a given stress step, $\sigma = 10^{-6}$, for various separation parameters corresponding to a fluid, i.e. $\varepsilon < 0$, and the other parameters as in tab. 4.1. Dashed lines show the asymptotic shear rate predicted by eq. (4.59).

Fig. 4.11, and fig. 4.12 show the asymptotic flow result for the strain, γ, and the shear rate, $\dot{\gamma}$, of a linear–response fluid. The asymptotic flow of these fluids agrees with α–scaling, but as for the v. Schweidler law, deviations from the predictions occur far from the bifurcation point and due to numerical issues for long times as well. The scaling is highlighted in fig. 4.13, where all asymptotic shear rates coincide with the previously described exceptions.

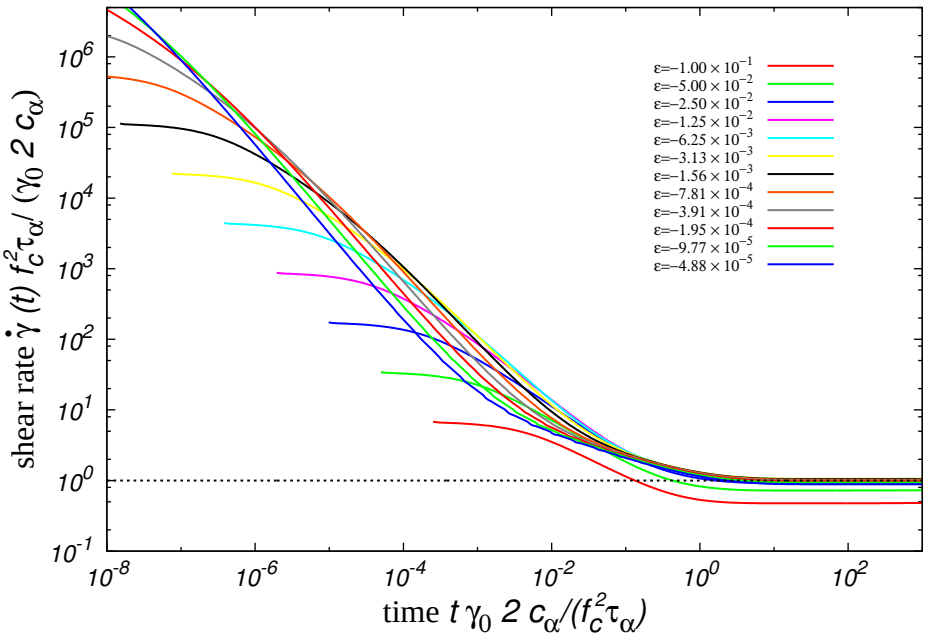

Figure 4.13.: Creep shear rate, $\dot{\gamma}(t)$, rescaled by the asymptotic shear rate, eq. (4.59), as a function of time, t, also rescaled by the asymptotic shear rate for a given stress step, $\sigma = 10^{-6}$, for various separation parameters corresponding to a fluid, i.e. $\varepsilon < 0$, and the other parameters as in tab. 4.1. The black dashed line marks one.

4.4.2. Shear–melted glass

In the glass, the same asymptotic behaviour of flow, i.e., linearly increasing strain, is found for sufficiently large stresses. The imposed stress has to be larger than the yield stress, σ_y. The yield stress can be related to a yield strain, $\gamma_y = \frac{\sigma_y}{G_\infty}$. γ_y is related to the strain scales,γ_c, and γ^*, that mark the point when shear advection begins to induce the decay of the memory kernel and the generalized shear modulus for the schematic model, respectively. Fig. 4.14 shows, that also the glass flows asymptotically for large imposed stresses. The asymptotic shear rates of this flow are discussed in the following subsection, the onset of this asymptotic flow is discussed at the end of this section.

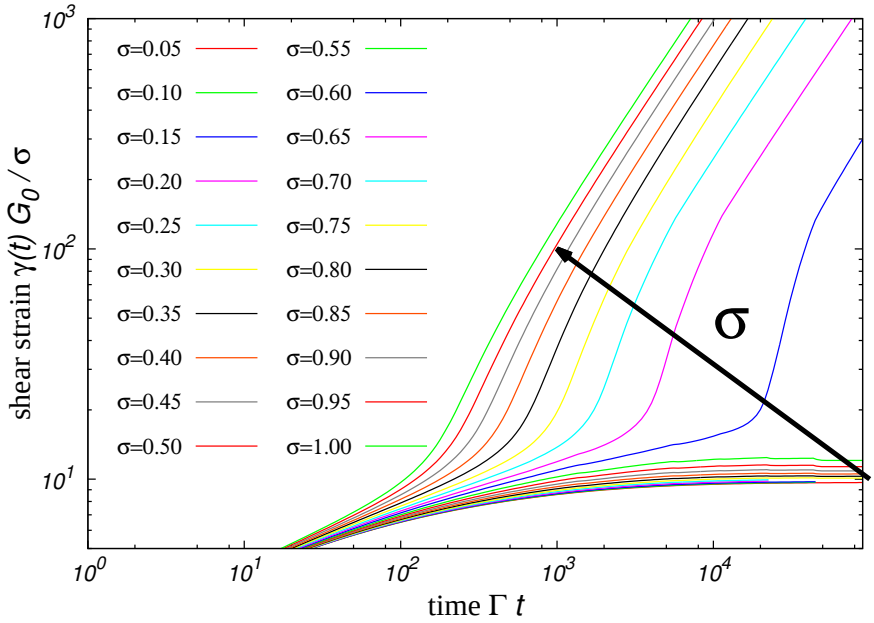

Figure 4.14.: Creep strain, $\gamma(t)$, rescaled by the instantaneous strain (full lines) for various stress steps, σ, the separation parameter, $\varepsilon = 10^{-3}$, and the other parameters as in tab. 4.1.

4.4.3. Flow curves

The memory kernel, $m(t, s, t')$, and the shear modulus, $G(t, t')$, decay when a constant shear rate is applied. This implies that also the memory of previous deformations does not influence the response, if a constant shear rate is applied long enough. This holds naturally for asymptotic flow, when the shear rate is applied for infinite long times.

As flow curves have been shown to be monotonous [31], only one asymptotic shear rate agrees with the applied constant stress. The fact, that shear induces the decay of the memory kernel and the modulus, does not lead automatically to asymptotic flow under constant stress. But together with the monotonicity of the flow curves from constant rate computations, it implies that if asymptotic flow is a solution, than it is unique. As the flow curves are unique, if one defines the flow curve as steady stress vs. steady shear rate, this also implies that there can be now asymptotic flow, viz. a constant asymptotic shear rate, for applied stresses smaller than the dynamical yield stress found for rate controlled computations.

Fig. 4.15 compares the flow curves from fixed–rate computations and fixed–stress computations, viz. steady shear and creep. The flow curves agree, when a steady state has been reached. The blue discs placed on the axes of fig. 4.15, correspond to stresses, for which no asymptotic flow or creep which increases logarithmically or faster has been observed. For three stress values, $\sigma = 0.45, 0.5, 0.55$, the computation could not be run sufficiently long to

determine the asymptotic result. The corresponding blue discs have been left out of the plot.

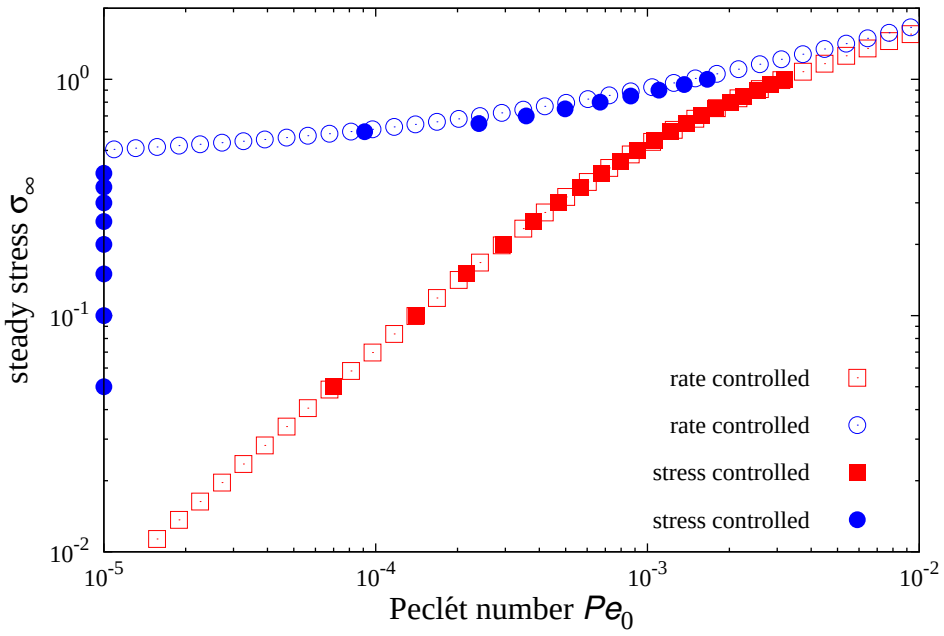

Figure 4.15.: Flow curves for parameters as in tab. 4.1. Blue circles show the flow curves for a glass, $\varepsilon = 10^{-3}$. The red squares show the flow curves for a fluid, $\varepsilon = -10^{-1}$. Filled symbols correspond to the asymptotic shear–rate results for fixed stresses, empty symbols correspond to asymptotic stress results for fixed shear rates. Blue circles placed on the axes have not exhibit asymptotic flow within the time of the computation.

4.4.4. Constant stress vertex

If I follow the ansatz of a constant stress–vertex function [37, 31, 38, 39, 40], $v_\sigma(t) = G_0$, the onset of the flow of the fluid and the glass is given by an approximation,

$$\sigma(t) \approx \int_0^t \mathrm{d}t' \dot{\gamma}(t') G_0 \left(f_c^2 - 2 f_c (1 - f_c)^2 c\,(t - t') \right), \tag{4.61}$$

with a constant, c, motivated by the scaling behaviour found in refs.[29, 31, 26]. Solving this equation in Laplace space gives,

$$\dot{\gamma}(t) \approx \frac{\gamma_0}{f_c^2} \mathcal{LT}^{-1} \left[\frac{z}{z - 2\frac{c}{f_c}} \right] \tag{4.62}$$

$$= \frac{\gamma_0}{f_c^2} \left(\delta(t) + \frac{2c}{f_c} + \mathcal{O}(t) \right). \tag{4.63}$$

One possibility for a decay of the modulus, linear in time, t, in the first order, would be an exponentially decaying modulus,

$$G(t) \propto \exp\left(-ct\right), \tag{4.64}$$

with a constant, $\tilde{c}$. This modulus generates the following solution for the shear rate,

$$\dot{\gamma}(t) = \frac{\gamma_0}{f_c^2} \mathcal{LT}^{-1} \left[\frac{\tilde{c} + z}{z} \right] \tag{4.65}$$

$$= \frac{\gamma_0}{f_c^2} \left(\delta(t) + \tilde{c} \right). \tag{4.66}$$

This shows, that an approximately exponential decay of the modulus, which agrees in first order with the results found in the β–scaling analysis for steady shear [29, 31, 26], generates a constant shear rate, viz. asymptotic flow. For a constant vertex function, the asymptotic flow results are consistent with the results of the schematic model under steady shear.

Fig. 4.16 shows the resulting creep curves. Although they do not show a delayed yielding as in fig. 4.14, the numerical computations show the same problems, that the computed curves are no smooth functions in time, especially close to the yield stress and after many decimation steps. This can be solved by computing the results with a higher precision, on the other hand this increases the computation time.

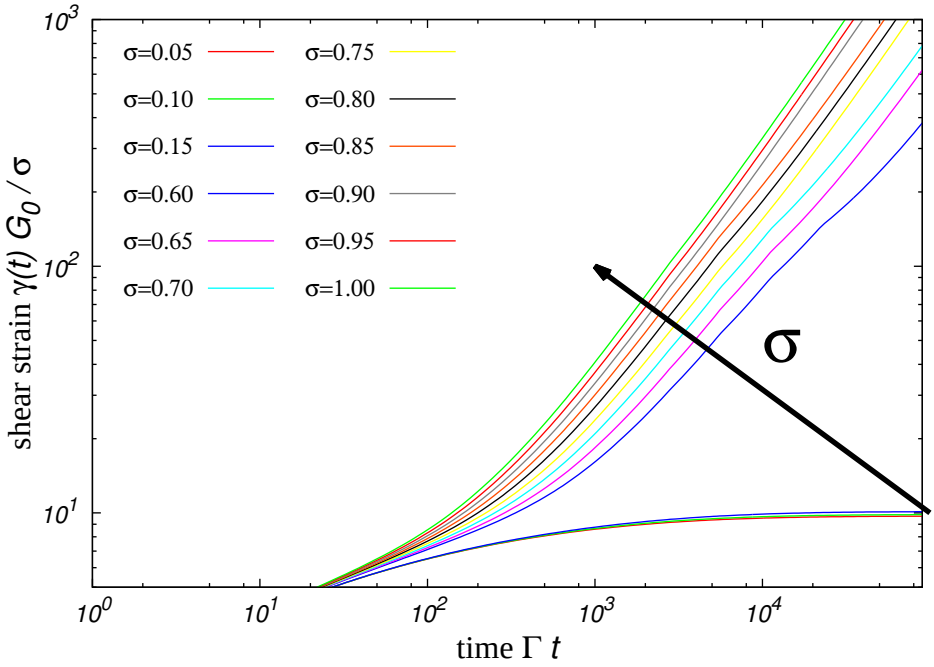

Figure 4.16.: Creep strain, $\gamma(t)$, rescaled by the instantaneous strain as a function of rescaled time, Γt, for various given stress steps, σ, the separation parameters corresponding to a glass, i.e. $\varepsilon = 10^{-3}$, a constant stress–vertex function, $v_\sigma(t, t') = G_0$, and the other parameters as in tab. 4.1.

4.4.5. Super–linear strain (tertiary creep), delayed yielding

In chap.2, I have shown the time evolution of the so–called stress–vertex function, eq.(2.153). It is connected to the strain–induced cage breaking at a given strain scale. A direct comparison between fig. 4.14 and fig. 4.16 shows that it is also connected to the phenomenon, which is known as delayed yielding for soft glasses [59, 60] or tertiary creep [50]. If the creep strain approaches a level close to the strain scale of the vertex function, $\gamma \to \gamma_* \approx 10\%$, one can see that the onset of asymptotic flow is preceded by a superlinear creep or sudden enhancement of the creep compliance. Therefore, it is a sound assumption that this effect might be connected to the same microscopic dynamics which induce stress overshoots and the Bauschinger effect in the form discussed in previous chapters.

The quantitative results of the schematic model for the onset of the flow are strongly determined by the choice of the vertex function, $v_\sigma(t, t')$. Fig. 4.17 shows the results for a time dependent vertex function as in eq. 2.153.

The result shown in fig. 4.17 can be interpreted in another way, if one introduces a time–

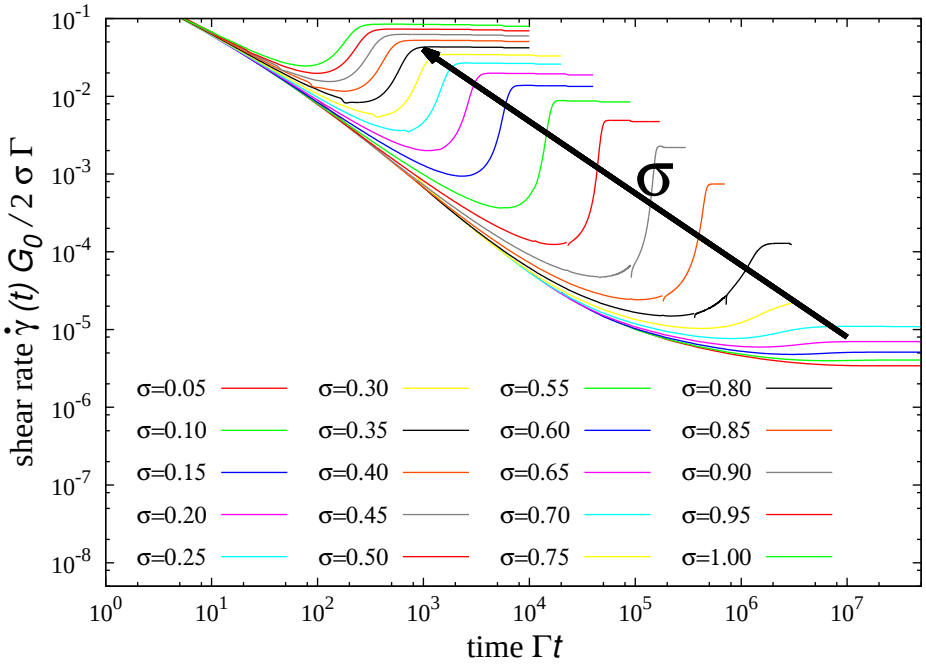

Figure 4.17.: Creep shear rate, $\dot{\gamma}(t)$, rescaled by the instantaneous shear rate as a function of the rescaled time, Γt, for various stress steps, σ, and the separation parameter, $\varepsilon = -10^{-3}$, and the other parameters as in tab. 4.1.

dependent viscosity,

$$\eta(t) = \frac{\sigma}{\dot{\gamma}(t)}, \tag{4.67}$$

as in ref. [61]. Normalizing the time–dependent viscosity by the instantaneous viscosity, $\eta_0 = \eta_\infty^{\dot{\gamma}}$, which I can identify with the high–shear–rate viscosity from rate–controlled experiments, makes it dimensionless.

Fig. 4.18 shows how the apparent viscosity evolves after a step stress was applied. For all stresses, the viscosity starts at the viscosity, $\eta_0 = \eta_\infty^{\dot{\gamma}}$, the lowest viscosity of the glass. At times, $t > t_0$, the viscosity increases, the glass starts to vitrify. According to eq. (4.40), the viscosity diverges like a power law, followed by an exponential divergence, eq. (4.50), for large times, $t > t_\varepsilon$. For applied stresses, larger than the yield stress, a bifurcation is observed. In fig. 4.18, these are the eight bottommost curves. The apparent viscosity, $\eta(t)$, follows approximately the diverging viscosity curves up to some value and then starts to deviate and increase to a lesser extent, before it decreases again on an asymptotic constant value. The decrease of the time–dependent viscosity, $\eta(t)$, is connected to a strain scale. In the schematic model, this is the parameter, γ_*.

The bifurcation between a finite asymptotic viscosity, $\eta(t \to \infty) = \eta_\infty$, and a diverging

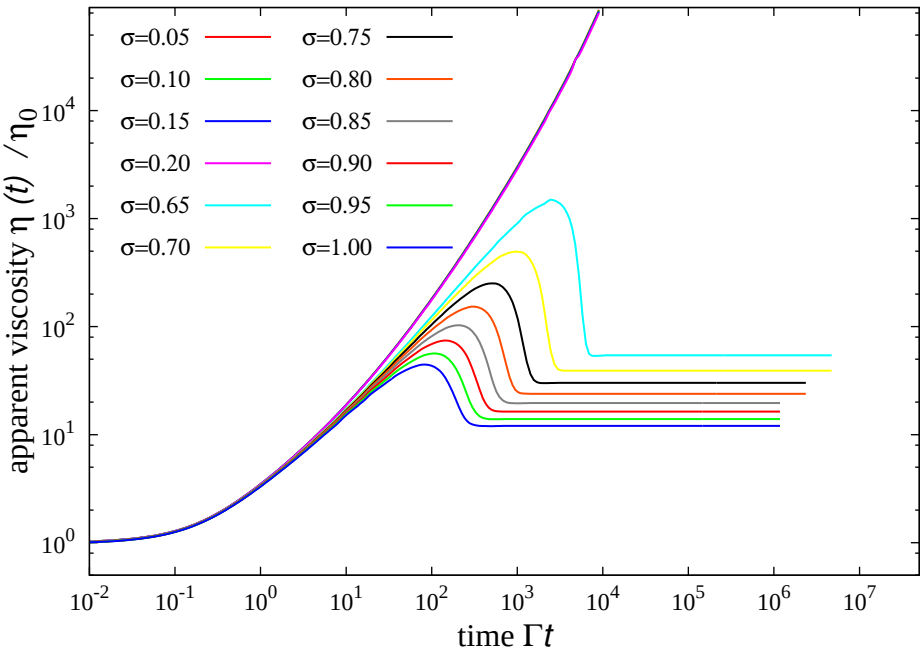

Figure 4.18.: Time–dependent viscosity, $\eta(t)$, as function of the rescaled time, Γt, for a glass, $\varepsilon = 10^{-3}$, for various applied stresses, σ and the other parameters as in tab. 4.1.

viscosity, $\eta(t \to \infty) \to \infty$, corresponds to the yielding transition from a shear–melted glass to a deformed solid glass. If the divergence of the viscosity was linear, the deformed solid glass would be replaced by a logarithmically creeping glass. A fluid, $\varepsilon < 0$, does not show a bifurcation in the viscosity. For each applied stress, σ, the time–dependent viscosity, $\eta(t)$, converges to a constant value for times larger than the α–decay time, $t > \tau_\alpha$.

4.5. Yielding transition

Since the earliest research on plasticity and viscosity, efforts have been made to categorize the experimental results. Bingham, who differentiated between viscous and plastic behaviour, proposed one of the simplest models [62], that features a critical stress, the yield stress. Below that yield stress, no flow is observed. Later studies question the existence of such a yield stress [63], and claim that all yielding materials show asymptotic flow if the measurement is sufficiently accurate for small stresses.

Fig. 4.19 provides a schematic overview for the results of the previous sections in this chapter. It shows the resulting dynamics in an applied stress vs. separation parameter (or packing fraction) plot.

Corresponding to the states known at zero stress [18], the diagram is separated into a fluid

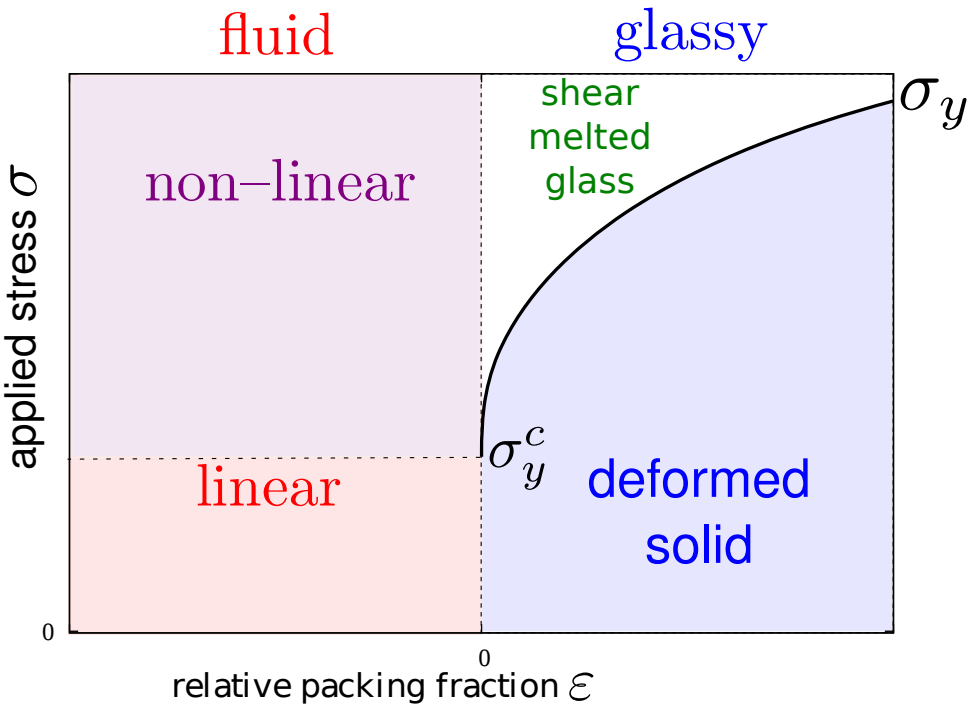

Figure 4.19.: Schematic phase diagram for supercooled fluids and glasses under constant stress.

region, $\varepsilon < 0$, and a region of glassy dynamics, $\varepsilon > 0$. The existence of asymptotic flow is found for the schematic model, as defined in sec. 2.4, in the whole fluid region and for the shear–melted glass, viz. for applied stresses above the dynamical yield stress. The dynamical yield stress, σ_y, is zero for the fluid and nonzero for the glass in accordance with ref. [29]. As the shear rate decays faster than logarithmically, eq. (4.40) and eq. (4.50), for applied stresses below the yield stress, the strain will converge to a finite asymptotic strain value. Hence, I attribute the section for the glassy dynamics below the yield stress to a deformed solid. The fluid dynamics is divided into a linear and a nonlinear response regime.

If I move along lines of constant stress from the linear response fluid towards the glass transition, the α–decay time, τ_α, which marks the onset of asymptotic flow in this regime, diverges as in eq. (2.130). Along lines of constant stress in the regime of the deformed solid towards the glass transition, the time scale that marks the onset of glassy arrest, t_ε , diverges as in eq. (2.128). In fig. 4.19, the transition line between the linear and nonlinear response regime for a fluid is placed at approximately the same stress value as the critical yield stress, σ_y^c. But flow curves resulting from rate–controlled computations show, that along the critical yield stress the time scale connected to the asymptotic flow, $1/\dot{\gamma}$, diverges slower than in the linear response regime, eq. (2.130). Hence, the nonlinearity of the fluid is in evidence for applied stresses of the magnitude of the critical yield stress, $\sigma \approx \sigma_y^c$.

The yielding transition is numerically very demanding to analyze with the discussed methods. Close to the yield strain, the solutions which show asymptotic flow or arrest are very close to each other. This slows down the iteration methods used for the numerical inversion.

Following the assumption, that the numerical inversion is legitimate, I can rule out, that asymptotic flow is caused by an applied stress smaller than the dynamical yield stress. Steady shear shows, that even the smallest applied shear rate results in a finite stress above the dynamical yield stress in the long–time limit. As a consequence, any applied stress larger than the yield stress results in asymptotic flow,

$$\lim_{t\to\infty} \gamma(t) \propto t. \tag{4.68}$$

The β–scaling analysis for scaling equations with a single time parameter are only valid, when either the accumulated strain, $\gamma(t,t')$, is negligible or given as a function of the difference of the time parameters, viz. time–translational symmetric, $\gamma(t,t') = \dot{\gamma}\ (t-t')$. This allows the analysis to be carried out in the regions of arrest and flow, but not for the transition in between. As the accumulated strain cannot be neglected, this might add intermediate correction terms. If they are slower than logarithmic, the asymptotic strain will be constant. Otherwise they will result in a sublinear increase of the strain. Using an alternative definition of the static yield stress as the instantaneous stress level which has to be overcome to start plastic flow of the material, viz. $\gamma(t) \propto t$, the so defined static yield stress can be identified with the dynamical yield stress. However, it is important to note, that the static yield stress is often defined in a different way.

A finite answer how the strain evolves in the schematic model under constant stress just below the yield stress, $\sigma(t) \lesssim \sigma_y$, cannot satisfactory be given without an analysis of the β–scaling equations for two time parameters. The question if the exponent, x, of the asymptotic strain evolution,

$$\lim_{t\to\infty} \gamma(t) \propto t^x, \tag{4.69}$$

changes continuously or jumps at the yielding transition, viz. the answer if the yielding transition is a first order or second order transition, is not provided by the methods which are used in this thesis. As the form of the stress–vertex function is phenomenological, the numerical inversion of the schematic model would be only valid for the specific model and the specific choice of the vertex function.

The yielding transition can also be understood as the transition from linear to non–linear response. For a linear stress response,

$$\sigma(t) = \int_{-\infty}^{t} \mathrm{d}t'\ \dot{\gamma}(t') G_{\mathrm{eq}}(t-t'), \tag{4.70}$$

higher orders in the shear rate $\dot{\gamma}$ can be omitted, at least approximately. In particular, the shear modulus, $G(t-t')$, does not depend on the shear rate and can be replaced by the solution from quiescent mode–coupling theory. In the fluid regime, the linear response is an approximation for small applied stresses. In flow controlled rheology, any applied shear rate, $\dot{\gamma}$, will set the time scale of the relaxation of the shear modulus and of the density correlators, eq. (2.132). As the shear induced decay is faster than the quiescent α–decay, this will make the shear modulus dependent on the shear rate for any shear rate. For the sake of completeness, I have to add, that the changes in the long–time tails of the modulus will decrease with the shear rate. In this way, the computation of the influence of the small shear rates requires at some point a numerical accuracy which cannot be provided.

Thus I have to conclude, that the linear response for the fluid is for any finite stress only an approximation, similar to the linear response of the glass which requires that the strain term in the β–scaling equation can be omitted as well. Steady–shear analysis provides nevertheless numerical methods to fairly quantify the dynamical yield stress as an asymptotic value of a sequence of steady stress response for decreasing shear rates, viz. the asymptotic stress response to steady shear with the constant shear rate, $\dot{\gamma} \to 0+$. Quantifying a transition line between the linear and the nonlinear fluid is not that easy. Close inspection of the data reveals, that any applied stress accelerates the decay of the shear modulus. Analogously, the so–called linear regime of the flow curves of rate–controlled computations is concave at a closer look.

Therefore, any transition line between the linear and the nonlinear fluid depends on an arbitrarily chosen level of accuracy. In fig. 4.20, I choose as criterion for the transition the relative deviation of the flow curve from its linear extrapolation at the smallest computed shear rate, $Pe_0 = 10^{-14}$, which exceeds 5 percent. The obtained transition line between the linear and non–linear fluid increases in stress when the density or separation parameter is decreased. This shape agrees intuitively with the observation, that dilute dispersions show rather Newtonian–like behaviour than shear–thinning effects. If the relative deviation, that marks the transition from linear to nonlinear response of the fluid, is set to a larger value, the corresponding transition line in fig. 4.20 is shifted to larger stress values.

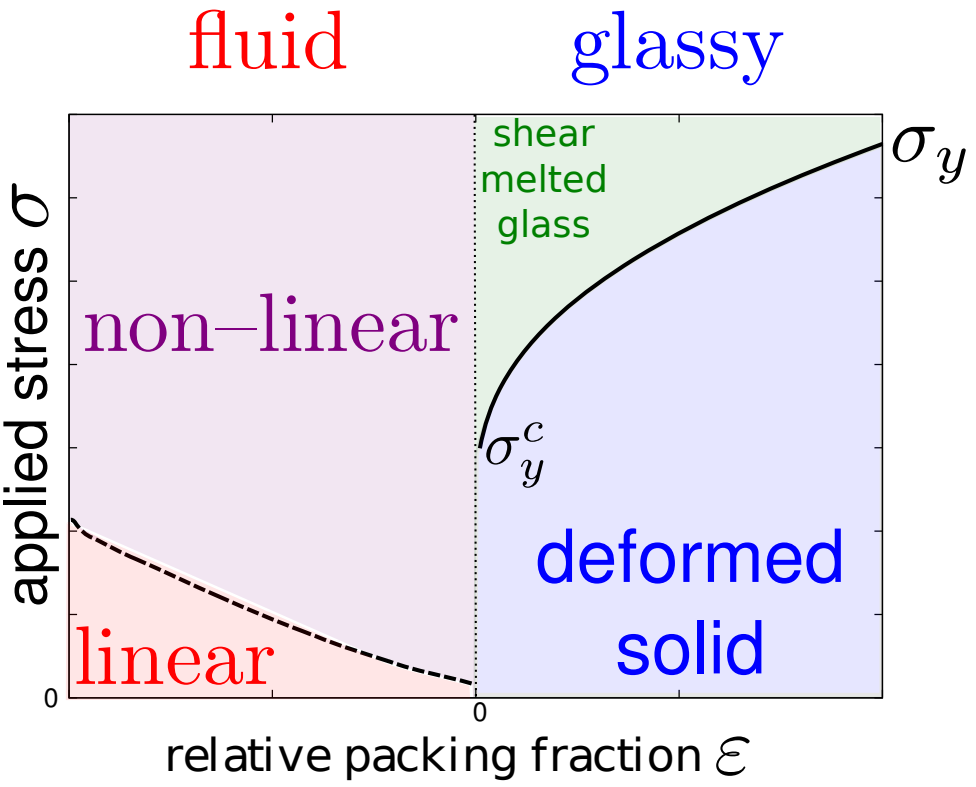

Figure 4.20.: Schematic dynamical phase diagram for the transition between a deformed solid and viscous flow.

4.6. Comparison between the theory and experiments

4.6.1. colloidal glasses

Rheological experiments lack the idealizations assumed in the previous sections. The instantaneous step deformation response, γ_0, would require the rheometer, which applies a step stress, to accelerate infinitely fast. But each rheometer has a certain moment of inertia. As discussed in refs. [64, 65], proportionality between applied stress and torque as well as between shear strain and angular displacement give rise to the equation,

$$a\ddot{\gamma} = \sigma_{\text{appl}} - \sigma_{\text{resp}}, \tag{4.71}$$

with a constant, a, which includes the moment of inertia of the rheometer and the constants of proportionality, determined by the rheometer's geometry.

For colloidal glasses, the solvent's viscosity, η_∞, or any equivalent quantities of the dominating dissipation processes have to be considered in the model as an additional aspect.

The discussed Kelvin-Voigt models [64, 65] are reproduced for the MCT ansatz if one

approximates the shear modulus by the elastic modulus $G(t) \approx G_\infty$. The occurrence of the inertio–elastic oscillations also depends on a critical elasticity, $G_c = \eta_\infty^2/4a$, the resulting strain response differs from the previously discussed results for an idealized response. The strain evolution onto the plateau value, γ_∞, now approximately reads,

$$\gamma(t) \approx \gamma\infty \left(1 - e^{-\frac{\eta_\infty}{2a}t}\left(\cos(\omega t) + \frac{\eta_\infty}{2a\omega\sin(\omega t)}\right)\right), \tag{4.72}$$

with the frequency, $\omega = \sqrt{\frac{G_\infty}{a} - \left(\frac{\eta_\infty}{2a}\right)^2}$. The creep curve, $\gamma(t)$, can be obtained numerically, if one replaces the constitutive eq. (4.7) by,

$$\sigma_{\text{appl}}(t) = \int_{-\infty}^{t} \mathrm{d}t'\, \dot\gamma(t') \cdot G(t,t') + \eta_\infty \dot\gamma(t) + a\ddot\gamma(t), \tag{4.73}$$

with the initial creep,

$$\gamma(t) = \frac{\sigma_0}{2a}t^2 + \mathcal{O}(t^3). \tag{4.74}$$

Via integration by parts and omitting boundary terms, I can rewrite eq. (4.73) in such a way, that the high–frequency viscosity and the inertia term become a part of a generalized shear modulus,

$$\sigma_{\text{appl}}(t) = \int_{-\infty}^{t} \mathrm{d}t'\, \dot\gamma(t') \cdot \left(G(t,t') + \eta_\infty\delta(t-t') + a\partial_{t'}\delta(t-t')\right), \tag{4.75}$$

This shows that the viscosity, η_∞, can be identified with the viscosity term, η_∞^ω, which I have discussed in eq. (2.144). In previous works [30, 50], this contribution has been called the high–frequency viscosity, as they dominate the linear loss modulus for high frequencies. Its domination of the linear loss modulus for high frequencies can be seen in fig. 2.4.

The inertia of the rheometer and of the sample affect the linear storage modulus for high frequencies, $G'(\omega) + a\omega^2$, as the inertia adds a term which increases quadratically in ω.

The high–frequency viscosity, η_∞, and the inertia constant, a, define a time scale, $\tau_{\text{rheo}} = \frac{2a}{\eta_\infty}$. For times small compared to this time scale, stress–controlled rheology will be dominated by by the effects of the high–frequency viscosity and the rheometer's momentum of inertia and geometry. If the time, τ_{rheo}, becomes small compared to the time scale of the initial decay, $1/\Gamma$, the experimental results can be compared to the results for the schematic model in the previous section. Fig. 4.21 shows, that the shear rate increases linearly for the smallest times before it decreases onto the instantaneous shear rate, known from eq. (4.17).

In good agreement with the results from sec. 4.4, the steady–state flow curve from constant–rate experiments and from stress–controlled experiments are consistent [50].

The experimental results by M. Siebenbürger for creep curves as in fig. 4.22 differ not only because of inertio–elastic oscillations from the predictions in the previous sections. For a

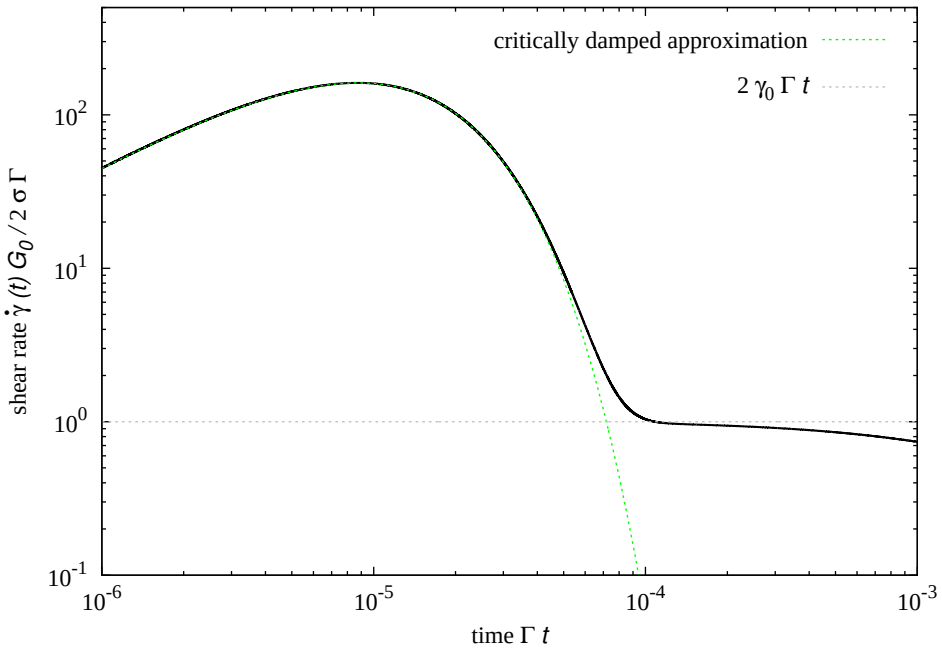

Figure 4.21.: Creep shear rate, $\dot{\gamma}(t)$, rescaled by $2\sigma\Gamma/\gamma_0$, compared to the constant shear rate prediction, $2\gamma_0\Gamma t$, (dashed gray line) and to the prediction for a critically damped system with constant modulus, $\frac{\gamma_0 G_0}{a} e^{-\sqrt{\frac{G_0}{a}}t} t$, (dashed green line).

glassy creep curve, it is expected from the perspective of the schematic model, that the creep curve stays on a plateau for asymptotically long times. In contrast, the measurements on thermosensitive microgels show an anomalous creep.

Before imposing a constant shear stress in the experiments, a preshear with constant shear rate was applied followed by a waiting time, t_w. Other experiments [60] and simulations [66] confirm that the onset of flow depends on the waiting time, although the simulation, in difference to the experiment, considers the waiting time since a temperature quench and the authors of ref. [60] performed oscillatory preshear. However at large waiting times, $t_w = 6000s$, as in fig. 4.22, the aging–dependence should converge. This is reflected by the almost vanishing deviations between the resulting shear rates for the smallest imposed shear stress, $\sigma R^3/k_B T = 0.1$, for the two larges waiting times, $t_w = 3600$, and $t_w = 6000s$.

The anomalous creep occurring in the long–time limit for the smallest imposed shear stress in the experiment on colloidal glasses could be connected to an activated process, as discussed in ref. [30]. An asymptotic power law for the shear rate, $\dot{\gamma} \propto t^{-1+x}$, can be understood as a slow decay of the shear modulus from the plateau, $-t^x$, in lowest order analogously to the result of eq. (4.57). This slow dissipative would occur in the linear loss modulus as power law, decreasing $\propto \omega^{-x}$, eq. (2.139). As shown in fig. 4.23, the long–time asymptote of the

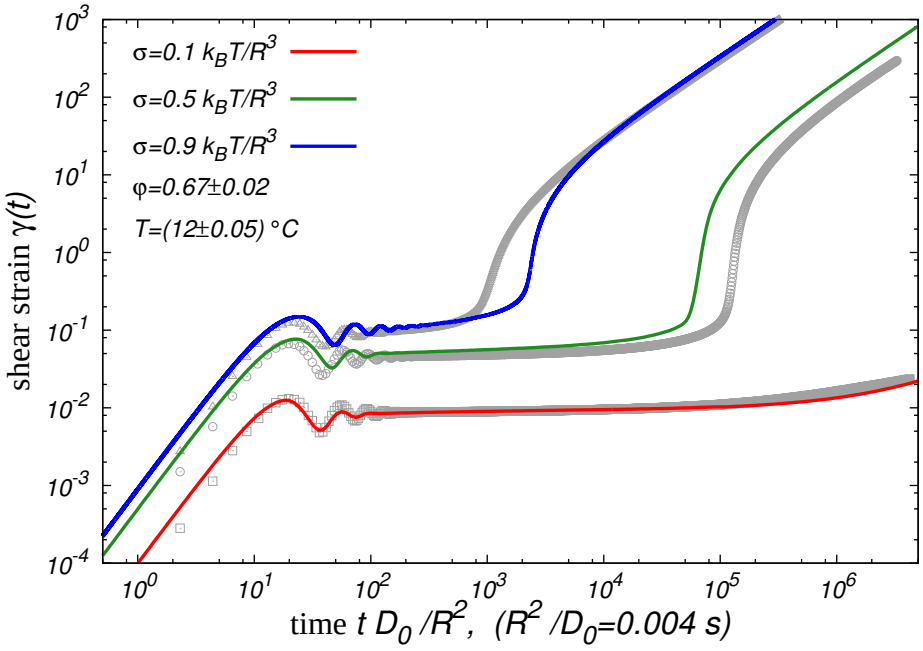

Figure 4.22.: Creep curves, $\gamma(t)$, measured in a stress controlled experiment for three different stress steps, σ, after the waiting time, $t_w = 6000s$, [50] (gray symbols) and the corresponding fits from the schematic model with fit parameters as in tab. 4.2 (colored lines).

anomalous creep for the lowest imposed stress in fig. 4.22 can be approximated via nonlinear fitting without the first 500 data points, the resulting power law is,

$$\dot{\gamma}(t)\tau_0 \approx 7.07 \cdot 10^{-6}(t/\tau_0)^{-0.553}. \tag{4.76}$$

Analogously, the linear loss modulus should exhibit a power law for small frequencies with the exponent, $0.553 - 1$,

$$G''(\omega) \propto \omega^{-0.443}. \tag{4.77}$$

Previous experiments on the same material have shown a slow dissipative process for small frequencies in the glassy regime [30].

Although this agreement might support an interpretation of an additional slow dissipative process in the glass, that determines the long–time dynamics, the variation of the fit parameter for additional dissipative processes, tab. 4.2, indicates more complex dynamics in the glass under stress.

As the schematic model is based on MCT–ITT, it describes homogeneous, incompressible flows. Hence, it can be understood as a benchmark to distinguish the onset of homoge-

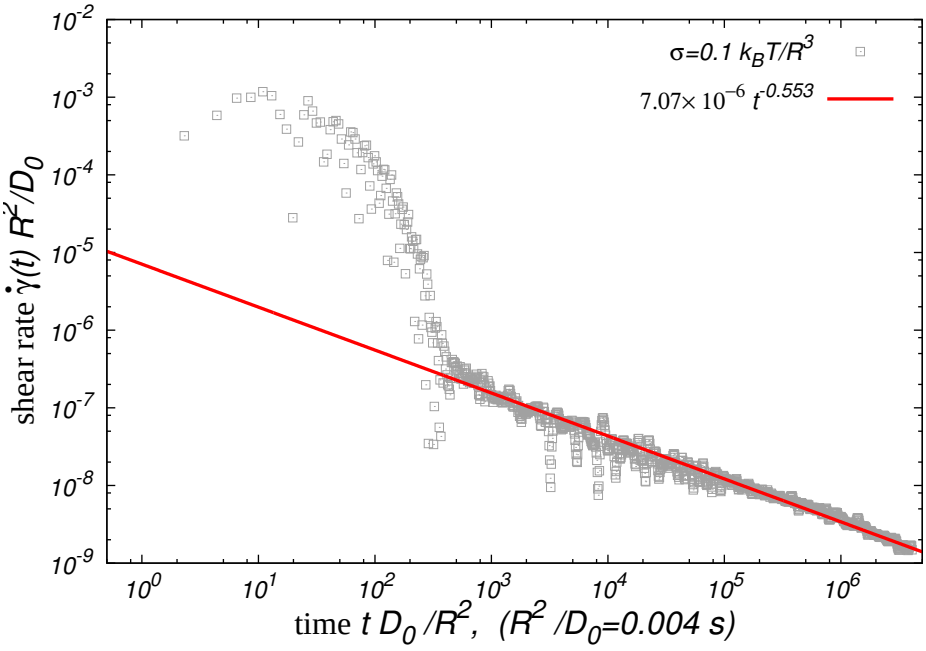

Figure 4.23.: Fit (red line) to creep shear rate, $\dot{\gamma}(t)$, measured in a stress controlled experiment for the largest waiting time, $t_w = 6000s$ [50] (gray symbols).

neous and heterogeneous flows. In ref. [50], the shear rate response for an imposed stress, $\sigma R^3/k_BT = 0.5$, after the waiting time, $t_w = 3600s$, shows a prominent S–shape. In experiments on carbopol microgels [67], the onset could be analyzed with local velocimetry. In a similarly S–shaped strain rate curve, the onset of flow is initiated by a fail at the walls followed by total wall slip. Shear banding gradually establishes a linear velocity profile again, which remains linear for the steady state. The same evolution for velocity profiles was found again for carbon black colloidal gels [68]. All three experiments used the same stress–controlled rheometer.

For colloidal glasses, numerical simulations [66] show for the onset of flow heterogeneous local mobilities, as well as shear banding after longer aging times, which the authors connect explicitly with the waiting–time dependence of the results in ref. [50]. The velocity profiles of the simulation [66] display transient heterogeneities.

In soft–glass rheology [69], transient shear–banding is also found during tertiary creep.

The discussion of the heterogeneous flow during tertiary creep is related to the discussion of shear–banding for steady shear in the time interval between the occurrence of an overshoot and the onset of the steady state.

MCT explains both phenomena with a mechanism that agrees with homogeneous flow, and at least for the stress overshoots in steady shear, the existence of homogeneous flow has been confirmed by both Brownian–dynamics (BD) simulations [70] and molecular dynamics (MD)

simulations [33].

The Percus–Yevick structure factor for hard–spheres [20] is crucial to the yielding transition of the schematic model. The question remains thereby open, how a non–vanishing softness of the core shell microgel particles might influence the onset of the flow and the asymptotic creep. In the memory kernel of the model which I used to compute the creep curves in this chapter, eq. (2.113), I set the functions, h_1 and h_3, to one in accordance with the models used for steady shear. At a strain of about $\gamma \approx 1\%$, roughly the strain scale of the creep curve for the smallest imposed stress in fig. 4.22, the function, h_1, can be treated like a constant close to one, that barely varies in time. The time–dependence of the function, h_3, and the resulting influence on the creep curves has not been studied yet.

It remains a subject to further research, if the inversion of the constitutive equation, eq. (4.7), has unique solutions. As described in the appendix, sec. A.1, I use a one–sided iteration scheme, which ensures that I find the largest attractor of the iteration for the transient density correlator, $\phi(t, t')$. Through the numerical inversion, this algorithm finds the smallest possible solution for the creep strain, $\gamma(t)$. If larger solutions, i.e. faster increasing solutions, exist, the algorithm does not find them.

σ	ε	G_0	Γ	γ_c	γ^*	γ^{**}	δ
0.1	10^{-6}	125	130	0.85	0.08	0.086	5×10^{-8}
0.5	10^{-6}	125	130	0.85	0.1	0.107	5×10^{-7}
0.9	10^{-6}	125	130	0.85	0.17	0.192	6×10^{-7}

Table 4.2.: $F_{12}^{(\dot\gamma)}$–parameters used in the MCT computations for this section.

4.7. Stress ramps

4.7.1. Instantaneous response

For a stress ramp, i.e. the applied stress rises linearly in time, $\sigma(t) \propto t$, one observes for small times, i.e. $t \ll 1/\Gamma$, an initial shear rate of,

$$\dot\gamma_0 = \frac{\dot\sigma}{G_0}. \tag{4.78}$$

When the short–time decay of the generalized shear modulus sets on,

$$G(t - t') \approx G_0 \exp\left(-2\Gamma t\right), \tag{4.79}$$

the shear rate response will increase linearly and the strain will increase quadratically in

time,

$$\dot{\gamma}(t) = \frac{\dot{\sigma}}{G_0}\,(1 + 2\Gamma t)\,, \tag{4.80}$$

$$\gamma(t) = \frac{\sigma(t)}{G_0} + 2\Gamma\dot{\gamma}_0 t^2. \tag{4.81}$$

Fig. 4.24 shows the shear rate response to stress ramps compared to the prediction from eq. 4.80.

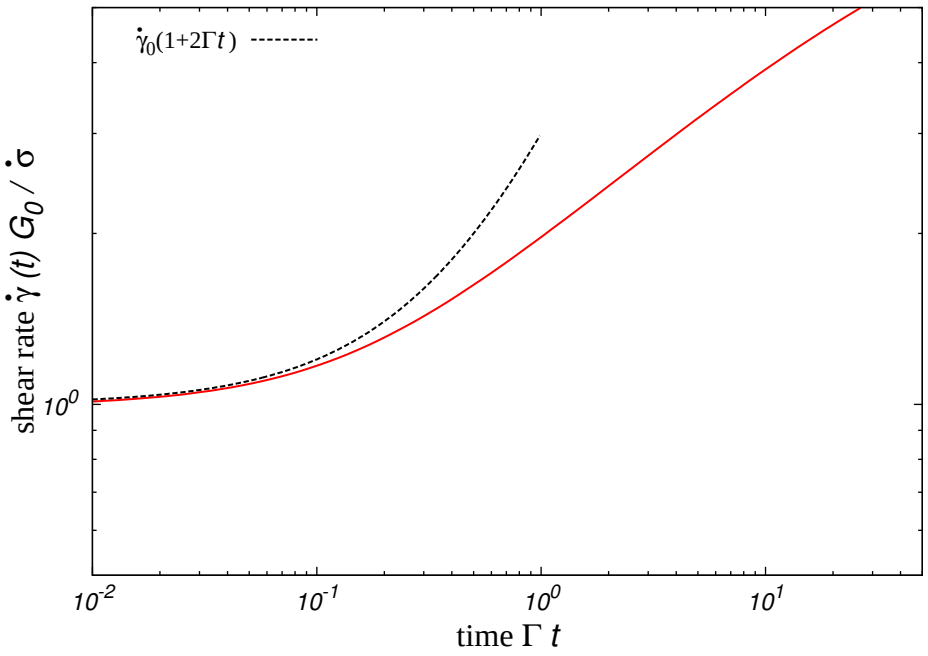

Figure 4.24.: Shear rate response, $\dot{\gamma}(t)$,rescaled by the instantaneous shear rate of eq. (4.78),as a function of rescaled time, Γt, for a stress ramp, $\dot{\sigma} = 10^{-10}$, separation parameter, $\varepsilon = 2 \times 10^{-7}$, and the other parameters as in tab. 4.1 (full red line) and the short–time approximation from eq. (4.80) (dashed black line).

4.7.2. β–process

In the following analysis, I assume that the strain, $\gamma(t)$, will be small compared to the scales of the strain–induced decay of the modulus and the density correlator,

$$\gamma(t) \ll \gamma_* \qquad \text{and} \qquad \gamma(t) \ll \gamma_c. \tag{4.82}$$

This ensures that I am approximately in the regime of linear response.

Due to the fast β–process, the generalized shear modulus decays onto its plateau value,

$$G(t-t') \approx G_\infty + 2(1-f_c)^2 f_c \left(\frac{t}{t_0}\right)^a + \mathcal{O}(t^{2a}). \tag{4.83}$$

Similar analysis as in sec. 4.3 yields an asymptotic shear rate predefined by the β–process. Eq. (4.23) is solved for an linearly increasing stress, $\sigma(t) = \dot{\sigma}t$, by the shear rate,

$$\dot{\gamma}(t) \approx \frac{\dot{\gamma}_0}{f_c^2} \mathcal{L}^{-1}\left[\frac{z^{-1}}{1+\frac{2\Gamma(1-a)t_0^a}{f_c} z^a}\right] \tag{4.84}$$

$$= \frac{\dot{\gamma}_0}{f_c^2} \mathcal{L}^{-1}\left[z^{-1}\sum_{n=0}^{\infty}\left(-\frac{2\Gamma(1-a)t_0^a}{f_c} z^a\right)^n\right] \tag{4.85}$$

$$= \frac{\dot{\gamma}_0}{f_c^2}\left(\sum_{n=0}^{\infty}\left(-\frac{2t_0^a\Gamma\left(1-a\right)}{f_c}\right)^n \frac{t^{-na}}{\Gamma(1-na)}\right). \tag{4.86}$$

The shear rate is increased to a plateau value at the same time, the generalized shear modulus reaches its plateau,

$$\dot{\gamma}(t) = \frac{\dot{\sigma}}{G_\infty}\left(1 - \frac{2f_c(1-f_c)^2 t_0^a}{f_c^3} t^{-a} + \mathcal{O}(t^{-2a})\right), \tag{4.87}$$

which means that the strain response approaches a linear increase,

$$\gamma(t) = \frac{\sigma(t)}{G_\infty} - \frac{2\dot{\gamma}_0(1-f_c)^2 t_0^a}{f_c(1-a)} t^{1-a} + \mathcal{O}(t^{1-2a}), \tag{4.88}$$

At the glass transition, the shear rate plateau is in zeroth order,

$$\dot{\gamma}_{\mathrm{pl}} = \frac{\dot{\sigma}}{G_\infty} = \frac{\dot{\sigma}}{G_0 f_c^2} = \frac{\dot{\gamma}_0}{f_c^2}. \tag{4.89}$$

The plateau shear rate, $\dot{\gamma}_{\mathrm{pl}}$, depends on the separation parameter, ε, analogously as the plateau strain in sec. 4.3,

$$\dot{\gamma}_{\mathrm{pl}}(\varepsilon) = \frac{\dot{\sigma}}{G_\infty(\varepsilon)} = \frac{\dot{\sigma}}{G_0\left(f_c + \lambda^2\sqrt{\frac{\varepsilon}{1-\lambda}} + \mathcal{O}(\varepsilon)\right)^2}. \tag{4.90}$$

In the fluid regime, the generalized shear modulus will decay from the plateau at times close to the α–decay time, τ_α,

$$G(t-t') = G_\infty - 2(1-f_c)^2 f_c \left(\frac{t}{\tau_\alpha}\right)^b + \mathcal{O}(t^{2a}). \tag{4.91}$$

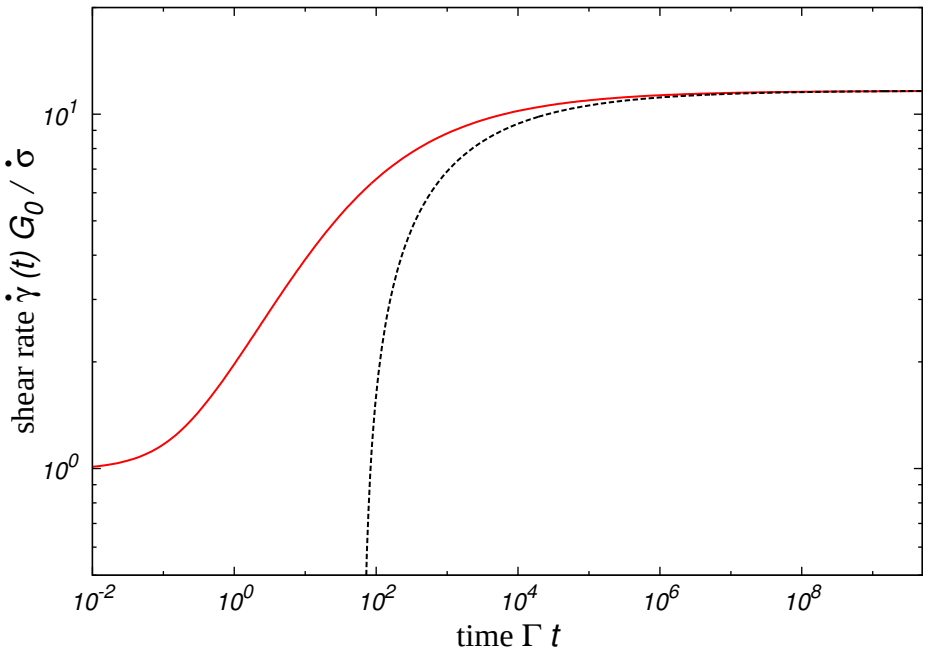

Figure 4.25.: Shear–rate response, $\dot{\gamma}(t)$, rescaled by the instantaneous shear rate, as a function of rescaled time, Γt, for a stress ramp, $\dot{\sigma} = 10^{-10}$, separation parameter, $\varepsilon = 2 \times 10^{-7}$, and the other parameters as in tab. 4.1 (full red line) and the approximated result from eq. (4.87) (dashed black line).

This will result in the shear rate increasing faster than linearly,

$$\dot{\gamma}(t) = \frac{\dot{\sigma}}{G_\infty} \left(1 + \frac{2 f_c (1 - f_c)^2 \tau_\alpha^{-b}}{f_c^3} t^b + \mathcal{O}(t^{2b}) \right). \tag{4.92}$$

For longer times the decay of the α–process might be fitted by a Kohlrausch law. For the longest times, an exponential decay might be a good choice for a fit, as it is indicated by the agreement for small frequencies in fig. 2.4. An exponential decaying shear modulus,

$$G(t - t') = G_\infty \exp\left(-2\tilde{\alpha} \frac{t}{\tau_\alpha} \right), \tag{4.93}$$

causes the shear rate to increase linearly and the strain to increase quadratically in time,

$$\dot{\gamma}(t) = \frac{\dot{\sigma}}{G_\infty} \left(1 + \tilde{\alpha} \frac{t}{\tau_\alpha} \right), \tag{4.94}$$

$$\gamma(t) = \frac{\sigma(t)}{G_\infty} + \frac{\dot{\sigma}}{G_\infty} \tilde{\alpha} \frac{t^2}{2\tau_\alpha}. \tag{4.95}$$

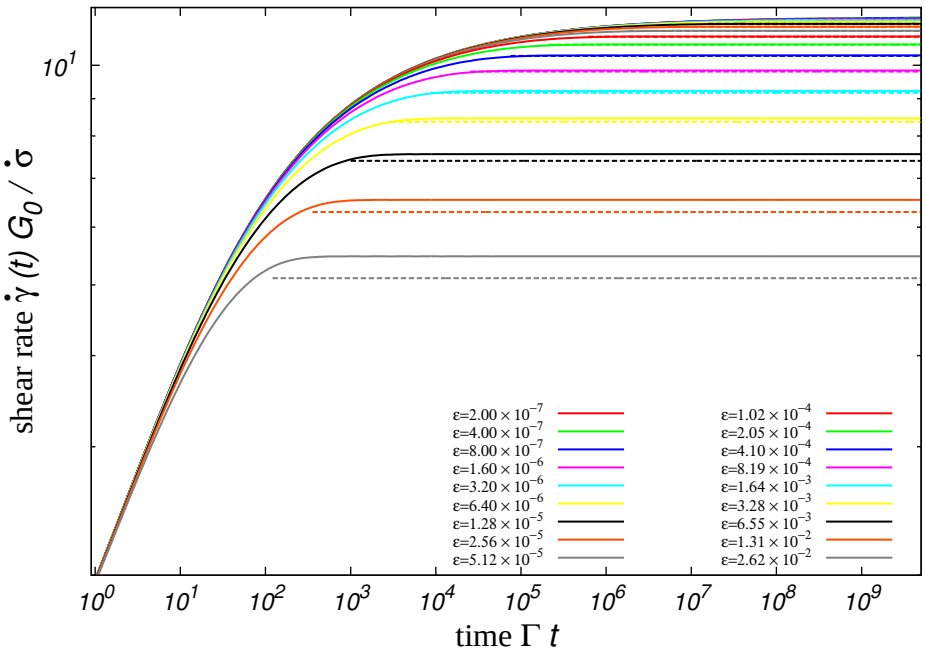

Figure 4.26.: Shear–rate response, $\dot{\gamma}(t)$, rescaled by the instantaneous shear rate, for a stress ramp, $\dot{\sigma} = 10^{-10}$, various separation parameters, $\varepsilon > 0$, and the other parameters as in tab. 4.1 (full lines) and the corresponding plateau shear rate predicted from eq. 4.90 (dashed lines).

The result of the strain increasing quadratically in time is only observable, if the approximation of linear response holds. This requires a stress rate so small, that at time, τ_α, the strain has not reached the scale of the yield strain, which can be estimated as,

$$\dot{\sigma} \ll \frac{\gamma_y G_\infty}{\tau_\alpha}. \tag{4.96}$$

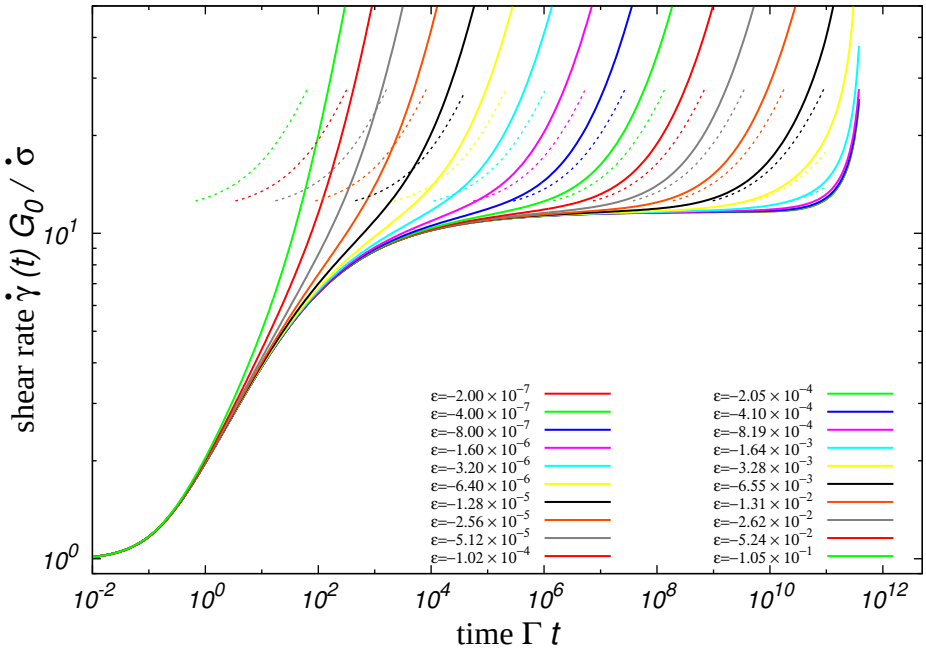

Figure 4.27.: Shear–rate response, $\dot{\gamma}(t)$, rescaled by the instantaneous shear rate for a stress ramp, $\dot{\sigma} = 10^{-10}$, ,various separation parameters, $\varepsilon < 0$, and the other parameters as in tab. 4.1 (full lines) and the corresponding shear rate increase predicted from eq. 4.92 (dashed lines).

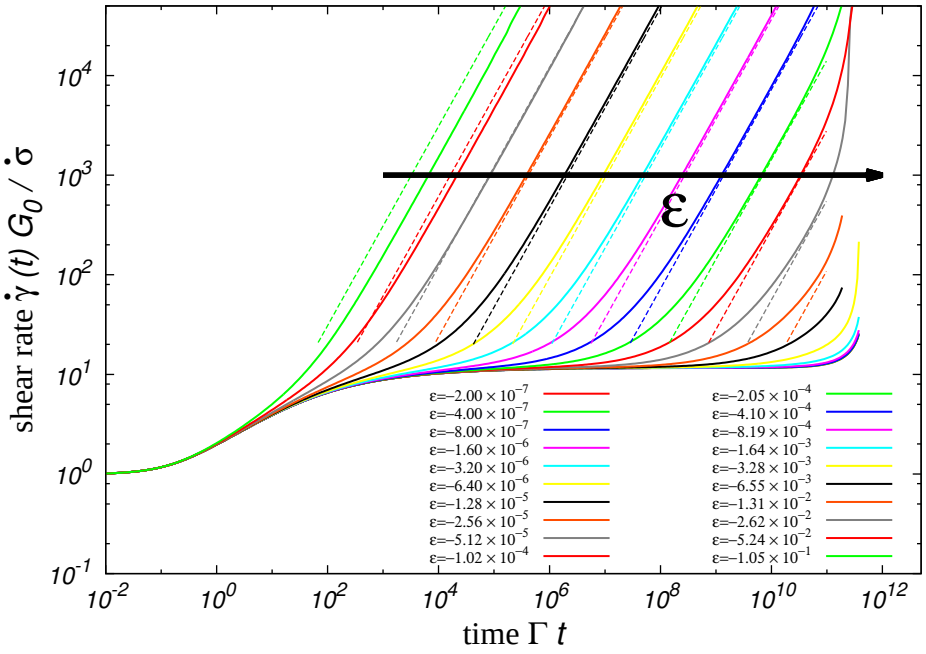

Figure 4.28.: Shear–rate response, $\dot{\gamma}(t)$, rescaled by the instantaneous shear rate for a stress ramp, $\dot{\sigma} = 10^{-10}$, various separation parameters, $\varepsilon < 0$, and the other parameters as in tab. 4.1 (full lines) and the corresponding linear shear rate increase predicted from eq. 4.94 (dashed lines).

4.7.3. Yielding

For stress ramps with a stress rate larger than the threshold given in eq. (4.96), the onset of a fast increasing strain will be observed, when the yield strain, γ_y, is approached. As the decaying time of the α–process diverges at the glass transition, this observation is expected in the glassy regime, $\varepsilon > 0$, for any finite stress rate. Fig. 4.29 shows, that the onset of superlinear flow is connected to the time scale set by the dynamical yield stress, σ_y, and the stress rate, $\dot{\sigma}$. At the glass transition, i.e. $\varepsilon = 0$, the superlinear flow starts close to a time, $\sigma_y^c/\dot{\sigma}$. For higher packing fractions, $\varepsilon > 0$, the onset of yielding is shifted to later times, as the dynamical yield stress is shifted to higher stress values as well.

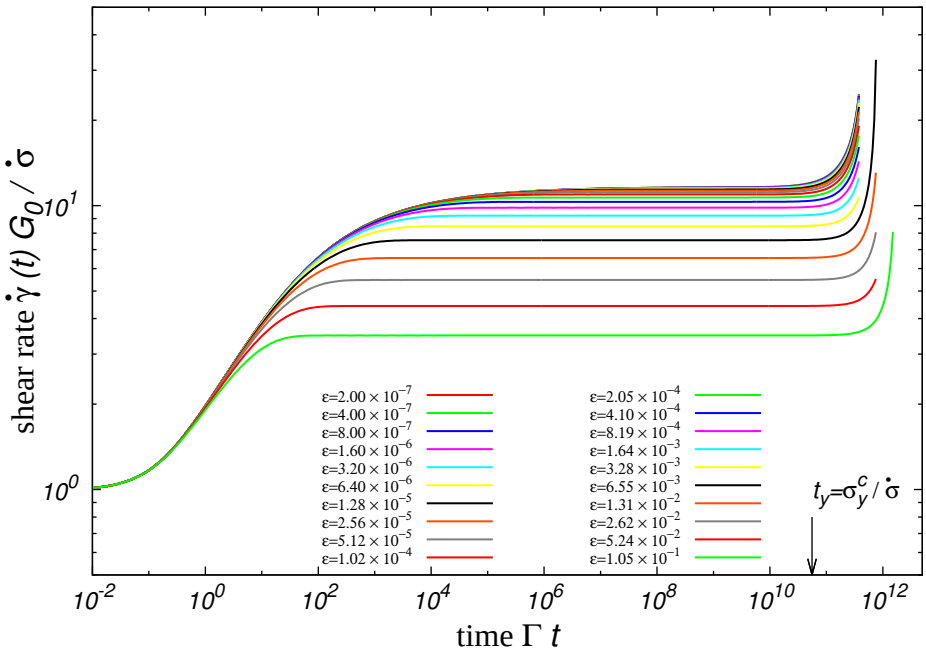

Figure 4.29.: Shear–rate response, $\dot{\gamma}(t)$, rescaled by the instantaneous shear rate, as a function of rescaled time, Γt, for a stress ramp, $\dot{\sigma} = 10^{-10}$, various separation parameters, ε, and the other parameters as in tab. 4.1.

In this chapter, I have discussed the mechanical response under applied stress. I have obtained the creep response, the strain deformation under constant stress, by numerical inversion of a schematic MCT model. Although this method demands a substantial amount of memory and computation time, it has been able to provide results on the numerous time regimes of creep. My analysis of β–scaling has confirmed a relation between the observed increase of the strain and the decay of the generalized shear modulus known from quiescent MCT and the results of ITT–MCT for shear–controlled rheology. This has enabled me to link the various types of increase in the strain response to dissipative processes. Before the onset of the nonlinearity of the response, I can approximately describe the creep response using linear response theory. I have found, that the dynamical yield stress, as known from shear–controlled rheology as steady stress for asymptotically small shear rates, is also a yield stress in stress-controlled rheology. It is the smallest stress, which causes asymptotic flow. I stress–controlled rheology, I can also study stresses below that critical stress value. I have observed a linear response of the glass and its transition to the shear–melted glass, which I can relate to the shear–melted glass known from shear–controlled rheology.

The comparison to the experimental results for a well–studied material, underline the validity of the theoretical approach. Experiments carried out with additional velocimetry, as well as molecular dynamics simulations providing information on the velocities of the single particles put the homogeneity of the yielding flow into perspective. However, the schematic model predicts a mechanism which makes homogeneous yielding possible. Therefore, the contribution of heterogeneities to the process of yielding can be quantified.

The linear increase of the external stress applied onto the material, a stress ramp, has been also studied as a second class of stress–controlled rheology problems. The changes in the constitutive equations link the linear shear–rate response of a stress ramp with the linear strain–response of a stress step, which has confirmed the differentiation between linear and nonlinear response. The nonlinear shear–rate response of the stress ramps differs qualitatively from the nonlinear strain response of stress steps.

5. Conclusion

In this thesis, I have discussed the nonlinear response of glass–forming dispersions under applied time–dependent deformations. This topic provides insight in the dynamics of such materials close to the glass transition. The nonlinear response offers a further comprehension of the glass transition and the nature of the glass. I have described the process of yielding as a transition from the anelastic stress response to plastic flow and as a transition from a deformed to a shear–melted glass. The schematic MCT model, which I have used to describe the response to time–dependent shear flow and to applied stress, gives the transient time–dependence of the response. By omitting the wave–vector dependence, I have lost structural information. I can interpret the structural dynamics only in the context of the microscopic MCT theory, by relating the density correlation function of the schematic model to the corresponding correlation functions of the microscopic theory.

By an instantaneous change of direction of the imposed shear flow, I have studied the history–dependent response of materials in proximity of the glass transition. In equilibrium physics, a change in the observables can be explained by a change of the variables defining each state. The schematic MCT model obtains a nonequilibrium observable by taking the whole deformation history into account, based on the ITT–MCT approach [10].

Using this history–dependence of the response to a shear reversal, I have probed the dynamics at the time of the reversal. I have rationalized the phenomena of residual strains, decreased overshoots and a softer apparent elasticity as results of stress contributions of the preshear, the shear flow before the reversal of its direction. By systematic computations of the quantifying observables of these phenomena for preshear strains from zero to one, I have discussed the effect of the yielding transition on the preshear dependence. This discussion is consistent, with the interpretation of the yielding as the transition from a (mostly) reversible anelastic regime to the steady state of irreversible flow.

The density–dependence of the elasticity of the quiescent glass and the shear–rate dependence of transient stress overshoots and steady states persists in the results for a shear–flow reversal. I have traced the scaling with the separation parameter, that corresponds to a relative density, back to the scaling of the nonergodicity parameter.

Using the numerical inversion of the schematic MCT model, I have computed the strain response under applied constant stress, known as creep. The inversion simplifies the analysis of the relation between strain–controlled and stress–controlled rheology. In the linear response regime, for both stress steps and stress ramps, I have connected every increase of the strain

to a known dissipative process in the glass. The onset of the nonlinear response depends in my computations on the same mechanisms related to the yielding of a glass under steady shear.

I can rule out for the schematic MCT model, that asymptotic flow is caused by an applied stress smaller than the dynamical yield stress. Any applied stress larger than the yield stress results in asymptotic flow. I have introduced a schematic overview, which separates glassy from fluid dynamics and linear from nonlinear response. The yielding transition is connected to the transition from linear to nonlinear response of the glass.

The results for the stress response after a shear–flow reversal and for strain response under applied stress show new aspects on the onset of nonlinear response. Stress and stain response can be described by the same fundamental principles. In this work, the process of homogeneous yielding is attributed to a collective cage breaking of neighboring particles, represented in ITT–MCT by a dephasing of the derivatives of the static structure factor [41].

To advance the discussion of the transient time dependence of yielding, the underlying structural mechanisms should be studied in the microscopic MCT and in Brownian dynamics simulations.

5.1. Zusammenfassung

In der vorliegenden Arbeit habe ich das nichtlineare Antwortverhalten von glasbildenden Dispersionen unter zeitabhängigen Verformungen erläutert. Es bietet Einsicht in die Dynamik solcher Materialien nahe am Glasübergang und ein tiefer gehendes Verständnis des Glasübergangs und der Natur des Glases. Ich habe die Fließgrenze als Punkt eines Übergangs von einer anelastischen Spannungsantwort zum plastischen Fließen, und als Punkt eines Übergangs von einem verformten zu einem schergeschmolzenen Glas beschrieben. Das schematische Modell der Modenkopplungstheorie, das ich verwendet habe um die Reaktion auf zeitabhängige Scherflüsse und auf konstante Spannungen zu beschreiben, liefert die transiente Zeitabhängigkeit der Antwort. Durch das Weglassen der Wellenvektorabhängigkeit, habe ich Strukturinformationen verloren. Ich kann die Strukturdynamik nur im Rahmen der mikroskopischer MCT im Verhältnis des Dichtekorrelationsfunktion des schematischen Modells und der entsprechenden Korrelationsfunktionen der mikroskopischen Theorie interpretieren.

Mit einer abrupten Richtungsänderung des aufgeprägten Scherflusses, habe ich die vorgeschichtsabhängige Reaktion der Materialien in der Nähe des Glasübergangs untersucht. In der Gleichgewichtsphysik kann eine Änderung einer Observablen durch eine Änderung der Zustandsvariablen erklärt werden. Das schematische MCT–Modell erhält eine Nichtgleichgewichts–Observable, indem die gesamten Deformationsgeschichte berücksichtigt wird, basierend auf dem ITT–MCT–Ansatz. [10].

Mit dieser Vorgeschichtsabhängigkeit der Reaktion auf eine Scherflussumkehr, habe ich die Dynamik zum Zeitpunkt der Umkehrung untersucht. Ich habe die Phänomene der Restdeh-

nung, verringerten Spannungsüberschwingern und eine weichere scheinbare Elastizität als Ergebnisse der Spannungbeiträge des Vorscherens, des Scherflusses vor der Richtungsänderung, begründet. Durch systematische Berechnungen der Größen dieser Phänomene für Vorscherdehnungen von null bis eins, habe ich die Wirkung der Fließgrenze auf die Vorscherabhängigkeit diskutiert. Diese Darstellung ist konsistent mit der Interpretation der Fließgrenze als Übergang von einem Regime überwiegend reversibler, anelastischer Verformung zu dem stationären Zustand irreversiblen Flusses.

Die Dichteabhängigkeit der Elastizität des ruhenden Glases und der Schergeschwindigkeitsabhängigkeit der transienten Spannungsüberschwinger und der stationären Zustände setzt sich in den Ergebnissen für eine Scherflussumkehr fort. Ich habe die Skalierung mit dem Separationsparameter, der einer relative Dichte entspricht, auf die Skalierung des Nichtergodizitätsparameters zurückgeführt.

Mithilfe der numerischen Inversion des schematischen MCT–Modells habe ich die Dehnungsantwort unter einer konstanten Spannung berechnet, die man als Kriechen bezeichnet. Die numerische Inversion vereinfacht die Analyse der Beziehung zwischen der dehnungs– und spannungsgesteuerten Rheologie. Im Linearen–Antwort–Regime, sowohl für Spannungsstufen als auch Spannungsrampen, konnte ich für jeden Anstieg der Dehnungsverformung die Beziehung zu einem bekannten dissipativen Prozess im Glas herstellen. Das Auftreten der nichtlinearen Antwort hängt in meinen Berechnungen mit den gleichen Mechanismen zusammen, die in Beziehung zu dem Übergang an der Fließgrenze eines stetig gescherten Glases stehen.

Für das schematische MCT–Modell kann ich ausschließen, dass Spannungen unterhalb der Fließgrenze asymptotischen Fluss generieren. Jede Spannung oberhalb der Fließgrenze wiederum erzeugt einen asymptotischen Fluss. Ich habe einen schematischen Überblick vorgestellt, bei dem ich zwischen glasartiger und fluider Dynamik und zwischen linear und nichtlinearer Antwort unterscheide. Die Fließgrenze ist eng verbunden mit dem Übergang von linear zu nichtlinearer Antwort des Glases.

Die Ergebnisse für die Spannungsantwort nach Scherflussumkehr und für die Dehnungsantwort bei einer angelegten äußeren Spannung zeigen neue Aspekte des Einsetzens der Nichtlinearität. Spannungs– und Dehnungsantwort können mit den gleichen fundamentalen Prinzipien beschrieben werden. In dieser Arbeit wird der Fließübergang dem kollektiven Brechen der Käfige, die aus den benachbarten Teilchen gebildet werden, zugeordnet. Im ITT–MCT–Ansatz wird dies durch eine Phasenverschiebung der Ableitungen der statischen Strukturfaktoren dargestellt [41].

Um die Diskussion der transienten Zeitabhängigkeit voranzubringen, sollten die zugrunde liegenden strukturellen Mechanismen mithilfe der mikroskopischen MCT und Brownsche–Dynamik–Simulationen untersucht werden.

A. Numerical details

A.1. Two–time algorithm for MCT

The numerical algorithm to solve the schematic model as defined in sec.2.4, follows the the algorithm developed by J. Brader and Th. Voigtmann.

The time is discretized in equidistant time steps, Δt, so that the time, $t = i \cdot \Delta t$, can be denoted with the index i. The transient density correlator, $\phi(t, t')$, is discretized as $\phi_{i,j}$ with one index for each time argument. The derivative in eq.(2.110), $\frac{1}{\Gamma}\partial_t \phi(t, t')$, is discretized in the following way

$$\frac{1}{\Gamma \Delta t}\left(\frac{3}{2}\phi_{i,j} - 2\phi_{i-1,j} + \frac{1}{2}\phi_{i-2,j}\right), \tag{A.1}$$

which is a three point backwards derivative of the interpolating Lagrange polynomial. The memory integral, $\int_{t'}^{t} \mathrm{d}t'' m(t, t'', t')\partial_{t'}\phi(t'', t')$, is written as a sum,

$$\sum_{k=j}^{i} m_{i,k} \cdot (\phi_{k,j} - \phi_{k-1,j}), \tag{A.2}$$

which requires a definition of the correlator $\phi_{j-1,j}$. Causality restricts the transient density correlator, $\phi(t, t')$, to the time domain of $t \geq t'$. The occurrence of $\phi_{j-1,j}$ is only caused formally to compute the numerical derivative, $\partial_{t''}\phi(t'', t')|_{t''=t'}$, still included in the causal part of the (t', t'')–time plane. Numerically this derivative is obtained by setting the respective correlator to one, $\phi_{j-1,j} = \hat{1}$.

The discretized version of eq.(2.110) is then solved for $\phi_{i,j}$, but the memory kernel is explicitly not written as the polynomial in $\phi_{i,j}$. The solution is,

$$\phi_{i,j} = \frac{\left(\hat{1} - \phi_{i,j}\right) m_{i,j} - m_{i,i}\phi_{i-1,j} + \sum_{k=j+1}^{i-1} m_{i,k} \cdot (\phi_{k,j} - \phi_{k-1,j}) + \frac{1}{\Gamma \Delta t}\left(-2\phi_{i-1,j} + \frac{1}{2}\phi_{i-2,j}\right)}{1 + m_{i,i} + \frac{3}{2}\frac{1}{\Gamma \Delta t}}, \tag{A.3}$$

which is more conveniently written with the following abbreviations,

$$A_i = 1 + m_{i,i} + \frac{3}{2}\frac{1}{\Gamma\Delta t}, \tag{A.4}$$

$$B_{i,j} = \hat{1} - \phi_{i,j}, \tag{A.5}$$

$$C_{i,j} = -m_{i,i}\phi_{i-1,j} + \sum_{k=j+1}^{i-1} m_{i,k}\cdot(\phi_{k,j} - \phi_{k-1,j}) + \frac{1}{\Gamma\Delta t}\left(-2\phi_{i-1,j} + \frac{1}{2}\phi_{i-2,j}\right), \tag{A.6}$$

$$\phi_{i,j} = \frac{B_{i,j}m_{i,j} + C_{i,j}}{A_i}. \tag{A.7}$$

The memory kernel, $m_{i,k}$, is in accordance to eq.(2.113)

$$m_{i,k} = h^{(1)}_{i,j}h^{(2)}_{i,k}h^{(3)}_{k,j}(v_1\phi_{i,k} + v_2\phi^2_{i,k}), \tag{A.8}$$

which is actually dependent on the tree time indices i, j, k. $h^{(3)}$ is set to one in all previous applications of this algorithm [49, 38, 39, 40, 33], its role remains to be determined. I chose to set $h^{(1)}$ to one, to keep the algorithm consistent with the one–time parameter dependent equations used for steady shear[29, 71, 30, 31, 37, 72, 32]. If one chooses to keep, $h^{(1)} \neq 1$, it is numerically more convenient and efficient to factorize the memory kernel into $h^{(1)}_{i,j}$ and a two–indices memory kernel $m_{i,k}$.

The density correlators are initialized with $\phi_{i,i} = 1$ and $\phi_{i,i-1} = -\Gamma\Delta t$. $\phi_{i,j}$ is computed in such a scheme, that $A_i, B_{i,j}, C_{i,j}$ are well defined by computing all the quantities, they depend on, before. This requires to compute all $\phi_{x,j}$ with $j \leq x < i$ and all $m_{i,y}$ with $j < y \leq i$ before $\phi_{i,j}$.

As $m_{i,j}$ depends on $\phi_{i,j}$ the equations are not closed. Theoretically this could be done by solving the quadratic equation, but the root, that one needs to take for solving a quadratic equation, has a symmetric error. The solution of eq.(2.110) is defined to be the largest attractor, if there exists more than one[18]. The solution of the quadratic discretized equation might lead to a numerical solution for $\phi_{i,j}$, smaller than the exact solution. As the correlators at larger times depend numerically on $\phi_{i,j}$, this triggers a fast decay to zero of the numerical solution for the correlator which will deviate significantly from the exact solution.

In order to avoid this bug, one has to make sure, that the numerical solution stays greater or equal than the exact solution during the whole computation. Therefore an one sided iteration scheme is used, which computes the memory kernel $m^{(0)}_{i,j}$ with an initial value $\phi^{(0)}_{i,j}$. The choice of $\phi^{(0)}_{i,j} = 1$ ensures, that the value fulfills the requirement, $\phi^{(0)}_{i,j} \geq \phi(t,t')$. For monotonously decreasing time–correlation functions, $\phi^{(0)}_{i,j} = \phi_{i,j+1}$ is a more efficient initial value. As this thesis considers non–monotonic strains, the first choice is the one to be made. In the following iterations, $\phi^{(n)}_{i,j}$ is computed with $m^{(n-1)}_{i,j}$, until the relative change $\frac{\phi^{(n)}_{i,j} - \phi^{(n-1)}_{i,j}}{\phi^{(n)}_{i,j}}$ is smaller than a chosen level of accuracy.

Every N time steps, the width Δt of the time steps is doubled. To operate on an equidistant

grid and keep the amount of allocated memory constant, the solutions of $\phi_{i,j}^{\Delta t}$ computed with the step width Δt are saved on a hard drive and the algorithm maps $\frac{1}{2}\left(\phi_{2i,j}^{(\Delta t)} + \phi_{2i+1,j}^{(\Delta t)}\right) \mapsto \phi_{i,j}^{(2\Delta t)}$. As a result, the density correlator is known for the first $\frac{N}{2}$ time steps of the new grid with step width $2\Delta t$. For the numerical inversion, the strain γ_i and the shear rate $\dot{\gamma}_i$ have to be mapped analogously.

A.2. Brent's method

To find a solution for the equation

$$f(\dot{\gamma}(t)) = \sigma(t) - \int_0^t dt'\, \dot{\gamma}(t') G(t,t') = 0, \tag{A.9}$$

Brent's method [73] is numerically applied.

This method requires a given interval, in which the solution, viz. the root of the given function, $f(\dot{\gamma}(t))$, is searched for. Starting with the shear rate at the previous time step, $\dot{\gamma}(t-\Delta t)$, the shear rate is increased in steps of 1 percent of this value, $0.01 \cdot \dot{\gamma}(t-\Delta t)$, until a shear rate, $\dot{\gamma}^+$, is obtained, for which the value of the function, $f(\dot{\gamma}^+)$, is positive. Analogously, starting from the same value the shear rate, $\dot{\gamma}^-$, is decreased in steps of the same magnitude, until the value of the function, $f(\dot{\gamma}^-)$, has a negative value.

Two competing objectives have to be balanced. I want the interval being found in a small number of steps, as each step in the shear rate includes a complete time step in the computation of the shear stress as described in the previous section. On the other hand, I want a small interval around the expected solution. A larger interval might cause the algorithm to fail, as the resulting shear modulus might be computed as zero, when the amplitude of the shear rate is set to a too large value, $|\dot{\gamma}| \gg 1$. An adaptive method, that searches the interval based upon the value of the previous time step, seems to be favorable to meet this dilemma. The choice of the step size as 1 percent of the value of the shear rate at the previous time step, $\dot{\gamma}(t-\Delta t)$, is a guess and could be improved under the constraints of the described objectives.

Having established the interval, $[\dot{\gamma}_-, \dot{\gamma}^+]$, and the initial estimate, $\dot{\gamma}_0 = \dot{\gamma}(t-\Delta t)$, for the shear rate, $\dot{\gamma}(t)$, the prerequisites for Brent's method are met.

If the values of the term, $f = \sigma(t) - \int_0^t dt'\, \dot{\gamma}(t') G(t,t')$, for the estimated shear rate, $\dot{\gamma}_i$, is unequal to the values, f_-, f_+, obtained for the lower and the upper boundary, $\dot{\gamma}_-, \dot{\gamma}^+$, an inverse quadratic interpolation is performed. Otherwise, instead of the inverse quadratic interpolation, the secant method is used. The result of the interpolation step, $\dot{\gamma}_{i+1}$, is only accepted, when it is in the interval, $\left[\frac{3\dot{\gamma}_- + \dot{\gamma}_+}{4}, \dot{\gamma}_+\right]$. Also the change, $|\dot{\gamma}_i - \dot{\gamma}_{i-1}|$, between the two previous iteration steps must exceed a predefined threshold of tolerance. The change of

the current iteration step should not exceed half of the change in the previous iteration step, $|\dot{\gamma}_{i+1} - \dot{\gamma}_i| < \frac{1}{2}|\dot{\gamma}_i - \dot{\gamma}_{i-1}|$. Otherwise a bisection step, $\dot{\gamma}_{i+1} = \frac{\dot{\gamma}_- + \dot{\gamma}_+}{2}$, is performed. If the previous iteration step was an interpolation step, the change between the previous iteration step and the iteration step before, $|\dot{\gamma}_{i-1} - \dot{\gamma}_{i-2}|$, and $\frac{1}{2}|\dot{\gamma}_{i-1} - \dot{\gamma}_{i-2}|$, are compared respectively.

This method ensures, that it does not run much slower than the bisection method. It requires less or equal then the number of the steps required by the bisection method squared [73], $N_{\text{Brent}} \leq N^2_{\text{bisection}}$. This estimate regards only the worst–case scenario. For well–behaved functions, it converges superlinearly with the inverse quadratic interpolation. Therefore, this method is fast for stresses, $|\frac{\sigma - \sigma_y}{\sigma}| \gg 1$, and strains, $|\frac{\gamma - \gamma_*}{\gamma}| \gg 1$, and it remains robust for stresses, $\sigma \approx \sigma_y$ and strains, $\gamma \approx \gamma_*$.

B. Mathematical techniques

B.1. Laplace Transform

In this thesis, I use the following convention for the Laplace transform, $\mathcal{LT}\left[f(t)\right](z)$, of a function, $f(t)$, defined on the time domain, $t \in [0, \infty[$,

$$\mathcal{LT}\left[f(t)\right](z) = \hat{f}(z) = \int_0^\infty \mathrm{d}t\; e^{-zt} f(t), \tag{B.1}$$

with z as a complex number.

In sec.2.4.2, the Laplace transform is used with $z = i\omega$. The dynamic moduli are given as the real and imaginary part of the Laplace transform of the derivative of the generalized modulus. Taking the time derivative corresponds to a multiplication with $i\omega$ in Laplace space.

For the results in this thesis the Laplace transform of a function, which describes the decay onto or from a constant value, is of major interest,

$$f(t) = c_0 + c_1 t^x, \tag{B.2}$$

with x, any real number but a negative integer, $x \in \mathbb{R}\backslash\mathbb{Z}_{<0}$.

Its Laplace transform can be easily obtained, as the Laplace transformation is a linear transformation,

$$\begin{aligned}
\mathcal{LT}\left[f(t)\right](z) =& \mathcal{LT}\left[c_0 + c_1 t^x\right](z) && \text{(B.3)}\\
=& \mathcal{LT}\left[c_0\right](z) + c_1 \mathcal{LT}\left[t^x\right](z) && \text{(B.4)}\\
=& \frac{c_0}{z} + c_1 \frac{\Gamma(1+x)}{z^{1+x}}. && \text{(B.5)}
\end{aligned}$$

The convolution theorem states, that the Laplace transform of a convolution, $\int_0^t \mathrm{d}t'\; f(t')g(t-t')$, is given as the product of the Laplace transforms of each

function,

$$\mathcal{LT}\left[\int_0^t \mathrm{d}t'\ f(t')g(t-t')\right](z) = \mathcal{LT}\left[f(t)\right](z)\mathcal{LT}\left[g(t)\right](z). \tag{B.6}$$

I can find the asymptotic behaviour of a function, $f(t)$, via its Laplace transform, as for the asymptotic of a function, $f(t)$, is connected to its Laplace transform, $\mathcal{LT}\left[f(t)\right](z)$, for small z,

$$\lim_{t\to\infty} f(t) = \lim_{z\to 0+} z\mathcal{LT}\left[f(t)\right](z). \tag{B.7}$$

The asymptotic solutions for the shear rate for a given approximation of the shear modulus is obtained in this way.

In the linear response regime, the constitutive equations give the stress as a convolution of the shear rate and a generalized modulus

$$\sigma(t) = \int_0^t \mathrm{d}t'\ \gamma(t')G(t-t'), \tag{B.8}$$

$$\Rightarrow \dot{\gamma}(t) = \mathcal{LT}^{-1}\left[\frac{\mathcal{LT}\left[\sigma(t)\right](z)}{\mathcal{LT}\left[G(t)\right](z)}\right](t). \tag{B.9}$$

If a back transformation of $\frac{\mathcal{LT}[\sigma(t)](z)}{\mathcal{LT}[G(t)](z)}$ is unknown, I obtain the asymptotic solution of the shear rate by finding an expansion for $\frac{\mathcal{LT}[\sigma(t)](z)}{\mathcal{LT}[G(t)](z)}$ around $z = 0$ and taking the inverse Laplace transform of this approximation.

C. Parameters of the schematic MCT model

C.1. Control parameters

- ε is the separation parameter, which denotes the relative separation from the glass transition point. Close, to the glass transition, it can be given as a relative packing fraction in relation to the critical packing fraction $\varepsilon \propto \frac{\varphi - \varphi_c}{\varphi}$. In the fluid regime, the time scale of the α–process scales with ε, $\tau_\alpha \propto |\varepsilon|^{-\gamma}$.
- $\dot{\gamma}$ denotes the shear rate, $\dot{\gamma} = \frac{\partial^2 x}{\partial t \partial y}$.
- σ denotes the shear stress.

C.2. Material parameters

- λ denotes the exponent parameter. It generates the critical exponents of the β–scaling.
- G_0 denotes the short–time shear modulus. It is the ratio between the immediate stress response to a step strain and the step strain's height $G_0 = \frac{\sigma}{\gamma}$ and vice versa. It also describes the ratio between the plateau modulus and the nonergodicity parameter squared at the glass transition $G_0 = \frac{G_\infty}{f_c^2}$.
- γ^* denotes the strain scale of the shear–induced decay of the stress kernel from the plateau. In steady shear it marks the shear strain, at which the generalized shear modulus equals 0 and the stress response displays a peak. In creep curves this strain scale marks the onset of tertiary flow or yielding. Close to the glass transition, $\varepsilon = 0, \dot{\gamma} = 0$, it is constant. For larger shear rates it starts to increase.
- γ^{**} denotes the strain scale of the shear–induced decay of the stress kernel to zero. Comparison between the schematic model, Brownian simulation and the results of the microscopic ITT approach for steady shear have shown, that this parameter depends linear on γ^*.
- γ_c denotes the strain scale of the shear–induced decay of the memory kernel.

C. Parameters of the schematic MCT model

- Γ denotes the time scale of the short–time decay of the density correlator and the shear modulus.
- η_∞^ω denotes the high–frequency viscosity. It can be seen as the asymptotic slope of the loss modulus for high frequencies. It can also be determined from the asymptotic slope of the flow curve $\eta_\infty^\omega + \frac{G_0}{2\Gamma}$ for large shear rates.
- a denotes the inertia parameter, introduced in comparison to rheological measurements with a rheometer. It can be determined from the initial creep $\frac{\sigma}{2a}t^2$ for a stress step σ, and from the frequency $\omega = \sqrt{\frac{G_\infty}{a} - \left(\frac{\eta_\infty^\omega}{2a}\right)^2}$ of inertio–elastic oscillations.

Bibliography

[1] Die Gesellschaft für deutsche Sprache (GfdS) *»Stresstest« zum Wort des Jahres 2011 gewählt* Press Release, 16 December 2011.

[2] Brown, R. (1828) *Ann. Phys.* **90(10)**, 294.

[3] Zwanzig, R. (1961) *Phys. Rev.* **124(4)**, 983.

[4] Mori, H. (1965) *Prog. Theor. Phys.* **33(3)**, 423–455.

[5] Einstein, A. (1906) *Ann. der Phys.* **324(2)**, 371–381.

[6] von Smoluchowski, M. (1906) *Ann. Phys.* **326(14)**, 756–780.

[7] Langevin, P. (1908) *C. R. Acad. Sci. Paris* **146**, 530–532.

[8] Fokker, A. D. (1914) *Ann. Phys.* **348(5)**, 810–820.

[9] Planck, M. (1917) *Sitzungsber. Preuss. Akad. Wiss.* **24**, 324–341.

[10] Fuchs, M. and Cates, M. E. (2009) *J. Rheol.* **53(4)**, 957–1000.

[11] Zwanzig, R. (2001) *Nonequilibrium statistical mechanics*, Oxford University Press, Oxford.

[12] Bengtzelius, U., Götze, W., and Sjölander, A. (1984) *J . Phys. C: Solid State Phys.* **17(33)**, 5915–5934.

[13] Fuchs, M. and Cates, M. E. (2002) *Phys. Rev. Lett.* **89(24)**, 248304.

[14] Brader, J. M., Cates, M. E., and Fuchs, M. (2012) *Phys. Rev. E* **86(2)**, 021403.

[15] Cichocki, B. and Hess, W. (1987) *Physica A* **141(2-3)**, 475–488.

[16] Fuchs, M. and Cates, M. E. (2005) *J. Phys. Condens. Matter* **17(20)**, S1681.

[17] Ornstein, L. S. and Zernike, F. (1914) *K. Ned. Akad. Wet., Proc.* **17(2)**, 793–806.

[18] Götze, W. (1991) *Liquids, Freezing and Glass Transition*, North-Holland, Amsterdam.

[19] Percus, J. and Yevick, G. (1958) *Phys. Rev.* **110(1)**, 1–13.

[20] Wertheim, M. (1963) *Phys. Rev. Lett.* **10(8)**, 321.

[21] Voigtmann, Th. and Fuchs, M. (2013) *Eur. Phys. J.-Spec. Top.* **222(11)**, 2819–2833.

[22] Arnold, V. I. (1986) *Catastrophe theory*, Springer, Berlin 2. edition.

[23] Gilmore, R. (1981) *Catastrophe theory for scientists and engineers*, Wiley, New York.

[24] Götze, W. (1985) *Z. Phys. B Condens. Matter* **60(2-4)**, 195–203.

[25] Franosch, T., Fuchs, M., Mayr, M. R., Singh, A. P., and Götze, W. (1997) *Phys. Rev. E* **55(6)**, 7153.

[26] Amann, C. P. *Time dependent flows in arrested states* PhD thesis, Universität Konstanz (2013).

[27] Götze, W. (1984) *Z. Phys. B Condens. Matter* **56(2)**, 139–154.

[28] Brader, J. M., Voigtmann, Th., Fuchs, M., Larson, R. G., and Cates, M. E. (2009) *Proc. Natl. Acad. Sci. U.S.A.* **106(36)**, 15186–15191.

[29] Fuchs, M. and Cates, M. E. (2003) *Farad. Discuss.* **123**, 267–286.

[30] Crassous, J. J., Siebenbürger, M., Ballauff, M., Drechsler, M., Hajnal, D., Henrich, O., and Fuchs, M. (2008) *J. Chem. Phys.* **128**, 204902.

[31] Hajnal, D. and Fuchs, M. (2009) *Eur. Phys. J. E Soft Matter* **28(2)**, 125–138.

[32] Amann, C. P., Siebenbürger, M., Krüger, M., Weysser, F., Ballauff, M., and Fuchs, M. (2013) *J. Rheol. (N. Y. N. Y).* **57(1)**, 149.

[33] Frahsa, F., Bhattacharjee, A. K., Horbach, J., Fuchs, M., and Voigtmann, Th. (2013) *J. Chem. Phys.* **138(12)**, 12A513.

[34] von Schweidler, E. (1907) *Ann. Phys.* **329(14)**, 711–770.

[35] Fuchs, M., Götze, W., Hildebrand, S., and Latz, A. (1992) *J. Phys.: Condens. Matter* **4(38)**, 7709.

[36] Kohlrausch, R. (1854) *Ann. Phys.* **167(1)**, 56–82.

[37] Siebenbürger, M., Fuchs, M., Winter, H., and Ballauff, M. (2009) *J. Rheol. (N. Y. N. Y).* **53(3)**, 707.

[38] Brader, J. M. (2010) *J. Phys.: Condens. Matter* **22(36)**, 363101.

[39] Farage, T. F. F. and Brader, J. M. (2012) *J. Rheol.* **56(2)**, 259.

[40] Voigtmann, Th., Brader, J. M., Fuchs, M., and Cates, M. E. (2012) *Soft Matter* **8(15)**, 4244–4253.

[41] Zausch, J., Horbach, J., Laurati, M., Egelhaaf, S. U., Brader, J. M., Voigtmann, Th., and Fuchs, M. (2008) *J. Phys. Condens. Matter* **20(40)**, 404210.

[42] Fritschi, S., Fuchs, M., and Voigtmann, T. (2014) *Soft matter* **10(27)**, 4822–4832.

[43] Bauschinger, J. (1886) *Mitt. aus d. Mechan.-Techn. Lab. d. Kgl. techn. Hochschule in München* **13**, 1–111.

[44] Falk, M. and Langer, J. (1998) *Phys. Rev. E* **57(6)**, 7192–7205.

[45] Karmakar, S., Lerner, E., and Procaccia, I. (2010) *Phys. Rev. E* **82(2)**, 026104.

[46] Hooke, R. (1678) *Lectures de potentia restitutiva, or of spring explaining the power of springing bodies.*, John Martyn, London.

[47] Quinson, R., Perez, J., Rink, M., and Pavan, A. (1996) *Journal of Materials Science* **31(16)**, 4387–4394.

[48] Quinson, R., Perez, J., Rink, M., and Pavan, A. (1997) *Journal of Materials Science* **32(5)**, 1371–1379.

[49] Brader, J., Cates, M., and Fuchs, M. (2008) *Phys. Rev. Lett.* **101(13)**, 138301.

[50] Siebenbürger, M., Ballauff, M., and Voigtmann, Th. (2012) *Phys. Rev. Lett.* **108(25)**, 255701.

[51] Fielding, S. M., Sollich, P., and Cates, M. E. (2000) *J. Rheol.* **44(2)**, 323.

[52] da C. Andrade, E. N. (1910) *Proc. R. Soc. A Math. Phys. Eng. Sci.* **84(567)**, 1–12.

[53] Miguel, M.-C., Vespignani, A., Zaiser, M., and Zapperi, S. (2002) *Phys. Rev. Lett.* **89(16)**, 165501.

[54] Ballauff, M., Brader, J. M., Egelhaaf, S. U., Fuchs, M., Horbach, J., Koumakis, N., Krüger, M., Laurati, M., Mutch, K. J., Petekidis, G., Siebenbürger, M., Voigtmann, Th., and Zausch, J. (2013) *Phys. Rev. Lett.* **110(21)**, 215701.

[55] Phillips, P. (1903) *Proc. Phys. Soc. Lond.* **19(1)**, 491–511.

[56] Nechad, H., Helmstetter, A., El Guerjouma, R., and Sornette, D. (2005) *Phys. Rev. Lett.* **94(4)**, 045501.

[57] Fielding, S. M. (2014) *Rep. Prog. Phys.* **77(10)**, 102601.

[58] Fuchs, M., Götze, W., Hofacker, I., and Latz, A. (1991) *J. Phys.: Condens. Matter* **3(26)**, 5047–5071.

[59] Sprakel, J., Lindstroem, S., Kodger, T., and Weitz, D. (2011) *Phys. Rev. Lett.* **106(24)**, 248303.

[60] Baldewa, B. and Joshi, Y. M. (2012) *Soft Matter* **8(3)**, 789–796.

[61] Da Cruz, F., Chevoir, F., Bonn, D., and Coussot, P. (2002) *Phys. Rev. E* **66(5)**, 051305.

[62] Bingham, E. (1916) *Bull. Bur. Stand.* **13**, 309–353.

[63] Barnes, H. A. and Walters, K. (1987) *Rheol. Acta* **24(4)**, 323–326.

[64] Baravian, C. and Quemada, D. (1998) *Rheol. Acta* **37(3)**, 223–233.

[65] Yao, N. Y., Larsen, R. J., and Weitz, D. a. (2008) *J. Rheol. (N. Y. N. Y).* **52(4)**, 1013.

[66] Chaudhuri, P. and Horbach, J. (2013) *Phys. Rev. E* **88(4)**, 040301.

[67] Divoux, T., Barentin, C., and Manneville, S. (2011) *Soft Matter* **7(18)**, 8409–8418.

[68] Grenard, V., Divoux, T., Taberlet, N., and Manneville, S. (2014) *Soft matter* **10(10)**, 1555–1571.

[69] Moorcroft, R., Cates, M., and Fielding, S. (2011) *Phys. Rev. Lett.* **106(5)**, 055502.

[70] Weyßer, F. *Rheology of Brownian Discs* PhD thesis, Universität Konstanz (2011).

[71] Henrich, O., Varnik, F., and Fuchs, M. (2005) *J. Phys.: Condens. Matter* **17(45)**, S3625–S3630.

[72] Laurati, M., Mutch, K. J., Koumakis, N., Zausch, J., Amann, C. P., Schofield, A. B., Petekidis, G., Brady, J. F., Horbach, J., Fuchs, M., and Egelhaaf, S. U. (2012) *J. Phys.: Condens. Matter* **24(46)**, 464104.

[73] Brent, R. P. (1973) *Algorithms for Minimization Without Derivatives*, Prentice-Hall, Englewood Cliffs, NJ.